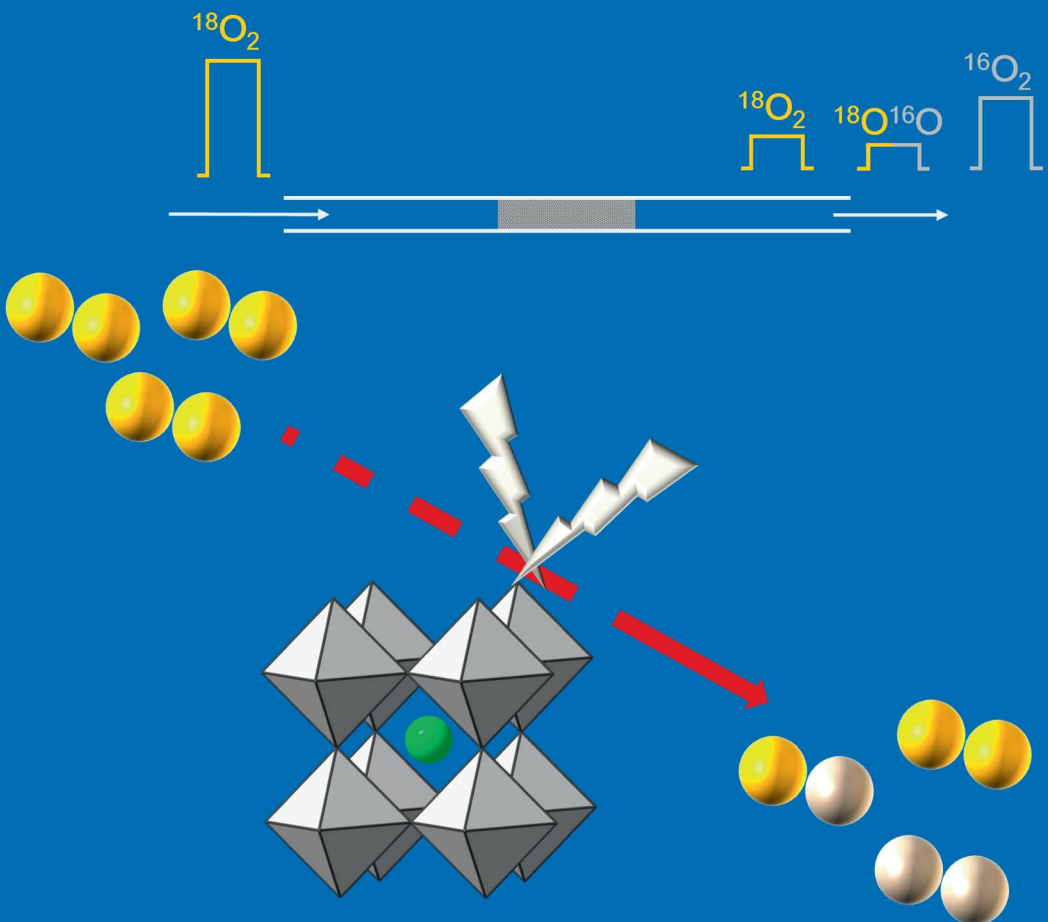


# Phase stability and oxygen transport properties of mixed ionic-electronic conducting oxides

Chung-Yul Yoo



**Phase stability and oxygen transport properties of  
mixed ionic-electronic conducting oxides**

Graduation committee:

Chairman:

prof. dr. G. van der Steenhoven (University of Twente)

Promotor:

prof. dr. ir. A. Nijmeijer (University of Twente)

Assistant promotor:

dr. H.J.M. Bouwmeester (University of Twente)

Committee members:

dr. B.A. Boukamp (University of Twente)

prof. dr. ir. H.J.W. Zandvliet (University of Twente)

prof. dr. ir. J.E. ten Elshof (University of Twente)

prof. dr. H.-D. Wiemhöfer (University of Münster)

prof. dr. P.V. Hendriksen (Technical University of Denmark)

The research described in this thesis was carried out in the Inorganic Membranes group and the MESA<sup>+</sup> Institute for Nanotechnology at the University of Twente, Enschede, the Netherlands. This project was financially supported by the Helmholtz Association of German Research Centres through the MEM-BRAIN Helmholtz Alliance.



Phase stability and oxygen transport properties of mixed ionic-electronic conducting oxides

Chung-Yul Yoo, Ph D thesis, University of Twente, The Netherlands

ISBN: 978-90-365-3394-2

DOI: 10.3990/1.9789036533942

Copyright © 2012 by Chung-Yul Yoo

Printed by Gildeprint, Enschede, The Netherlands

**PHASE STABILITY AND OXYGEN  
TRANSPORT PROPERTIES OF MIXED IONIC-  
ELECTRONIC CONDUCTING OXIDES**

**DISSERTATION**

to obtain  
the degree of doctor at the University of Twente,  
on the authority of the rector magnificus,  
prof. dr. H. Brinksma,  
on account of the decision of the graduation committee,  
to be publicly defended  
on Wednesday, 12th of September, 2012 at 16:45

by

**Chung-Yul Yoo**

born on 10th of February, 1982  
in Incheon, Republic of Korea

This dissertation has been approved by,

Promotor: prof. dr. ir. A. Nijmeijer

Assistant promotor: dr. H.J.M. Bouwmeester

# Table of Contents

<b>Chapter 1</b>	Introduction	1
1.1	Introduction	2
1.2	Structure and oxygen transport	2
1.2.1	Perovskite-type oxides	2
1.2.2	Fluorite-type oxides	5
1.3	Oxygen transport	6
1.3.1	Wagner equation	7
1.3.2	Oxygen flux limitations by surface exchange	8
1.4	Common experimental methods for evaluation of oxygen transport parameters	10
1.4.1	Isotope exchange depth profiling method	10
1.4.2	Gas phase analysis during isotope exchange	11
1.4.3	Electrical conductivity relaxation	12
1.5	Mechanism of oxygen surface exchange	13
1.6	Scope of the thesis	15
	References	17
<b>Chapter 2</b>	Phase transformation and oxygen equilibration kinetics of pure and Zr-doped $\text{Ba}_{0.5}\text{Sr}_{0.5}\text{Co}_{0.8}\text{Fe}_{0.2}\text{O}_{3-\delta}$ perovskite oxide probed by electrical conductivity relaxation	21
2.1	Introduction	22
2.2	Experimental	23
2.3	Results and discussion	24
2.4	Conclusions	30
	References	31
	Note Added in Proof	32
<b>Chapter 3</b>	Performance and stability of niobium-substituted $\text{Ba}_{0.5}\text{Sr}_{0.5}\text{Co}_{0.8}\text{Fe}_{0.2}\text{O}_{3-\delta}$ membranes	37
3.1	Introduction	38
3.2	Experimental	39
3.3	Results and discussion	42

3.3.1 Structure and phase analysis	42
3.3.2 Phase stability	44
3.3.3 Thermal expansion	46
3.3.4 Electrical conductivity	48
3.3.5 Oxygen permeation	51
3.4 Conclusions	54
References	56
<b>Chapter 4</b> <i>In-situ</i> neutron diffraction study of zirconium- and niobium-substituted $\text{Ba}_{0.5}\text{Sr}_{0.5}\text{Co}_{0.8}\text{Fe}_{0.2}\text{O}_{3-\delta}$	59
4.1 Introduction	60
4.2 Experimental	60
4.3 Results and discussion	61
4.4 Conclusions	71
Acknowledgement	71
References	72
<b>Chapter 5</b> Oxygen surface exchange kinetics of erbia-stabilized bismuth oxide	73
5.1 Introduction	74
5.2 Experimental	76
5.3 Results and discussion	78
5.4 Conclusions	88
References	89
<b>Chapter 6</b> Oxygen surface exchange kinetics of $\text{SrTi}_{1-x}\text{Fe}_x\text{O}_{3-\delta}$ mixed conducting oxides	91
6.1 Introduction	92
6.2 Experimental	93
6.2.1 Sample preparation and analysis	93
6.2.2 Pulse-response $^{18}\text{O}$ - $^{16}\text{O}$ isotope exchange measurements	94
6.3 Results and discussion	95
6.3.1 Sample characterization	95
6.3.2 Pulse isotopic exchange (PIE) measurements	96
6.3.3 Correlation between oxygen surface exchange rate and	

partial conductivities	100
6.3.4 Two-step exchange mechanism	104
6.4 Conclusions	111
Acknowledgement	112
References	113
Appendix	115
6.A Theory of oxygen isotopic exchange	115
6.B Data for alternative two-step exchange mechanism	122
<b>Chapter 7</b> Oxygen surface exchange kinetics of 20 mol% rare-earth oxide-doped ceria	125
7.1 Introduction	126
7.2 Experimental	126
7.2.1 Sample preparation and analysis	126
7.2.2 Pulse-response $^{18}\text{O}$ - $^{16}\text{O}$ isotope exchange measurements	127
7.3 Results and discussion	129
7.4 Conclusions	137
Acknowledgement	137
References	138
<b>Chapter 8</b> Oxygen surface exchange kinetics of $\text{La}_{1-x}\text{Sr}_x\text{CoO}_{3-\delta}$ ( $x = 0-0.7$ )	141
8.1 Introduction	142
8.2 Experimental	142
8.2.1 Sample preparation and analysis	142
8.2.2 Pulse-response $^{18}\text{O}$ - $^{16}\text{O}$ isotope exchange measurements	143
8.3 Results and discussion	145
8.4 Conclusions	152
References	153
<b>Chapter 9</b> Some recommendations for future research	155
9.1 Introduction	156
9.2 Stability of alkaline-earth doped perovskite oxides in $\text{CO}_2$ -containing atmospheres	156
9.3 Oxygen surface exchange kinetics	159



References	162
<b>Summary</b>	163
<b>Samenvatting</b>	167
<b>Acknowledgement</b>	171
<b>Curriculum vitae</b>	173

---

# Chapter 1

## Introduction

## 1.1 Introduction

Mixed ionic-electronic conductors (MIECs) have a potential for use as an oxygen separation membrane [1-3]. Application offers significant advantages over conventional cryogenic distillation, in the sense that membrane separation is simpler, more energy efficient, and provides a continuous delivery of oxygen with infinite selectivity [4]. MIEC membranes can also be integrated into a catalytic membrane reactor for the partial oxidation of hydrocarbons to value-added products, offering high selectivity and improved safety of operation by avoiding a direct mixing of the fuel with molecular oxygen [5-7]. Other potential applications of MIEC's include their use as electrodes in solid oxide fuel/electrolyzer cells (SOFCs/SOEC's), and as resistive oxygen sensors [8, 9].

This chapter provides a concise introduction into MIEC membranes for oxygen separation. Comprehensive reviews on fundamental aspects and developments in this field have been published by Bouwmeester and Burggraaf [2] and Sunarso *et al.* [3].

## 1.2 Structure and oxygen transport

### 1.2.1 Perovskite-type oxides

Perovskite-type oxides exhibit a wide range of physical properties, such as ferroelectricity, piezoelectricity, magnetic property, superconductivity, and electronic/ionic conductivity [10, 11]. They are named after the mineral perovskite  $\text{CaTiO}_3$ , which was first discovered in the Ural mountains by Gustav Rose in 1839, who named it after the Russian mineralogist Lev Alekseevich Perovski.

The general structural formula of a perovskite oxide is  $\text{ABO}_3$ . In the  $\text{ABO}_3$  structure, the A-site is occupied by an alkali, alkaline earth, or rare earth cation, while the B-site is occupied by a transition metal or rare earth cation.

The ideal cubic perovskite oxide, shown in Fig. 1.1, is composed of a three-dimensional framework of corner-shared  $\text{BO}_6$  octahedra.

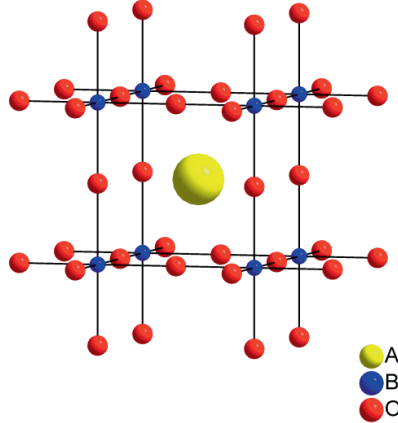


**Figure 1.1** Ideal cubic  $\text{ABO}_3$  perovskite structure.

The octahedra create cavities that are occupied by A-site cations. A- and B-site cations are in 12- and 6-fold coordination by oxygen, respectively, while each of the oxygen ions is bound to 6 neighboring cations (4A and 2B cations). Although the ideal symmetry is cubic, many perovskites exhibit distorted structures due to tilting of the  $\text{BO}_6$  octahedra. Goldschmidt [12] proposed a tolerance factor,  $t$ , which defines the degree of distortion in the perovskite structure,

$$t = \frac{(r_A + r_O)}{\sqrt{2}(r_B + r_O)} \quad (1.1)$$

where  $r_A$ ,  $r_B$ , and  $r_O$  are the radii of the A-site and B-site cations, and the oxygen ion, respectively. The parameter  $t$  has been widely used for assessment of the formation and stability of the cubic perovskite structure. The ideal cubic perovskite structure exhibits a  $t$ -value close to unity. The cubic structure is found to occur for  $0.8 < t < 1$  [13]. Lower values of  $t$  will lead to a structure with a lower symmetry. The parameter  $t$  is not always a reliable tool to assess

formation of the cubic perovskite structure. Other factors, such as the specific free volume (void fraction) and extent of oxygen nonstoichiometry, might need to be taken into account as well [14-16].

The first pioneering study on perovskite membranes for oxygen separation was conducted on  $\text{La}_{1-x}\text{Sr}_x\text{Co}_{1-y}\text{Fe}_y\text{O}_{3-\delta}$  ( $x = 0-1$ ,  $y = 0-1$ ) by Teraoka *et al.* [17]. The partial substitution of A-site cations,  $\text{La}^{3+}$ , by lower valent  $\text{Sr}^{2+}$  cations is charge compensated by the formation of oxygen vacancies and/or valence changes of the B-site cations. Teraoka *et al.* observed the rate of oxygen permeation to increase with increasing molar fractions of both strontium and cobalt. The highest oxygen flux in the series was found for  $\text{SrCo}_{0.8}\text{Fe}_{0.2}\text{O}_{3-\delta}$ . Substitution of 20 mol% of cobalt by iron suppresses the undesirable phase transition from cubic perovskite to a non-perovskite phase with hexagonal structure, as found for  $\text{SrCoO}_{3-\delta}$  in air, below  $\sim 950$  °C [18].

Although cubic  $\text{SrCo}_{0.8}\text{Fe}_{0.2}\text{O}_{3-\delta}$  shows a high, favorable oxygen permeation rate, a phase transition to a vacancy-ordered brownmillerite phase occurs, at  $\sim 790$  °C, below an oxygen partial pressure of 0.01 atm [19-21].  $\text{Ba}_{0.5}\text{Sr}_{0.5}\text{Co}_{0.8}\text{Fe}_{0.2}\text{O}_{3-\delta}$  (BSCF) is obtained by partial substitution of strontium by barium in  $\text{SrCo}_{0.8}\text{Fe}_{0.2}\text{O}_{3-\delta}$ . The  $\text{Ba}^{2+}$  (1.61 Å) has a much larger radius than  $\text{Sr}^{2+}$  (1.44 Å) [22]. Partial substitution of  $\text{Sr}^{2+}$  by  $\text{Ba}^{2+}$  suppresses ordering of oxygen vacancies, which decreases oxide ionic conductivity, but also enhances the oxygen vacancy concentration. The latter relates to a change in the mechanism of charge compensation associated with the expansion of the lattice upon partial substitution of  $\text{Sr}^{2+}$  by  $\text{Ba}^{2+}$  [23, 24]. Unfortunately, the oxygen permeation rate of BSCF is found to decline with the time on stream below  $\sim 825$  °C, due to a sluggish phase decomposition of the parent phase into a mixture of cubic and hexagonal polymorphs [25-26]. Recently, it was found that such decomposition can be suppressed by a small co-doping of either Zr or Nb on the B-site [30, 31].

Although high oxygen fluxes may be found for the perovskite-type membranes, their chemical stability, *e.g.*, under large oxygen potential gradients and towards gas phase impurities, such as  $\text{CO}_2$ ,  $\text{SO}_2$ , and  $\text{H}_2\text{O}$ , needs to be improved before any industrial application becomes feasible [32, 33].

### 1.2.2 Fluorite-type oxides

Although most research in the field of ceramic membranes for oxygen separation is conducted towards perovskite-structured oxide materials, another type of structure favorable to oxide ion transport is the fluorite structure. The general formula of a fluorite-type oxide is  $\text{MO}_2$ . The ideal structure is shown in Fig. 1.2, and can be regarded as a face-centered cubic packing of cations with the anions in all of the tetrahedral interstitial sites. The coordination number for each cation is 8, while that of the anions is 4. Fluorite oxides may exhibit high concentrations of oxygen vacancies, which are either intrinsic, such as in  $\delta\text{-Bi}_2\text{O}_3$ , or formed by doping with lower valent oxides, like  $\text{Y}_2\text{O}_3$  in  $\text{ZrO}_2$ , or  $\text{Gd}_2\text{O}_3$  in  $\text{CeO}_2$  [8].

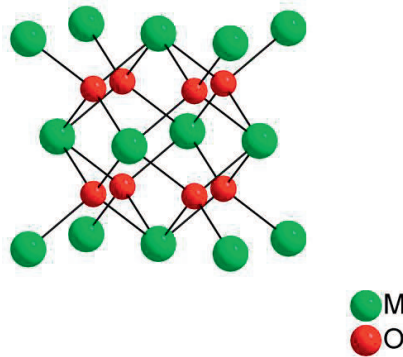


**Figure 1.2** Ideal cubic  $\text{MO}_2$  fluorite structure.

Among the fluorite oxides,  $\delta\text{-Bi}_2\text{O}_3$ , whose structure is stabilized by a rare earth dopant, *e.g.*, yttria or erbia, shows the highest oxygen permeation rate

[34-36]. The dopant prevents the phase transition from the cubic  $\delta$ -phase to the monoclinic  $\alpha$ -phase below  $\sim 730$  °C [37]. The poor chemical stability of the bismuth oxide-based materials at low oxygen partial pressure severely limits their potential use as an oxygen separation membrane. Gadolinia-, terbia-, and praseodymia-doped ceria have been reported for use as an oxygen transport membrane [38-41], showing comparable oxygen permeation fluxes to  $\delta$ - $\text{Bi}_2\text{O}_3$ -based membranes.

### 1.3 Oxygen transport

When a gradient in oxygen chemical potential is imposed across a dense MIEC membrane, oxygen ions are transported from high to low oxygen chemical potential. Charge neutrality is retained by a simultaneous counter transport of electrons as shown schematically in Fig. 1.3. Overall oxygen transport through the membrane is governed by (i) the surface exchange reaction at the feed side interface, (ii) electron (or electron hole) and oxygen ion diffusion in the bulk, and, (iii) the surface exchange reaction at the permeate side interface.

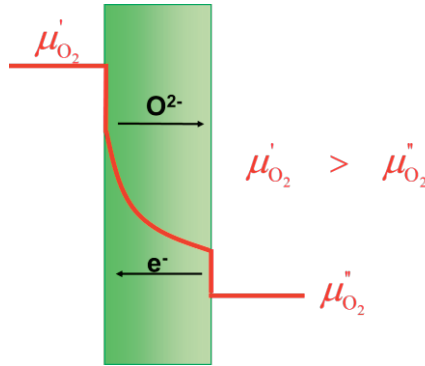
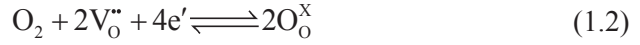


**Figure 1.3** Schematic illustration of the variation in oxygen chemical potential across interface and bulk regions of a MIEC membrane.

### 1.3.1 Wagner equation

The reaction between gas phase oxygen and lattice oxygen can be written as, using Kröger-Vink notation



assuming that oxygen vacancies are fully ionized. The intrinsic ionization across the band gap, producing electrons and electron holes, can be expressed as



The transport of each charge carrier under the influence of a spatial gradient in electrochemical potential is described by the Onsager equation. Neglecting cross terms between the fluxes, the Onsager equation reads

$$j_i = -\frac{\sigma_i}{z_i^2 F^2} \nabla \eta_i \quad (1.4)$$

where  $\nabla \eta_i$  is the gradient of the electrochemical potential of charge carrier  $i$ ,  $z_i$  its charge number,  $F$  the Faraday constant, and  $\sigma_i$  the conductivity of the charge carrier. The electrochemical potential gradient,  $\nabla \eta_i$  comprises a gradient in chemical potential,  $\nabla \mu_i$ , and a gradient in electrical potential,  $\nabla \phi_i$ ,

$$\nabla \eta_i = \nabla \mu_i + z_i F \nabla \phi_i \quad (1.5)$$

The fluxes of ionic and electronic defects are coupled to each other by charge balance,

$$2j_{\text{O}^{2-}} = j_{\text{h}' } + j_{\text{e}' } \quad (1.6)$$

In view of Eqs. (1.2) and (1.3), the following differential relations hold at thermodynamic equilibrium,



$$\nabla\mu_{\text{O}_2} + 2\nabla\mu_{\text{V}_\text{O}^\bullet} + 4\nabla\mu_{\text{e}^\bullet} = 0 \quad (1.7)$$

$$\nabla\mu_{\text{h}^\bullet} + \nabla\mu_{\text{e}^\bullet} = 0 \quad (1.8)$$

where  $\mu_{\text{V}_\text{O}^\bullet}$  is the chemical potential of an oxygen vacancy,  $\mu_{\text{e}^\bullet}$  and  $\mu_{\text{h}^\bullet}$  the chemical potential of electron and electron hole, respectively. The oxygen flux through the membrane can be derived by combining Eqs. (1.4)-(1.8), using

$j_{\text{O}_2} = -\frac{1}{2}j_{\text{V}_\text{O}^\bullet}$ . One finds,

$$j_{\text{O}_2} = -\frac{1}{4^2 F^2} \frac{\sigma_{\text{ele}}\sigma_{\text{ion}}}{\sigma_{\text{ele}} + \sigma_{\text{ion}}} \nabla\mu_{\text{O}_2} \quad (1.9)$$

where  $\sigma_{\text{ion}} = \sigma_{\text{V}_\text{O}^\bullet}$  and  $\sigma_{\text{ele}} = \sigma_{\text{h}^\bullet} + \sigma_{\text{e}^\bullet}$ . Eq. (1.9) was first derived by Carl Wagner and used in modeling of the scaling of oxides. Integrating Eq. (1.9) over membrane thickness,  $L$ , using the relationship  $\nabla\mu_{\text{O}_2} = RT\nabla\ln p\text{O}_2$ , yields the Wagner equation in its usual integral form,

$$j_{\text{O}_2} = -\frac{RT}{4^2 F^2 L} \int_{\ln p\text{O}_2^\bullet}^{\ln p\text{O}_2^\dagger} \frac{\sigma_{\text{ele}}\sigma_{\text{ion}}}{\sigma_{\text{ele}} + \sigma_{\text{ion}}} d\ln p\text{O}_2 \quad (1.10)$$

where  $p\text{O}_2^\dagger$  and  $p\text{O}_2^\bullet$  are the oxygen partial pressures at the feed and permeate sides of the membrane, respectively. Other parameters in Eq. (1.10) have their usual significance or have been specified above.

### 1.3.2 Oxygen flux limitations by surface exchange

Eq. (1.10) has been derived assuming that the kinetics of oxygen transport across the MIEC membrane is governed by ambipolar diffusion of ionic and electronic charge carriers. It predicts that the oxygen flux would increase by reducing the thickness of the membrane. In practice, the oxygen flux increases

until it is entirely governed by the rate of oxygen surface exchange at the gas/solid interfaces, and no gain in oxygen flux can be obtained by further reducing membrane thickness. Bouwmeester *et al.* [42] defined a characteristic thickness,  $L_c$ , at which point the flux is under equal control of oxygen diffusion and surface exchange. Under the assumption of linear kinetics of the relevant rate laws, the oxygen flux under conditions of mixed control of oxygen diffusion and surface exchange is given by [42]

$$j_{\text{O}_2} = -\frac{1}{1 + 2L_c / L} \frac{1}{4^2 F^2} \frac{\sigma_{\text{ele}} \sigma_{\text{ion}}}{\sigma_{\text{ele}} + \sigma_{\text{ion}}} \frac{\Delta\mu_{\text{O}_2}^{\text{total}}}{L} \quad (1.11)$$

where  $\Delta\mu_{\text{O}_2}^{\text{total}}$  is the total oxygen chemical potential difference across the membrane. With the aid of the classical Nernst-Einstein equation, assuming the MIEC to exhibit predominant electronic conduction, the characteristic membrane thickness,  $L_c$ , can accordingly be represented as [42],

$$L_c = \frac{D^*}{k^*} \quad (1.12)$$

where  $D^*$  ( $\text{m}^2 \text{s}^{-1}$ ) and  $k^*$  ( $\text{m s}^{-1}$ ) are the tracer diffusion and surface exchange coefficients, respectively. The factor 2 in the denominator of Eq. (1.11) is suggesting that surface exchange rate limitations occur at both membrane surfaces. The assumption of linear kinetics in its derivation implies that Eq. (1.11) is valid in the limit of small values for  $\Delta\mu_{\text{O}_2}^{\text{total}}$ , hence, for small  $p\text{O}_2$  gradients across the membrane only.

The characteristic membrane thickness,  $L_c$ , for mixed ionic-electronic conducting perovskite-type oxide varies, typically, in the range 10-100  $\mu\text{m}$ , while for fluorite-type oxides it may vary in the range of mm to cm [2]. Techniques to estimate both parameters in Eq. (1.12) relevant for calculation of  $L_c$

are discussed in the next sections, with emphasis on experimental evaluation and interpretation of data on oxygen surface exchange.

## 1.4 Common experimental methods for evaluation of oxygen transport parameters

### 1.4.1 Isotope exchange depth profiling method

A powerful method to measure both  $D^*$  and  $k^*$  is  $^{18}\text{O}$ - $^{16}\text{O}$  isotope exchange followed by *ex-situ* depth profiling (IEDP), usually by using secondary ion mass spectrometry (SIMS) [43]. In this method, a single crystal or well-polished dense ceramic is first subjected to an  $^{18}\text{O}$  anneal for a fixed period of time. Subsequently, the sample is quenched, and the  $^{18}\text{O}$  diffusion profile in the oxide probed by depth profiling. The departure of the isotope composition at the oxide surface ( $x = 0$ ) from that in the gas phase is accounted for by the boundary condition,

$$D^* c_o \left. \frac{\partial f_o^{18}}{\partial x} \right|_{x=0} = -k^* c_o (f_g^{18} - f_o^{18}) \quad (1.13)$$

where  $c_o$  is the oxygen ion concentration in the oxide,  $f_o^{18}$  and  $f_g^{18}$  are the  $^{18}\text{O}$  isotope fractions in the oxide and gas phase, respectively. Eq. (1.13) assumes simple first-order kinetics for the surface exchange reaction, and is commonly referred to as McKay's equation [44]. Fitting the measured  $^{18}\text{O}$  depth profile to the appropriate solution of Fick's diffusion equation yields both  $k^*$  and  $D^*$  [42]. Although IEDP has been applied extensively for the evaluation of kinetic parameters of acceptor-doped fluorite- and perovskite-type oxides [43, 45-47], a clear drawback is that the method involves a number of rapid heating and quenching steps. Not only is this very time consuming, but also one must exercise great care in order to avoid introducing artifacts and errors into the assessment of the kinetic parameters.

### 1.4.2 Gas phase analysis during isotope exchange

A number of techniques are based on gas-phase analysis of the  $^{18}\text{O}$  concentration during  $^{18}\text{O}$ - $^{16}\text{O}$  isotope exchange with the oxide enclosed either in a vessel or a continuous flow reactor, using *in-situ* mass spectrometry [48, 49]. As holds for the IEDP method, the isotope exchange measurements are conducted at isothermal and iso- $p\text{O}_2$  conditions. In the gas-phase based methods, the  $^{18}\text{O}$  uptake by the oxide is monitored by measuring the time-dependent decline of the  $^{18}\text{O}$  concentration in the gas phase during isotope exchange. In the pulse-isotope exchange (PIE) technique as employed in this Ph D work, an  $^{18}\text{O}$ -enriched gas phase pulse is passed through a continuous flow reactor loaded with the oxide [50]. The  $^{18}\text{O}$  uptake by the oxide during the residence time of the pulse in the reactor is assessed from the residual  $^{18}\text{O}$  concentration measured in the effluent pulse. The exchange rate  $\mathfrak{R}_0$  at the gas/oxide interface ( $x=0$ ) can be calculated from the appropriate integrated rate equations, derived from McKay's first-order differential equation for isotope exchange (*cf.* with Eq. (1.13)),

$$\frac{1}{S} \frac{n \partial f_g^{18}}{\partial t} = -\mathfrak{R}_0 (f_g^{18} - f_o^{18}) \Big|_{x=0} \quad (1.14)$$

where  $n$  is the number of oxygen atoms in the gas phase,  $S$  the oxide surface area available for exchange, and  $\mathfrak{R}_0$  ( $\text{mol O m}^{-2} \text{ s}^{-1}$ ) the balanced exchange rate at equilibrium. Note from comparison of Eqs. (1.13) and (1.14):  $\mathfrak{R}_0 = k^* c_o$ . A key point to note is that in the case of mixed surface exchange and bulk diffusion control the corresponding rate equations become rather complex. For example, see Ref. [51, 52]. An advantage of  $^{18}\text{O}$ - $^{16}\text{O}$  isotope exchange methods based upon gas-phase analysis over, for example, the IEDP method is that the measured distribution  $^{18}\text{O}_2$ ,  $^{18}\text{O}^{16}\text{O}$ , and  $^{16}\text{O}_2$  isotopomers in the gas phase provides additional information about the mechanism of the exchange reaction.

### 1.4.3 Electrical conductivity relaxation

In these experiments, the electrical conductivity of a dense ceramic oxide is *in-situ* monitored as a function of time after a small, instantaneous change of the surrounding oxygen partial pressure in the gas phase [48, 53-55]. Measurements are conducted, at chosen conditions of temperature and oxygen partial pressure, using usually a four-probe ac or dc technique to avoid polarization effects. The change in electrical conductivity relates to equilibration of the oxide towards a new oxygen stoichiometry. In view of the small change in oxygen partial pressure the conductivity-stoichiometry relationship is linearized. Fitting the time-dependent conductivity to the appropriate non-equilibrium solution of Fick's diffusion equation yields the chemical diffusion coefficient,  $D_{\text{chem}}$  ( $\text{m}^2 \text{s}^{-1}$ ) and associated surface exchange coefficient,  $k_{\text{chem}}$  ( $\text{m s}^{-1}$ ). The boundary condition often used in derivation is

$$D_{\text{chem}} \frac{\partial c(t)}{\partial x} = -k_{\text{chem}} (c(t) - c_{\infty}) \Big|_{x=0} \quad (1.15)$$

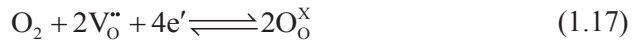
where  $c_{\infty}$  is the equilibrium oxygen concentration at time  $t = \infty$ . The non-equilibrium values  $D_{\text{chem}}$  and  $k_{\text{chem}}$  relate to their corresponding equilibrium values  $D^*$  and  $k^*$ . Neglecting correlation effects, these relationships can be represented as  $D_{\text{chem}} = D^* \gamma$  and  $k_{\text{chem}} = k^* \gamma$ , where  $\gamma$  is a thermodynamic factor [48, 54, 55]

$$\gamma = -\frac{1}{2} \frac{\partial \ln p\text{O}_2}{\partial \ln c_{\text{O}}} \quad (1.16)$$

relating oxygen concentration and oxygen partial pressure. Care must be taken in the experiments that the apparent characteristic time for gas switching is shorter than that of oxide (re-)equilibration. This implies that reactor residence times (= reactor volume/volumetric flow rate) must be sufficiently small [48, 56].

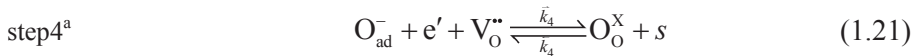
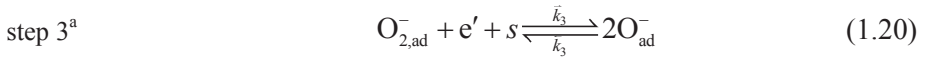
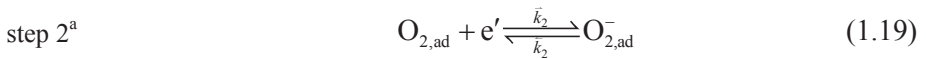
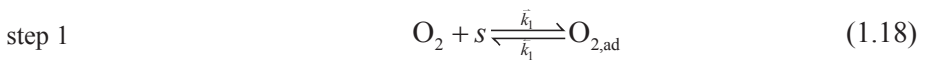
## 1.5 Mechanism of oxygen surface exchange

To date, mechanistic understanding of the oxygen exchange reaction is rather rudimentary. This is, at least in part, due to difficulties in probing oxygen surface exchange at elevated temperatures, where these reactions are most pertinent. It is generally conceived that oxygen exchange between the gas phase and the oxide comprises a series of steps. Possible steps include gas phase diffusion, adsorption, dissociation, surface diffusion of intermediates, charge transfer, and finally incorporation of the oxygen ions into the oxide lattice. Several intermediates may occur, such as  $O_{2,ad}$ ,  $O_{2,ad}^-$ , and  $O_{ad}^-$ . The overall exchange reaction can be written as



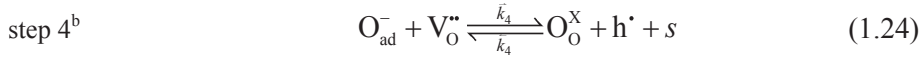
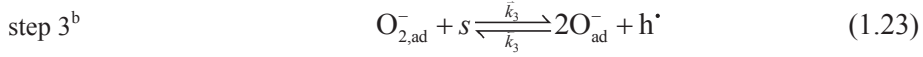
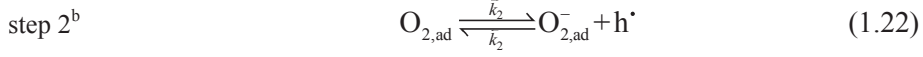
This reaction can be broken down in a number of reaction steps, each of which may be partially rate determining.

A possible, but certainly not exclusive, pathway for the oxygen reduction reaction (ORR), and subsequent incorporation of the oxygen ions into the oxide is



where  $s$  denotes an adsorption site. Electron transfer to adsorbed intermediates, as apparent in steps (1.19)-(1.21), occurs via the conduction band (CB) or the

valence band (VB). In the latter case, the kinetics of reactions is more appropriately described by writing reactions (1.19)-(1.21) as



The apparent  $p\text{O}_2$  dependence of the surface exchange rate,  $\mathfrak{R}_0$ , is commonly interpreted, assuming *i*) a low coverage of adsorbed or oxygen intermediate species, *ii*) a single rate determining step (rds), while all other steps have attained virtual equilibrium, *iii*) simple power law dependences of oxygen defects and electronic charge carriers on  $p\text{O}_2$ , while disregarding *iv*) the possible relevance of reaction symmetry parameters analogous to that used in description of electrochemical electrode kinetics. For the sake of illustration, calculated power law dependences of the exchange rate,  $\mathfrak{R}_0$ , on  $p\text{O}_2$ , assuming successive steps (1.18)-(1.24) to be rate-determining, are shown in Table 1.1. The experimentally observed rate of  $\mathfrak{R}_0$  on  $p\text{O}_2$  could thus be helpful in assignment of the rds. Often, however, a number of different, alternative mechanisms may be proposed to explain the observed  $p\text{O}_2$  dependence of  $\mathfrak{R}_0$ . In this Ph D study, correlations between  $\mathfrak{R}_0$  and other bulk properties, *e.g.*, partial ionic and electronic conductivities, and oxygen vacancy concentration, are used in an attempt to shed more light on possible factors determining the rate of the surface oxygen exchange on oxide ion conducting solids.

**Table 1.1** Exponents  $n$  in the power law dependence of the overall exchange rate,  $\mathfrak{R}_0 \propto (pO_2)^n$  calculated assuming each of reactions (1.18)-(1.24) to be the rate-determining step (rds). Corresponding power law dependences of the bulk defects are taken as:  $[h^\bullet]^{-1} = [e'] \sim (pO_2)^x$  and  $[V_o^{\bullet\bullet}] \sim (pO_2)^y$ , Charge neutrality requires  $1+4x+2y = 0$ . Cases *a* and *b* refer to electron transfer via the conduction band (CB) and valence band (VB), respectively.

rds	$n$	$n$
	Case <i>a</i> : electron transfer via CB	Case <i>b</i> : electron transfer via VB
step 1	1	1
step 2	$1+x$	1
step 3	$1+2x$	$1+x$
step 4	$0.5+2x+y$	$0.5+x+y$

## 1.6 Scope of the thesis

The key objectives of the research described in this thesis are examination of the crystal structure and phase stability of selected perovskite- and fluorite-structured oxides, and elucidation of the oxygen transport kinetics, with emphasis on the oxygen surface exchange properties, exhibited by these solids.

As mentioned above, the state-of-the-art mixed conducting perovskite-type oxide  $Ba_{0.5}Sr_{0.5}Co_{0.8}Fe_{0.2}O_{3-\delta}$  (BSCF) is known to decompose at moderate temperatures into a mixture of cubic and hexagonal polymorphs. In Chapters 2 and 3, the phase stability and oxygen transport properties of BSCF are investigated after partial substitutions of (Co,Fe) by Zr and Nb, respectively. In



Chapter 4, the corresponding crystal structures of both oxides are investigated using *in-situ* high-temperature neutron diffraction. In Chapters 5-8, oxygen surface exchange is studied on 25 mol% erbia-doped  $\text{Bi}_2\text{O}_3$  (Chapter 5),  $\text{SrTi}_{1-x}\text{Fe}_x\text{O}_{3-\delta}$  (Chapter 6), 20 mol% rare-earth oxide-doped  $\text{CeO}_2$  (Chapter 7), and  $\text{La}_{1-x}\text{Sr}_x\text{CoO}_{3-\delta}$  (Chapter 8) using  $^{18}\text{O}$ - $^{16}\text{O}$  pulse isotope exchange (PIE) technique. Finally, in Chapter 9, recommendations for future research are given.

---

## References

1. M. Czaperek, P. Zapp, H.J.M. Bouwmeester, M. Modigell, K. Ebert, I. Voigt, W. Meulenberg, L. Singheiser, D. Stöver, *J. Membrane. Sci.* 359 (2010) 149.
2. H.J.M. Bouwmeester, A.J. Burggraaf, "Chapter 14 Dense ceramic membranes for oxygen separation", in: *The CRC Handbook of Solid State Electrochemistry*, edited by P.J. Gellings and H.J.M. Bouwmeester, CRC press, Boca Raton (1997).
3. J. Sunarso, S. Baumann, J. Serra, W. Meulenberg, S. Liu, Y. Lin, J. Diniz da Costa, *J. Membrane. Sci.* 320 (2008) 13.
4. P.N. Dyer, R.E. Richards, S.L. Russek, D.M. Taylor, *Solid State Ionics* 134 (2000) 21.
5. J.E. ten Elshof, B.A. van Hassel, H.J.M. Bouwmeester, *Catal. Today* 25 (1995) 397.
6. W. Yang, H. Wang, X. Zhu, L. Lin, *Top. Catal.* 35 (2005) 155.
7. S. Liu, X. Tan, K. Li, R. Hughes, *Catalysis Reviews* 43 (2001) 147.
8. A.J. Jacobson, *Chem. Mater.* 22 (2009) 660.
9. R. Ramamoorthy, P. Dutta, S. Akbar, *J. Mater. Sci.* 38 (2003) 4271.
10. A. Bhalla, R. Guo, R. Roy, *Mater. Res. Innov.* 4 (2000) 3.
11. M. Pena, J. Fierro, *Chem. Rev.* 101 (2001) 1981.
12. V. Goldschmidt, *Skifter Norsk. Vidensk. Akad. Klass 1* (1926) 1.
13. C. Li, K. C. K. Soh, P. Wu, *J. Alloy. Compd.* 372 (2004) 40.
14. L. Feng, L. Jiang, M. Zhu, H. Liu, X. Zhou, C. Li, *J. Phys. Chem. Solids* 69 (2008) 967.
15. H. Hayashi, H. Inaba, M. Matsuyama, N. Lan, M. Dokiya, H. Tagawa, *Solid State Ionics* 122 (1999) 1.
16. J.C. Boivin, *Int. J. Inorg. Mater.* 3 (2001) 1261.
17. Y. Teraoka, H. Zhang, S. Furukawa, N. Yamazoe, *Chem. Lett.* 31 (1985) 1743.
18. Z. Deng, W. Yang, W. Liu, C. Chen, *J. Solid State Chem.* 179 (2006) 362.
19. L. Liu, T. Lee, L. Qiu, Y. Yang, A. Jacobson, *Mater. Res. Bull.* 31 (1996) 29.
20. S. McIntosh, J.F. Vente, W.G. Haije, D.H.A. Blank, H.J.M. Bouwmeester, *Solid State Ionics* 177 (2006) 833.
21. S. McIntosh, J.F. Vente, W.G. Haije, D.H.A. Blank, H.J.M. Bouwmeester, *Solid State Ionics* 177 (2006) 1737.
22. R.D. Shannon, *Acta Crystallogr. A* 32 (1976) 751.
23. S. McIntosh, J.F. Vente, W.G. Haije, D.H.A. Blank, H.J.M. Bouwmeester, *Chem. Mater.* 18 (2006) 2187.
24. Z. Shao, G. Xiong, H. Dong, W. Yang, L. Lin, *Sep. Purif. Technol.* 25 (2001) 97.

25. S. Švarcová, K. Wiik, J. Tolchard, H.J.M. Bouwmeester, T. Grande, *Solid State Ionics* 178 (2008) 1787.
26. M. Arnold, T.M. Gesing, J. Martynczuk, A. Feldhoff, *Chem. Mater.* 20 (2008) 5851.
27. D.N. Mueller, R.A. De Souza, T.E. Weirich, D. Roehrens, J. Mayer, M. Martin, *Phys. Chem. Chem. Phys.* 12 (2010) 10320.
28. K. Efimov, Q. Xu, A. Feldhoff, *Chem. Mater.* 22 (2010) 5866.
29. A.C. van Veen, M. Rebeilleau, D. Farrusseng, C. Mirodatos, *Chem. Commun.* (2003) 32.
30. S. Yakovlev, C.-Y. Yoo, S. Fang, H.J.M. Bouwmeester, *Appl. Phys. Lett.* 96 (2010) 254101.
31. S.M. Fang, C.-Y. Yoo, H.J.M. Bouwmeester, *Solid State Ionics* 195 (2011) 1.
32. M. Schulz, R. Kriegel, A. Kämpfer, *J. Membrane. Sci.* 378 (2011) 10.
33. S. Engels, T. Markus, M. Modigell, L. Singheiser, *J. Membrane. Sci.* 370 (2010) 58.
34. Y. Zeng, Y. Lin, *J. Catal.* 193 (2000) 58.
35. H.J.M. Bouwmeester, H. Kruidhof, A. Burggraaf, P. Gellings, *Solid State Ionics* 53 (1992) 460.
36. E. Capoen, M. Steil, G. Nowogrocki, M. Malys, C. Pirovano, A. Löfberg, E. Bordes-Richard, J.C. Boivin, G. Mairesse, R.N. Vannier, *Solid State Ionics* 177 (2006) 483.
37. T. Takahashi, T. Esaka, H. Iwahara, *J. Solid State Chem.* 16 (1976) 317.
38. C. Chatzichristodoulou, M. Sogaard, J. Glasscock, A. Kaiser, S. P.V. Foghmoes, P.V. Hendriksen, *J. Electrochem. Soc.* 158 (2011) F73.
39. A. Kaiser, S. Foghmoes, C. Chatzichristodoulou, M. Sogaard, J. Glasscock, H.L. Frandsen, P.V. Hendriksen, *J. Membrane. Sci.* 378 (2010) 51.
40. M. Balaguer, C. Solís, J. M. Serra, *Chem. Mater.* 23 (2011) 2333.
41. D. Fagg, A. Shaula, V. Kharton, J. Frade, *J. Membrane. Sci.* 299 (2007) 1.
42. H.J.M. Bouwmeester, H. Kruidhof, A. Burggraaf, *Solid State Ionics* 72 (1994) 185.
43. J.A. Kilner, S.J. Skinner, H.H. Brongersma, *J. Solid State Electrochem.* 15 (2011) 861.
44. H.A.C. McKay, *Nature* 142 (1938) 997.
45. R.A. De Souza, J.A. Kilner, *Solid State Ionics* 106 (1998) 175.
46. R.A. De Souza, J.A. Kilner, *Solid State Ionics* 126 (1999) 153.
47. R. Merkle, J. Maier, H.J.M. Bouwmeester, *Angew. Chem. Int. Edit.* 43 (2004) 5069.
48. M.W. den Otter, A study of oxygen transport in mixed conducting oxides using isotopic exchange and conductivity relaxation, Ph D thesis, University of Twente (2000).
49. B.A. Boukamp, I.C. Vinke, K.J. De Vries, A.J. Burggraaf, *Solid State Ionics* 32 (1989) 918.

50. H.J.M. Bouwmeester, C. Song, J. Zhu, J. Yi, M. van Sint Annaland, B.A. Boukamp, *Phys. Chem. Chem. Phys.* 11 (2009) 9640.
51. K. Klier, E. Kucera, *J. Phys. Chem. Solids* 27 (1966) 1087.
52. A.N. Ezin, V.I. Tsidilkovski, E.K. Kurumchin, *Solid State Ionics* 84 (1996) 105.
53. B.A. Boukamp, M.W. den Otter, H.J.M. Bouwmeester, *J. Solid State Electrochem.* 8 (2004) 592.
54. J. Lane, S. Benson, D. Waller, J. Kilner, *Solid State Ionics* 121 (1999) 201.
55. L.M. van der Haar, M.W. den Otter, M. Morskate, H.J.M. Bouwmeester, H. Verweij, *J. Electrochem. Soc.* 149 (2002) J41.
56. M.W. den Otter, H.J.M. Bouwmeester, B.A. Boukamp, H. Verweij, *J. Electrochem. Soc.* 148 (2001) J1.



---

## Chapter 2

# Phase transformation and oxygen equilibration kinetics of pure and Zr-doped $\text{Ba}_{0.5}\text{Sr}_{0.5}\text{Co}_{0.8}\text{Fe}_{0.2}\text{O}_{3-\delta}$ perovskite oxide probed by electrical conductivity relaxation

### Abstract

Electrical conductivity relaxation is used for monitoring the cubic-to-hexagonal phase transition in the perovskite-type oxide  $\text{Ba}_{0.5}\text{Sr}_{0.5}\text{Co}_{0.8}\text{Fe}_{0.2}\text{O}_{3-\delta}$ . After *in-situ* annealing at 900 °C, at which temperature the cubic polymorph is stable, electrical conductivity relaxation experiments are conducted during long-term annealing at 800 °C. The decreases in the surface exchange and chemical diffusion coefficients with time due to the sluggish phase transition are found to be correlated. It is demonstrated that B-site doping with Zr to an amount as low as 3 mol% stabilizes the high-temperature perovskite cubic phase of  $\text{Ba}_{0.5}\text{Sr}_{0.5}\text{Co}_{0.8}\text{Fe}_{0.2}\text{O}_{3-\delta}$ , with preservation of its high oxygen transport and exchange properties.

## 2.1 Introduction

Mixed electronic-oxygen ionic conducting oxides, where both oxygen ions and electrons are mobile, are presently considered for the separation of oxygen from air and as fuel cell electrodes. In particular, the perovskite composition  $\text{Ba}_{0.5}\text{Sr}_{0.5}\text{Co}_{0.8}\text{Fe}_{0.2}\text{O}_{3-\delta}$  (henceforth referred to as BSCF) has attracted much interest for its potential use as oxygen transport membrane [1, 2] and intermediate-temperature solid oxide fuel cell cathode [3]. BSCF exhibits high oxygen ionic conductivity, which is related to a high concentration of mobile oxygen vacancies. The oxygen nonstoichiometry of BSCF is as high as  $\delta = 0.66$  at  $600\text{ }^\circ\text{C}$  and  $p\text{O}_2 = 1\text{ atm}$  and  $\delta = 0.81$  at  $900\text{ }^\circ\text{C}$  and  $10^{-3}\text{ atm}$  [4]. Despite superior oxygen transport properties reported for BSCF, issues regarding its long-term stability remain to be solved. The oxygen permeation flux through a BSCF membrane decreases with time when measurements are conducted below  $825\text{ }^\circ\text{C}$  [2, 5]. This effect has been attributed to a structural change in BSCF and associated segregation of secondary phases to the surface [5]. Detailed X-ray diffraction (XRD) studies after long-term annealing of BSCF have revealed that the high temperature cubic structure gradually transforms to a hexagonal phase below  $900\text{ }^\circ\text{C}$  [6, 7]. The observed sluggish kinetics of the phase transition is explained by significant structural rearrangements occurring upon transition and slow cation diffusion. Švarcová *et al.* [6] have rationalized the cubic-to-hexagonal phase transition of BSCF in terms of the radii of constituent cations through the Goldschmidt tolerance factor. The value of it depends in an intricate manner on temperature and oxygen partial pressure, determining the concentration of the oxygen vacancies and oxidation state and, hence, effective radius of the B-cations. The authors suggested that the phase transition can be avoided by appropriate substitutions of the composition of BSCF.

In the present work, we show the use of electrical conductivity relaxation (ECR) for probing the kinetics of the cubic-to-hexagonal phase transformation in BSCF. It is further demonstrated that B-site doping with Zr, to yield  $\text{Ba}_{0.5}\text{Sr}_{0.5}(\text{Co}_{0.8}\text{Fe}_{0.2})_{1-x}\text{Zr}_x\text{O}_{3-\delta}$ , to an amount as low as  $x = 0.03$ , prevents occurrence of the phase transformation.

## **2.2 Experimental**

Perovskite oxide powders with the stoichiometric compositions  $\text{Ba}_{0.5}\text{Sr}_{0.5}(\text{Co}_{0.8}\text{Fe}_{0.2})_{1-x}\text{Zr}_x\text{O}_{3-\delta}$  with  $x = 0, 0.01, 0.03, 0.05, \text{ and } 0.10$  were prepared using the spray pyrolysis technique. The powders were ball-milled and calcined at  $800\text{ }^\circ\text{C}$  for 6 h in air. Green cylinders were obtained by uniaxial pressing at 50 MPa followed by isostatic pressing at 400 MPa. Sintering was conducted at  $1050\text{ }^\circ\text{C}$  for 3 h for the parent compound and at  $1120\text{ }^\circ\text{C}$  for 30 h for the Zr-substituted samples. The relative density of the ceramics was in excess of 95%. The phase composition of the calcined powders was studied by x-ray powder diffraction (PANanalytical PW1830) with  $\text{Cu } K_\alpha$  radiation at room temperature. Scanning electron microscopy (SEM, Philips CM300ST-FEG) was used to investigate the microstructure of the sintered ceramics.

For conductivity relaxation measurements, rectangular sheets of size  $12 \times 6 \times 0.5\text{ mm}^3$  were cut out of the sintered cylinders, and the largest surfaces were polished using  $1\text{ }\mu\text{m}$  grade alumina abrasive. The electrical conductivity was measured using a four-probe dc technique during oxidation and reduction step changes in  $p\text{O}_2$  between 1 and 0.33 atm. The  $p\text{O}_2$  of the gas streams was adjusted by appropriate mixing of  $\text{N}_2$  and  $\text{O}_2$  and monitored by an oxygen sensor. The gas flow through the cell and current through the sample were kept at values of  $300\text{ ml min}^{-1}$  and 0.3 A, respectively. The electrochemical cell was designed to enable gas switching faster than 0.1 s. Detailed descriptions of the ECR technique and model used for data fitting are given elsewhere [8, 9]. Prior



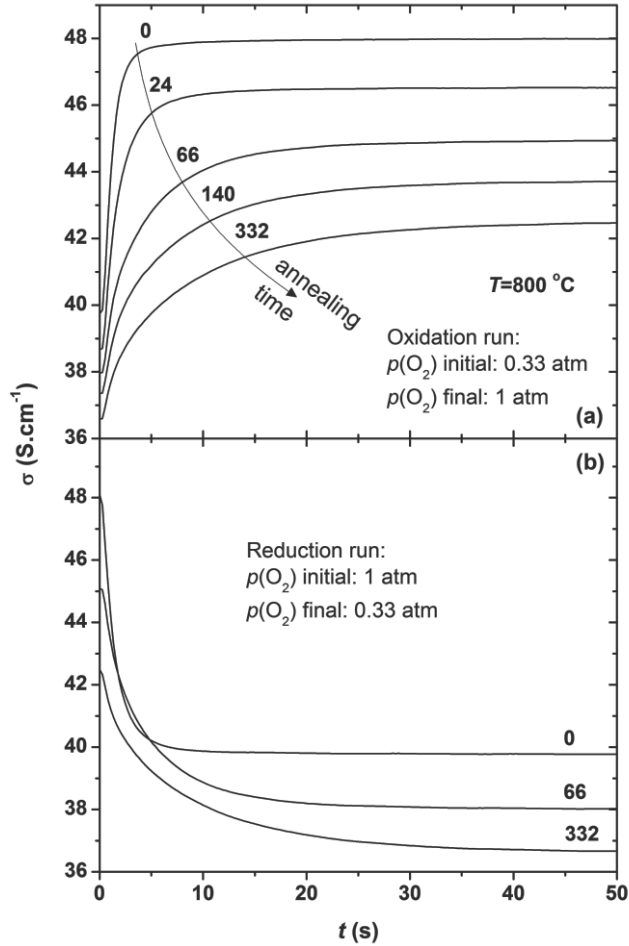
to experiments, the sample was *in-situ* annealed for 1 h at 900 °C, where the cubic phase of BSCF is known to be stable, and subsequently cooled to 800 °C with a rate of 7 °C min<sup>-1</sup>. Conductivity relaxation experiments were performed during long-term annealing at this temperature on compositions Ba<sub>0.5</sub>Sr<sub>0.5</sub>(Co<sub>0.8</sub>Fe<sub>0.2</sub>)<sub>1-x</sub>Zr<sub>x</sub>O<sub>3-δ</sub> with x = 0 and 0.03. SEM observations of the samples used for the experiments (data not shown) revealed a high quality of ceramics with no open porosity or traces of liquid phase formation during sintering.

### 2.3 Results and discussion

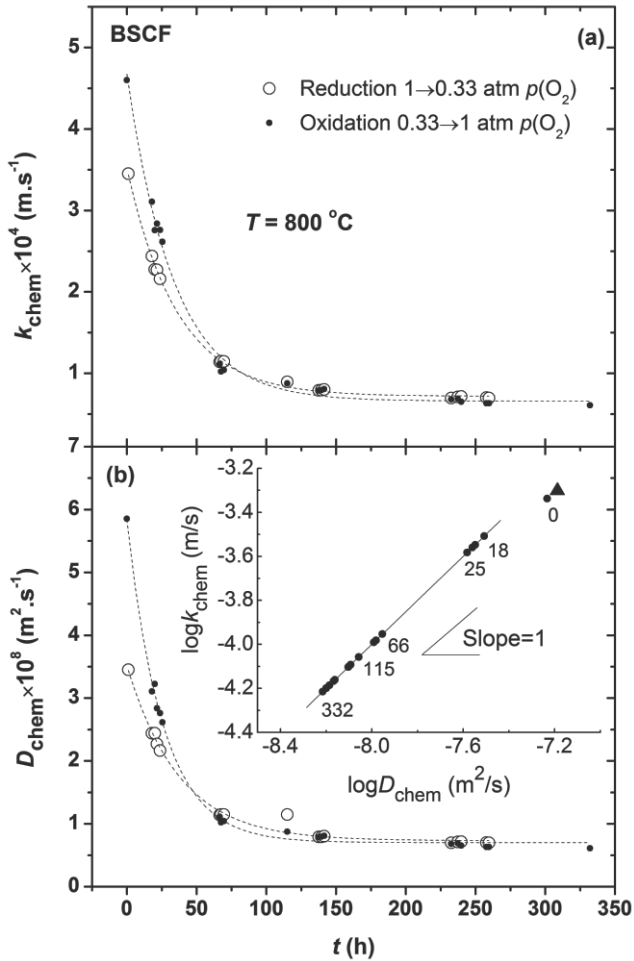
XRD analysis showed that all prepared phases possess the cubic perovskite structure. Except for the composition with the highest Zr content in this study, single phase materials were obtained. For the latter composition, XRD showed evidence of second phase formation. The cubic lattice parameters were found in compliance with Vegard's law up to the composition x = 0.05, which suggests a solid solubility limit of ZrO<sub>2</sub> in BSCF between 5 and 10 mol%. This result is in close agreement with the solid solubility limit of 10 mol% established for the dissolution of ZrO<sub>2</sub> in SrCo<sub>0.4</sub>Fe<sub>0.6-x</sub>Zr<sub>x</sub>O<sub>3-δ</sub> [10].

Fig. 2.1 shows typical conductivity relaxation curves acquired for pure BSCF ceramics during the long-term annealing at 800 °C. Both curves corresponding to reduction and oxidation runs are shown. The data demonstrate that the anneal treatment results in *i*) a slight decrease in the electrical conductivity [from 48 to 43 S cm<sup>-1</sup> at pO<sub>2</sub> = 1 atm, and from 40 to 36 S cm<sup>-1</sup> at pO<sub>2</sub> = 0.33 atm, over 332 h], and *ii*) a significant increase in the time needed for oxygen equilibration. After 332 h, the overall oxygen equilibration kinetics is about a factor of 5 slower than the initial one due to the partial transformation of the cubic to the hexagonal phase. These data are consistent with the sluggish kinetics of the cubic-to-hexagonal phase transition as evidenced by long-term

annealing studies using XRD [6, 7]. Unlike XRD, ECR is able to spur the effect of the phase transition on the oxygen equilibration kinetics already after several tenths of hours.



**Figure 2.1** Conductivity relaxation curves obtained for pure BSCF during long-term annealing at 800 °C; (a) oxidation runs [ $p\text{O}_2 = 0.33 \rightarrow 1$  atm], and (b) reduction runs [ $p\text{O}_2 = 1 \rightarrow 0.33$  atm]. Numbers denote the annealing time (in hours).



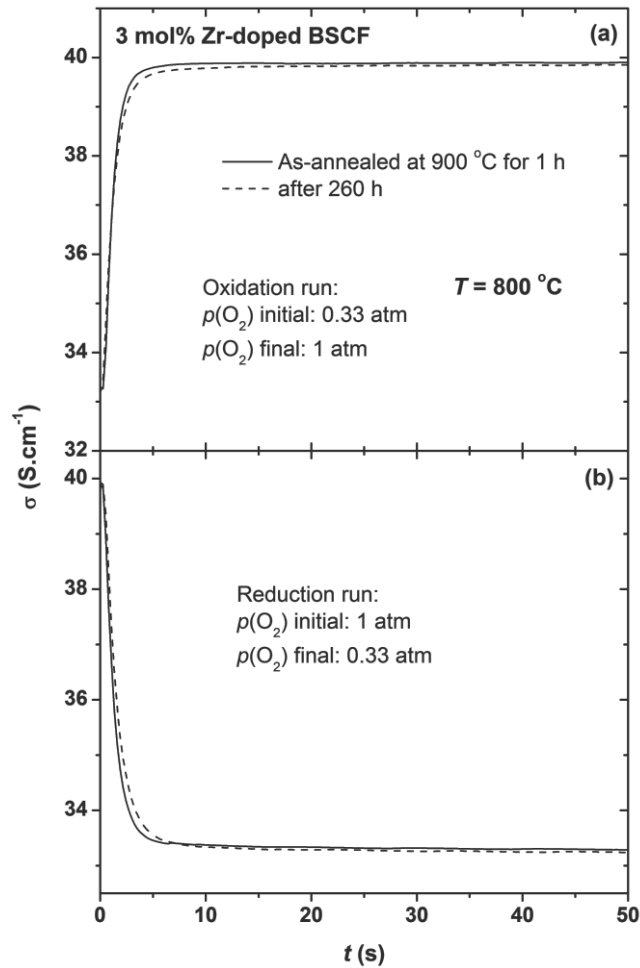
**Figure 2.2** Variation in the (a) oxygen exchange coefficient,  $k_{\text{chem}}$  and (b) chemical diffusion coefficient,  $D_{\text{chem}}$ , with time during long-term annealing of pure BSCF at  $800\text{ }^{\circ}\text{C}$ . Data are obtained from conductivity relaxation experiments on reduction (open symbols) and oxidation (filled symbols). The dashed lines are the guides to the eye. The inset shows  $\log k_{\text{chem}}$  vs  $\log D_{\text{chem}}$ . Numbers denote the annealing time (in hours). The additional data point in this figure (inset) is the corresponding value for 3 mol% Zr-doped BSCF measured at  $800\text{ }^{\circ}\text{C}$ .

Fig. 2.2 shows deconvoluted surface exchange and chemical diffusion coefficients,  $k_{\text{chem}}$  and  $D_{\text{chem}}$ , respectively, as derived from the data of ECR on BSCF as a function of the time of annealing at 800 °C. Both parameters decrease approximately a factor of 5 within the first 50 h of the experiment. It should be emphasized that both  $k_{\text{chem}}$  and  $D_{\text{chem}}$  are restored again to their initial values after 1 h annealing at 900 °C, and subsequently cooling to 800 °C. The oxygen exchange kinetics of BSCF have been studied by several researchers [11-13]. The present results clearly suggest that the partial transformation of the cubic to the hexagonal phase contributes to disparities of published data on  $k_{\text{chem}}$  and  $D_{\text{chem}}$  for BSCF.

In part, this study was conducted to determine whether the oxygen surface exchange or diffusion kinetics is affected by the cubic-to-hexagonal phase transition, or that both are affected. The observed decreases in  $k_{\text{chem}}$  and  $D_{\text{chem}}$  of BSCF with the time of annealing at 800 °C can be explained by the poor exchange and diffusion properties of the hexagonal compared with the cubic phase. To our surprise, however, the decrease in  $k_{\text{chem}}$  is found to vary linearly with the decrease in  $D_{\text{chem}}$ . The log-log plot of the values of  $k_{\text{chem}}$  versus  $D_{\text{chem}}$  measured during long-term annealing yields a slope equal to unity [see the inset in Fig. 2.2 (b)]. The surprise arises from the fact that the surface exchange is a two-dimensional process, occurring at the surface of the oxide ceramics exposed to the gas phase, whereas diffusion in the ceramic is a three-dimensional process. The present results suggest that  $k_{\text{chem}}$  versus  $D_{\text{chem}}$  derived from experiment are effective quantities, containing a common factor which is influenced by the degree of transformation of the cubic to the hexagonal phase. We are inclined to attribute the correlation between the decreases in both kinetic parameters during long-term annealing to the influence of grain boundaries on the oxygen equilibration kinetics. Formation of nuclei and growth of the hexagonal phase at the grain boundaries will restrict the overall rate of the

surface exchange reaction, and simultaneously reduce grain boundary diffusion. Preis and Sitte [14] have shown that the solution of the diffusion equation with limited surface exchange for polycrystalline materials still holds by introducing effective kinetic parameters which take into account fast diffusion and surface exchange at grain boundary regions. More research is, however, required to fully understand the observed correlation between the decreases in  $k_{\text{chem}}$  and  $D_{\text{chem}}$  upon partial transformation of the cubic to hexagonal phase in BSCF.

Fig.2.3 shows conductivity relaxation data obtained for 3 mol % Zr-doped BSCF at 800 °C. No changes in electrical conductivity and equilibration rates are observed even after an annealing time of 260 h. It is stressed here that the amount of Zr as low as 3 mol% turns out to be sufficient to prevent the cubic-to-hexagonal phase transition as observed in pure BSCF, and to preserve its high oxygen exchange and transport properties [see the inset in Fig. 2.2 (b)]. Traces of the hexagonal phase did not show up in XRD patterns of the ceramics after completion of the ECR measurements, as were found in the case of pure BSCF. Both  $k_{\text{chem}}$  and  $D_{\text{chem}}$  for 3 mol% Zr-doped BSCF show Arrhenius type of behavior, with activation energies 88 (8) and 107 (8) kJ mol<sup>-1</sup>, respectively, as extracted from ECR data (oxidation runs) in the range 650-800 °C.



**Figure 2.3** Conductivity relaxation curves obtained for 3 mol% Zr-doped BSCF during long-term annealing at 800 °C immediately after annealing at 900 °C and after 260 h; (a) oxidation runs [ $p\text{O}_2 = 0.33 \rightarrow 1$  atm], and (b) reduction runs [ $p\text{O}_2 = 1 \rightarrow 0.33$  atm].

## 2.4 Conclusions

In conclusion, the kinetics of the cubic-to-hexagonal phase transition occurring in BSCF at moderate temperatures has been monitored using ECR. The sluggish kinetics of the phase transformation at 800 °C results in an associated fivefold drop of the values of  $k_{\text{chem}}$  and  $D_{\text{chem}}$  within the first 50 h. Of notable surprise is the one-to-one correlation in the decreases in the apparent values of the surface exchange and chemical diffusion coefficients. It is further shown that doping of BSCF with  $\text{ZrO}_2$  as low as 3 mol% is effective in stabilizing the high-temperature cubic phase with preservation of the high oxygen transport and exchange properties of BSCF as demonstrated in conductivity relaxation experiments at 800 °C during extended annealing over a time of 260 h.

## References

1. J. Vente, S. McIntosh, W. Haije, H. Bouwmeester, *J. Solid State Electrochem* 10 (2006) 581.
2. Z. Shao, W. Yang, Y. Cong, H. Dong, J. Tong, G. Xiong, *J. Membrane. Sci.* 172 (2000) 177.
3. Z. Shao, S.M. Haile, *Nature* 431 (2004) 170.
4. S. McIntosh, J.F. Vente, W.G. Haije, D.H.A. Blank, H.J.M. Bouwmeester, *Chem. Mater.* 18 (2006) 2187.
5. H. Lu, Y. Cong, W.S. Yang, *Solid State Ionics* 177 (2006) 595.
6. S. Švarcová, K. Wiik, J. Tolchard, H.J.M. Bouwmeester, T. Grande, *Solid State Ionics* 178 (2008) 1787.
7. M. Arnold, T.M. Gesing, J. Martynczuk, A. Feldhoff, *Chem. Mater.* 20 (2008) 5851.
8. J.E. ten Elshof, M.H.R. Lankhorst, H.J.M. Bouwmeester, *J. Electrochem. Soc.* 144 (1997) 1060.
9. M.W. den Otter, A study of oxygen transport in mixed conducting oxides using isotopic exchange and conductivity relaxation, Ph D thesis, University of Twente (2000).
10. L. Yang, L. Tan, X. Gu, W. Jin, L. Zhang, N. Xu, *Ind. Eng. Chem. Res.* 42 (2003) 2299.
11. E. Bucher, A. Egger, P. Ried, W. Sitte, P. Holtappels, *Solid State Ionics* 179 (2008) 1032.
12. E. Girdauskaite, H. Ullmann, V. V. Vashook, U. Guth, G. B. Caraman, E. Bucher, W. Sitte, *Solid State Ionics* 179 (2008) 385.
13. B. Wei, Z. Lü, X. Huang, J. Miao, X. Sha, X. Xin, W. Su, *J. Eur. Ceram. Soc.* 26 (2006) 2827.
14. W. Preis, W. Sitte, *J. Phys. Chem. Solids* 66 (2005) 1820.



### Note Added in Proof

In follow-up research, it was found by means of scanning electron microscopy and energy dispersive X-ray analysis that the ceramic specimens used for electrical conductivity relaxation (ECR), *i.e.*, after completion of the measurements, were partially covered with BaSO<sub>4</sub> crystals. After dedicated testing, the origin of the sulfur appeared to be the sulfur-containing binder in the conductive gold paste (Alfa Aesar GmbH, Germany, LOT number: D13R009) used to improve the electrical connections. Since it cannot be excluded that the results are influenced by the sulfur contamination selected experiments were conducted again, using sulfur-free gold paste instead, in order to verify and re-evaluate, if necessary, the results presented in this chapter, being published in *App. Phys. Lett.* 96 (2010) 254101.

Typical normalized conductivity relaxation curves for parent BSCF and 3 mol% Zr-doped BSCF (BSCFZ3) ceramics recorded during long-term annealing in pure oxygen, at 800 °C, are given in Fig. 2.A.1. The experiments were conducted similarly as described in the main text, using rather sulfur-free gold paste (MaTeck GmbH, Germany, catalogue number: 902949) to improve the electrical connections in the electrochemical cell. The chemical exchange ( $k_{\text{chem}}$ ) and diffusion ( $D_{\text{chem}}$ ) coefficients extracted from the experiments as well as the apparent correlation found between both parameters, as displayed in Fig. 2.A.2., are found to be in excellent agreement with the previous findings (see corresponding figures in the main text). X-ray diffraction patterns of the ceramic specimens recorded after completion of the long-term (200 h) ECR tests are shown in Fig. 2.A.3. Evidence is found for the formation of hexagonal polymorphs in BSCF, but not in 3 mol% Zr-doped BSCF. At present, ongoing research is directed towards confirmation of the apparent phase stability of Zr-doped BSCF at different temperatures using scanning electron mi-

croscopy (SEM) and high-resolution transmission electron microscopy (HRTEM).

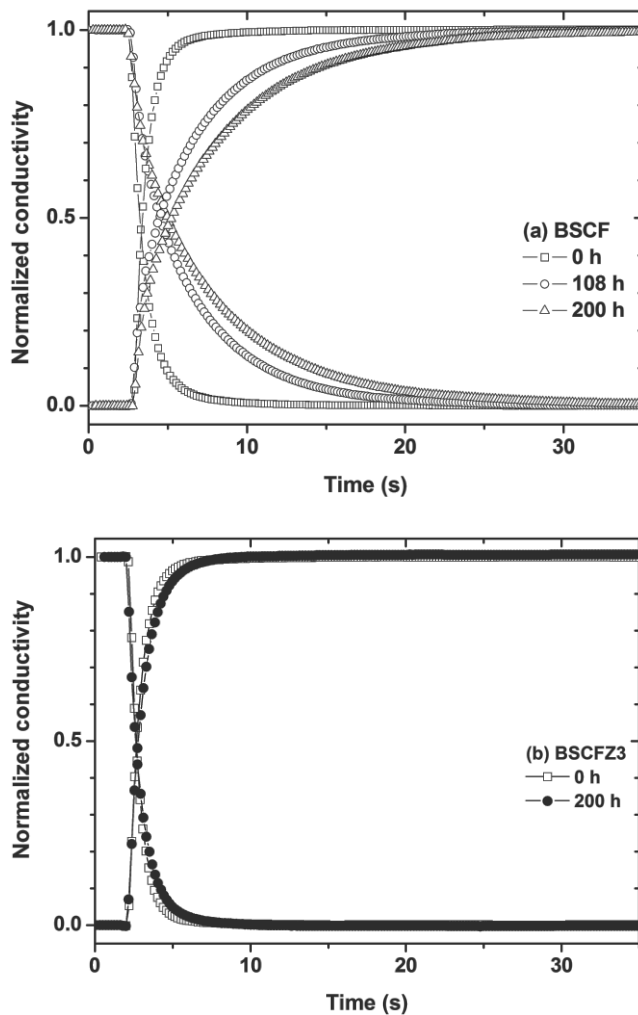


**Figure 2.A.1** Typical normalized conductivity relaxation curves for (a) BSCF and (b) 3 mol% Zr-doped BSCF (BSCFZ3) recorded during long-term annealing, at 800 °C, in flowing oxygen. Results from both reduction and oxidation step changes in  $pO_2$  are shown (from  $pO_2 = 1$  atm to  $pO_2 = 0.33$  atm, and *vice versa*).

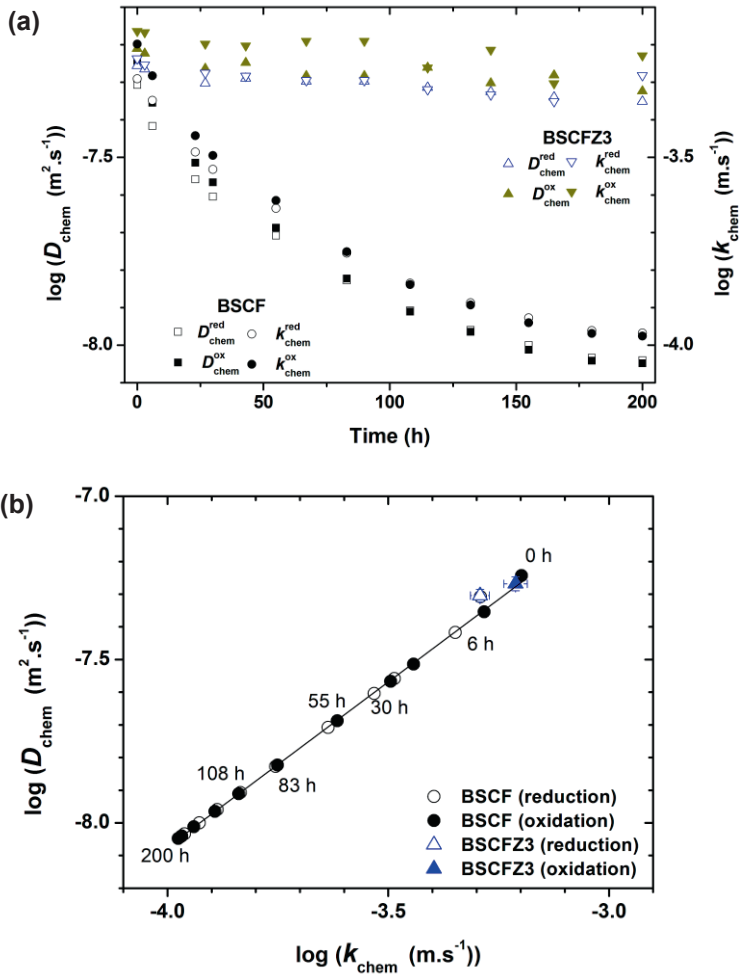


**Figure 2.A.2** (a)  $D_{\text{chem}}$  and  $k_{\text{chem}}$  as a function of time, and (b)  $\log D_{\text{chem}}$  vs  $\log k_{\text{chem}}$  for BSCF and 3 mol% Zr-doped BSCF (BSCFZ3). Parameters extracted from data of conductivity relaxation experiments during long-term annealing, at 800 °C, in flowing oxygen. Results from reduction and oxidation step changes in  $p\text{O}_2$  are shown (from  $p\text{O}_2 = 1 \text{ atm}$  to  $p\text{O}_2 = 0.33 \text{ atm}$ , and *vice versa*).

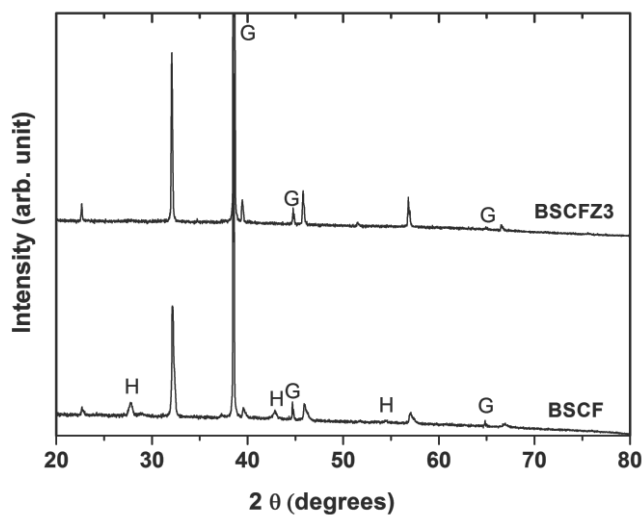


**Figure 2.A.3** X-ray diffraction patterns of BSCF and 3 mol% Zr-doped BSCF (BSCFZ3) ceramics recorded after long-term (200 h) electrical conductivity relaxation experiments, at 800 °C, in flowing oxygen (G: gold, and H: 2H hexagonal phase).



---

## Chapter 3

# Performance and stability of niobium-substituted $\text{Ba}_{0.5}\text{Sr}_{0.5}\text{Co}_{0.8}\text{Fe}_{0.2}\text{O}_{3-\delta}$ membranes

### Abstract

The phase stability, thermal expansion, electrical conductivity, and oxygen permeation of perovskite-type oxides  $\text{Ba}_{0.5}\text{Sr}_{0.5}(\text{Co}_{0.8}\text{Fe}_{0.2})_{1-x}\text{Nb}_x\text{O}_{3-\delta}$  ( $x = 0-0.2$ ) have been investigated. Room-temperature X-ray diffraction of as-prepared powders indicates that in the investigated compositional range solid solutions are formed. Long-term annealing experiments both in flowing air and nitrogen, at 750 °C, demonstrate that the phase instability observed in parent  $\text{Ba}_{0.5}\text{Sr}_{0.5}\text{Co}_{0.8}\text{Fe}_{0.2}\text{O}_{3-\delta}$  (BSCF) is suppressed already at the minimum substitution of 5 mol% of niobium for (Co,Fe). Both electrical conductivity and thermal expansion are found to decrease with increasing niobium concentration, which behaviors can be explained by defect chemical considerations, taking into account charge compensation mechanisms by doping BSCF with  $\text{Nb}^{5+}$  donor cations. The oxygen permeation flux of 10 mol% Nb-substituted BSCF, in the range 800-900 °C, is reduced by 10% relative to that found for parent BSCF. Switching from helium to a  $\text{CO}_2$ -containing purge gas results in a severe reduction or cessation of the oxygen flux. Options are discussed to avoid undesired formation of surface carbonates.

### 3.1 Introduction

Mixed ionic and electronic conducting  $ABO_{3-\delta}$  perovskite-type oxides have attracted much interest for potential applications as oxygen separation membranes and as cathodes in solid oxide fuel cells (SOFCs). Among the perovskite oxides under intensive research and development is  $Ba_{0.5}Sr_{0.5}Co_{0.8}Fe_{0.2}O_{3-\delta}$  (BSCF). Although being a predominant electronic conductor, BSCF displays fast oxide-ion conduction owing to its extraordinarily high concentration of mobile oxygen vacancies [1-3]. The oxygen nonstoichiometry can be as high as  $\delta \approx 0.8$  at  $900\text{ }^\circ\text{C}$  and  $pO_2 = 10^{-3}$  atm, while a cubic perovskite structure is still retained [1]. As a consequence, excellent performance has been demonstrated using BSCF both as an oxygen separation membrane and as a SOFC cathode [4, 5].

In their pioneering study on oxygen permeation through  $La_{1-x}Sr_xCo_{1-y}Fe_yO_{3-\delta}$  membranes, Teraoka *et al.* [6] found the highest oxygen flux for  $SrCo_{0.8}Fe_{0.2}O_{3-\delta}$ . Ionic charge compensation upon A-site substitution of divalent Sr for trivalent La induces formation of oxygen vacancies, which become mobile at elevated temperatures. The cubic perovskite structure  $SrCo_{0.8}Fe_{0.2}O_{3-\delta}$  is stabilized by the substitution of 20 mol% iron for cobalt at the B-site, noting that the end-member in the series,  $SrCoO_{3-\delta}$ , transforms under air at  $\sim 940\text{ }^\circ\text{C}$  from a cubic to a non-perovskite phase with hexagonal symmetry (2H structure) with face-shared octahedra [7]. Other studies have, however, demonstrated that  $SrCo_{0.8}Fe_{0.2}O_{3-\delta}$  undergoes a transition to a vacancy-ordered brownmillerite phase below a  $pO_2$  of 0.01 atm at  $\sim 790\text{ }^\circ\text{C}$  [8, 9]. The undesirable ordering of the oxygen vacancies, which reduces the rate of oxygen permeation, can be suppressed by partial substitution of barium for strontium [4, 9, 10]. Enhanced ionic over electronic charge compensation of the divalent A-site cations, induced by substituting barium for strontium, is found to increase further the concentration of oxygen vacancy defects relative to that in parent

$\text{SrCo}_{0.8}\text{Fe}_{0.2}\text{O}_{3-\delta}$ , as demonstrated by *in-situ* neutron diffraction experiments at elevated temperatures [9]. The influence of Ba-substitution on the oxygen permeation rate of  $\text{SrCo}_{0.8}\text{Fe}_{0.2}\text{O}_{3-\delta}$  has been investigated by Shao *et al.* [4].

The partial substitution of barium (1.61 Å) for the smaller-sized strontium (1.44 Å) cations in  $\text{SrCo}_{0.8}\text{Fe}_{0.2}\text{O}_{3-\delta}$ , however, affects the relative stability of the cubic perovskite phase. Recent studies by means of X-ray diffraction (XRD) and transition electron microscopy (TEM) give evidence of a miscibility gap in the phase diagram associated with BSCF, transforming the high-temperature cubic perovskite phase into a mixture of cubic and hexagonal phases [11-14]. The slow, but reversible, phase transformation process causes the oxygen permeation rate of BSCF to deteriorate with time when operated below the critical temperature of  $\sim 850$  °C [14-16]. Another problem encountered relates to a poor stability of BSCF in  $\text{CO}_2$ -containing environments due to carbonate formation (and concomitant decomposition of the perovskite phase) [17-19].

In the present study, we have investigated the effect of partial substitution of niobium for both cobalt and iron on phase stability, thermal expansion, electrical conductivity, and oxygen permeation of BSCF.

### **3.2 Experimental**

Powders of  $\text{Ba}_{0.5}\text{Sr}_{0.5}(\text{Co}_{0.8}\text{Fe}_{0.2})_{1-x}\text{Nb}_x\text{O}_{3-\delta}$  with  $x = 0.05, 0.10, 0.15,$  and  $0.2$  (abbreviated as BSCFN05, -10, -15, and -20, respectively) were prepared by solid state reaction. Stoichiometric amounts of  $\text{BaCO}_3, \text{SrCO}_3, \text{Co}_3\text{O}_4, \text{Fe}_2\text{O}_3,$  and  $\text{Nb}_2\text{O}_5$  (Sigma-Aldrich, > 99%) were ball-milled in isopropanol for 24 h. The powder mixtures were dried, calcined in air at 950 and 1000 °C for 10 h at each temperature with intermediate milling in a mortar for 2 h, and subsequently cooled with  $3$  °C  $\text{min}^{-1}$  to room temperature. Pure  $\text{Ba}_{0.5}\text{Sr}_{0.5}\text{Co}_{0.8}\text{Fe}_{0.2}\text{O}_{3-\delta}$  (BSCF) powder prepared by solid state reaction was



obtained from the Fraunhofer Institute for Ceramic Technologies and Systems (IKTS).

The chemical composition of the powders was analyzed by X-ray fluorescence (XRF, Philips PW1480). The phase stability of Nb-substituted BSCF was investigated by long-term annealing powders, at 750 °C, either in flowing air for 240 h or nitrogen for 100 h. Prior to long-term annealing, the powders were annealed in air at 1100 °C for 10 h. X-ray powder diffraction (XRD) patterns were recorded at room temperature using a Philips PANalytical PW1830 diffractometer. Lattice parameters were indexed and refined using the FullProf program [20].

Powders of the different compositions were uniaxially pressed ( $\varnothing = 20$  mm) at 50 MPa followed by isostatic pressing at 400 MPa for 3 min. The obtained pellets were sintered in air at temperatures 1170-1190 °C for 10 h using heating and cooling rates of 1 °C min<sup>-1</sup>. Densities of the sintered pellets ( $\varnothing = 15.5$  mm) were measured by the Archimedes method in mercury. The microstructure of the dense ceramics was examined by scanning electron microscopy (SEM, JEOL JSM-5600LV). Thermal expansion was measured on sintered cylindrical samples ( $\varnothing = 6$  mm, length 12 mm) using a Netzsch Dil-402C dilatometer. Measurements were conducted in air, at a heating rate of 3 °C min<sup>-1</sup>, from room temperature up to 1050 °C. For electrical conductivity measurements, rectangular sheets of size 12 × 6 × 0.5 mm<sup>3</sup> were cut from the sintered pellets and polished with 1 μm grade alumina abrasive. Measurements were conducted isothermally, under flowing air (300 ml min<sup>-1</sup>) by a 4-probe DC technique using Au electrodes at a current of 300 mA supplied by a Keithley 2400 source meter. The temperature was incremented stepwise, with a heating rate of 7 °C min<sup>-1</sup>, from room temperature up to 900 °C. At each tem-

perature step, the sample was allowed to equilibrate for at least 1 h prior to data acquisition.

For oxygen permeation measurements, the sintered pellets were shaped into discs ( $\varnothing = 15$  mm) and polished with 120, 240, 600, and 1200 mesh SiC sandpaper to a final thickness of 1 mm. Glass rings were used to seal the disc membrane into a quartz reactor by holding at a temperature of 1020 °C for 30 min. The temperature of the disc was monitored by a thermocouple. After sealing, the membrane was cooled to 900 °C. Synthetic air and high purity He were fed to opposite sides of the membrane at flow rates of 100 and 50 ml min<sup>-1</sup>, respectively. Permeation measurements were conducted sequentially at 900, 875, 850, 825 and 800 °C. The oxygen flux was measured for 5 h at each temperature. Post-test inspection using a light microscope revealed no obvious evidence for a reaction between the glass ring and the ceramic membrane. In order to investigate the effect of CO<sub>2</sub> on oxygen permeation, the sweep gas was switched from He to a He/CO<sub>2</sub> gas mixture or pure CO<sub>2</sub>. Gas flow rates were controlled using mass flow controllers (Brooks, 5850s). The effluent gas was analyzed by on-line gas chromatography (Varian, CP4900). The gas chromatograph, equipped with a 5 Å molecular sieve column, using He as carrier gas, was calibrated using standard gas mixtures (O<sub>2</sub>, N<sub>2</sub> in He). Gas leakage, if present, could be monitored by measuring the concentration of nitrogen in the sweep gas, and was found normally below 1%. Permeation data were corrected for leakage, assuming defects and/or pinholes to be non-selective for gas leakage. A detailed description of the experimental set-up used for oxygen permeation measurements is given elsewhere [21].

### 3.3 Results and discussion

#### 3.3.1 Structure and phase analysis

Chemical compositions of the calcined powders determined by XRF are listed in Table 3.1. These match well with their nominal compositions, albeit that the cobalt contents are slightly lower than that in the corresponding nominal compositions probably due to cobalt evaporation during the calcination procedure (see experimental section).

**Table 3.1** Composition and lattice parameters of BSCFN05, BSCFN10, BSCFN15, and BSCFN20.

Nominal composition	$\text{Ba}_{0.50}\text{Sr}_{0.50}\text{Co}_{0.76}\text{Fe}_{0.19}\text{Nb}_{0.05}\text{O}_{3-\delta}$	$\text{Ba}_{0.50}\text{Sr}_{0.50}\text{Co}_{0.72}\text{Fe}_{0.18}\text{Nb}_{0.10}\text{O}_{3-\delta}$	$\text{Ba}_{0.50}\text{Sr}_{0.50}\text{Co}_{0.68}\text{Fe}_{0.17}\text{Nb}_{0.15}\text{O}_{3-\delta}$	$\text{Ba}_{0.50}\text{Sr}_{0.50}\text{Co}_{0.64}\text{Fe}_{0.16}\text{Nb}_{0.20}\text{O}_{3-\delta}$
XRF results	$\text{Ba}_{0.500}\text{Sr}_{0.502}\text{Co}_{0.749}\text{Fe}_{0.186}\text{Nb}_{0.05}\text{O}_{3-\delta}$	$\text{Ba}_{0.500}\text{Sr}_{0.502}\text{Co}_{0.710}\text{Fe}_{0.176}\text{Nb}_{0.10}\text{O}_{3-\delta}$	$\text{Ba}_{0.500}\text{Sr}_{0.503}\text{Co}_{0.666}\text{Fe}_{0.166}\text{Nb}_{0.15}\text{O}_{3-\delta}$	$\text{Ba}_{0.500}\text{Sr}_{0.503}\text{Co}_{0.629}\text{Fe}_{0.156}\text{Nb}_{0.20}\text{O}_{3-\delta}$
Lattice parameter (Å)	3.9880 (2)	3.9896 (2)	3.9906 (3)	3.9914 (2)
Lattice volume (Å <sup>3</sup> )	63.425 (7)	63.501(6)	63.545 (4)	63.586 (5)

$\text{Ba}_{0.5}\text{Sr}_{0.5}(\text{Co}_{0.8}\text{Fe}_{0.2})_{1-x}\text{Nb}_x\text{O}_{3-\delta}$  form solid solutions over the investigated range of Nb-substitution. XRD patterns of the calcined powders collected at room temperature are shown in Fig. 3.1. Diffraction peaks could be indexed on the basis of the cubic perovskite structure. No evidence was found from XRD for second phase formation in each of the compositions. Corresponding lattice parameters from refinement are listed in Table 3.1. The lattice parameter is found to increase with Nb content, which is expected in view of the larger ionic radius of  $\text{Nb}^{5+}$ , 0.64 Å (in 6-fold coordination) relative to that of  $\text{Co}^{3+}$ , 0.61 Å and 0.545 Å, in high- and low-spin configuration, respectively, or  $\text{Co}^{4+}$ ,

0.53 Å in high-spin configuration [22], ignoring the possible presence of  $\text{Co}^{2+}$ -ions (0.65 Å and 0.745 Å, in high- and low-spin configuration, respectively) in the room temperature structure of BSCF. An average oxidation state of 3.4 for (Co, Fe) can be calculated from data of oxygen nonstoichiometry of BSCF powder slowly cooled to room temperature [23], whilst data from X-ray photoelectron spectroscopy entirely discard the presence of  $\text{Co}^{2+}$  [24]. In view of these observations, it is reasonable to assume that the partial substitution of  $\text{Co}^{2+}$  by  $\text{Nb}^{5+}$ , relative to the substitutions of  $\text{Co}^{3+}$  and  $\text{Co}^{4+}$  by  $\text{Nb}^{5+}$ , will only give a small or negligible contribution to the observed change in the lattice parameter.

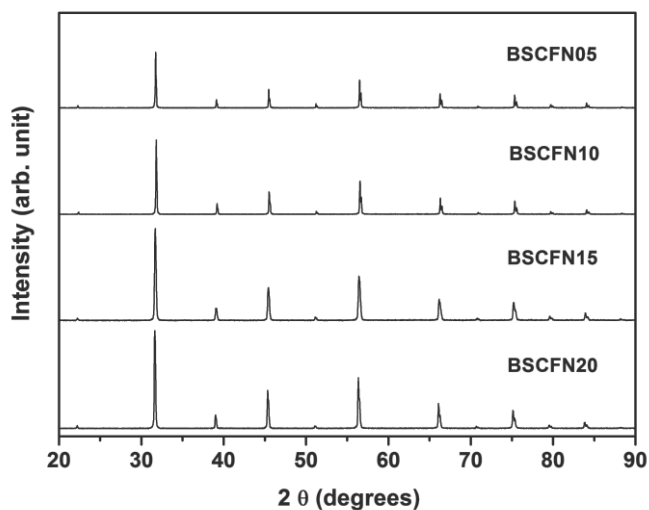


**Figure 3.1** X-ray powder diffraction patterns of niobium-substituted BSCF compositions collected at room temperature.

The SEM images of sintered discs of BSCFN05, - 10, - 15, and - 20 display many pores (Fig. 3.2). The corresponding relative densities measured by the Archimedes method are 89, 93, 95, and 96%, respectively, which agree

with estimated values from the corresponding SEM images. All samples, except BSCFN05, were found to be gas-tight, enabling oxygen permeation measurements.

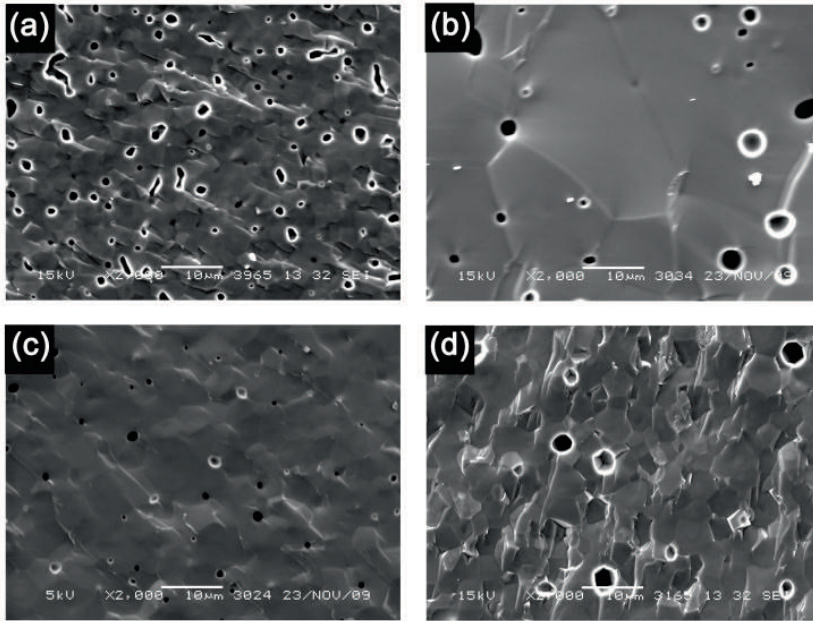


**Figure 3.2** Cross-sectional SEM images of sintered membranes of (a) BSCFN05, (b) BSCFN10, (c) BSCFN15, and (d) BSCFN20.

### 3.3.2 Phase stability

Fig. 3.3 (a) and (b) shows XRD patterns of powders annealed, at 750 °C, in air for 240 h and in N<sub>2</sub> for 100 h, respectively. Peaks corresponding to a hexagonal phase are observed in the XRD patterns of BSCF powders annealed in both atmospheres, consistent with previous reports [11] and [12], but none in those obtained for the Nb-substituted compositions. The relative stability of cubic and hexagonal perovskite polymorphs is often rationalized by means of

calculation of the Goldschmidt tolerance factor,  $t = (r_A + r_O) / [\sqrt{2}(r_B + r_O)]$ , where  $r_A$ ,  $r_B$ , and  $r_O$  are the radii of the A- and B-site cations and the oxygen anions in the ideal  $ABO_3$  perovskite structure. As stated by Goldschmidt [25],

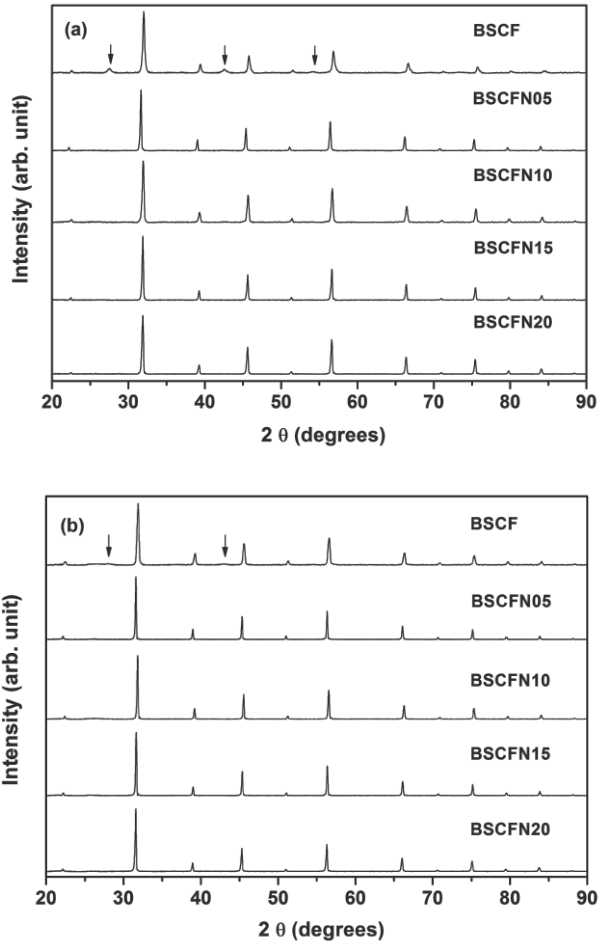


**Figure 3.3** X-ray powder diffraction patterns of BSCF and niobium-substituted BSCF collected at room temperature after prolonged annealing in (a) air at 750 °C for 240 h, and (b) nitrogen at 750 °C for 100 h. Reflections of the evolving hexagonal phase are denoted by arrows.

the cubic perovskite structure is preferred when  $t$  is between 0.8 and 1, whilst for  $t > 1$  formation of the hexagonal structure is preferred. Decreasing the ionic radius of the B-site ion thus favors formation of the hexagonal polymorph. The oxidation states of Co and Fe, and, hence, their ionic radii vary with temperature and oxygen partial pressure. Since the reduced cations tend to be larger in size than their oxidized forms, their presence will favor formation of the cubic perovskite polymorph at high temperatures. It is challenging to predict the stability window of the cubic perovskite phase of Nb-substituted BSCF in terms of temperature, oxygen partial pressure and Nb-substitution level, since calculation of  $t$  in the presence of mixed occupancy of A and B-sites, different valencies and spin states of Co and Fe ions, and oxygen deficiency is not straight-forward and unambiguous. The mere conclusion from the above observations is that substitution of 5 mol% Nb for (Co,Fe) in BSCF is effective in stabilization of the cubic perovskite phase under the conditions covered in this work. It should be mentioned that in previous research we demonstrated that the inherent phase stability of BSCF at moderate temperatures could be overcome by B-site doping with  $Zr^{4+}$  (0.72 Å) to an amount as low as 3 mol% [26]. Excellent stability was found during conductivity relaxation experiments conducted during long-term annealing at 800 °C. Since the phase transformation in BSCF is rather complex and likely involves complex reconstructive structural reorganizations, associated with long-range diffusion of cations [14], the role of kinetic factors and meta-stability of the cubic polymorph at moderate temperatures cannot be excluded.

### 3.3.3 Thermal expansion

Fig. 3.4 shows the thermal expansion behavior of compositions  $Ba_{0.5}Sr_{0.5}(Co_{0.8}Fe_{0.2})_{1-x}Nb_xO_{3-\delta}$ , with  $x = 0, 0.05, 0.10, 0.15,$  and  $0.2$ , measured by dilatometry. Due to equilibration with the ambient air at elevated tempera-

tures, two regions can be identified. In the low-temperature region, 200-500 °C, the thermal expansion coefficients (TECs) are found to vary between  $9 \times 10^{-6}$  and  $11 \times 10^{-6} \text{ °C}^{-1}$ , as shown in the inset of Fig. 3.4. In the high-temperature region, 500-1050 °C, the TECs are comparatively high, varying between

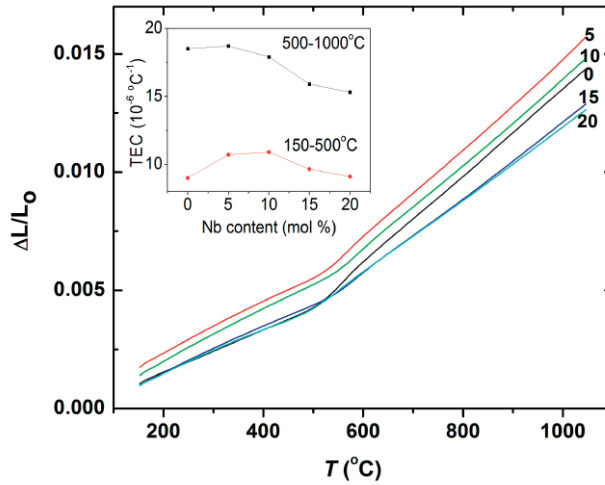


**Figure 3.4** Thermal linear expansion for  $\text{Ba}_{0.5}\text{Sr}_{0.5}(\text{Co}_{0.8}\text{Fe}_{0.2})_{1-x}\text{Nb}_x\text{O}_{3-\delta}$  heated in flowing air (at  $3 \text{ °C min}^{-1}$ ). The inset shows the calculated thermal expansion coefficient (TEC) as a function of Nb-content in different temperature regions. Numbers in the figure denote the mole percentage (mol%) of Nb.

$16 \times 10^{-6}$  and  $19 \times 10^{-6} \text{ °C}^{-1}$ . The increase in TEC above 500 °C is due to equilibration of the oxide with the ambient atmosphere, *i.e.*, the chemical expansion associated with the release of lattice oxygen, and the concomitant reduction of the cobalt and iron ions [1, 3]. The change-over temperature between the two regions will be strongly influenced by the sample's ability to exchange oxygen with the surroundings, and, hence, by sample dimensions and heating rate. The total expansion, thermal plus chemical, in the high-temperature region is found to decrease with increasing niobium content, and reflects the



non-redox active nature of the niobium cations [27]. The variation of the TEC with niobium content in the low-temperature region, where the oxygen stoichiometries are frozen-in, is not well understood, but may depend on the conditions maintained during cooling and the oxygen equilibration kinetics of the samples.

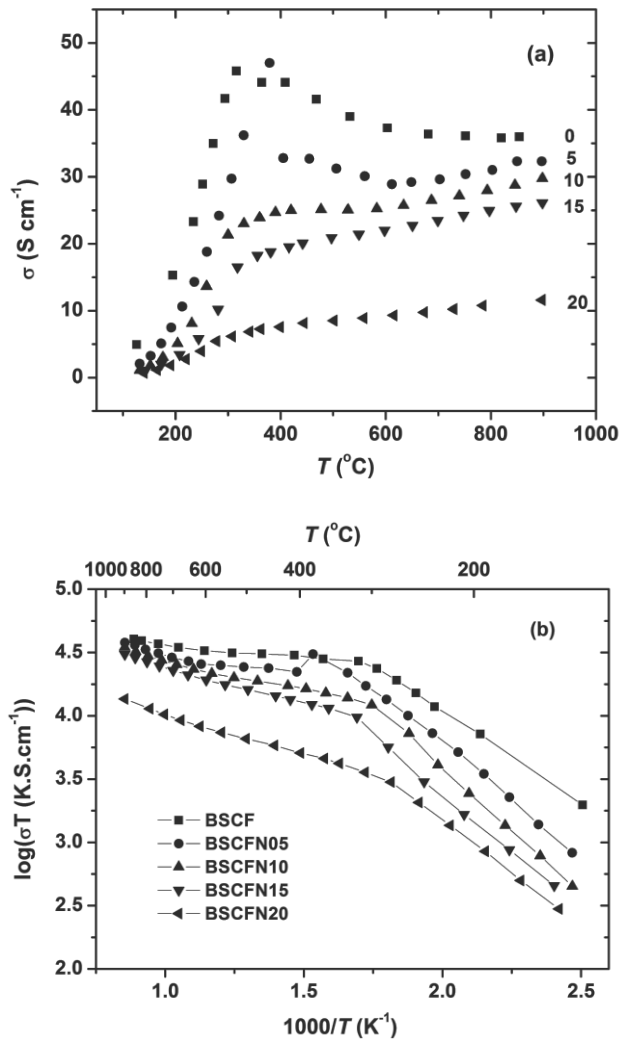
### 3.3.4 Electrical conductivity

Fig. 3.5 shows Arrhenius plots of the total electrical conductivities of  $\text{Ba}_{0.5}\text{Sr}_{0.5}(\text{Co}_{0.8}\text{Fe}_{0.2})_{1-x}\text{Nb}_x\text{O}_{3-\delta}$  ( $x = 0, 0.05, 0.10, 0.15,$  and  $0.2$ ) in air. Due to the equilibration with ambient air at elevated temperatures, again two regions can be identified that are characterized by different activation energies. The change-over temperatures for each of the compositions are, however, different from those observed in the data from dilatometry (see Fig. 3.4), which is attributed to differences in the data acquisition of both methods. While the dilatometric measurements were carried out on (6 mm ( $\varnothing$ )  $\times$  12 mm) cylindrical specimens, using a constant heating rate of  $3\text{ }^\circ\text{C min}^{-1}$ , the conductivity measurements were performed isothermally, allowing the sample ( $12 \times 6 \times 0.5\text{ mm}^3$ ) to equilibrate at least 1 h before data collection. The discrepancy in the change-over temperature between regions in the data from electrical conductivity and dilatometric measurements will depend on applied heating rate and dimensions of the specimen used in the latter type of experiment. No attempt was made to investigate this any further as similar observations have been published in other reports, for example, see Refs [28, 29].

In the following discussion, the ionic contribution to the total electrical conductivity is neglected. The latter is considered reasonable, at least for BSCF. Using data of oxygen permeation measurements, Lu *et al.* [30] extracted values for the ionic conductivity of BSCF, in the range 700-850  $^\circ\text{C}$ , of 0.53-

$1.17 \text{ S cm}^{-1}$ , which are one to two orders of magnitudes below values for the electrical conductivity at corresponding temperatures.

Data from electrical conductivity, thermal power and oxygen nonstoichiometry of pure BSCF support *p*-type small polaron hopping between  $(\text{Co,Fe})^{4+}$  and  $(\text{Co,Fe})^{3+}$  cations [31, 32]. In the low-temperature region, *i.e.*, at frozen-in oxygen nonstoichiometries, the *p*-type charge carrier concentration is constant while the mobility of the carrier is thermally activated. The activation energy of the conductivity in this region thus reflects that of the mobility of the small polarons. Apparent activation energies calculated from the data shown in Fig. 3.5, in the range 100–340 °C, are 0.25, 0.33, 0.36, 0.31, and 0.29 eV for BSCF and BSCFN05, -10, -15, and -20, respectively. Above  $\sim 340$  °C, where the oxygen equilibration kinetics are fast enough, the formation of oxygen vacancies results in an effective decrease of the carrier concentration. In this temperature region, changes in the polaron mobility counteract with changes in the carrier concentration. In the case of BSCF, this leads to an apparent maximum in the conductivity at the change-over temperature of  $\sim 340$  °C (see Fig. 3.5 (a)). The substitution of  $\text{Nb}^{5+}$  ions, acting as a donor in BSCF, compensates the divalent  $(\text{Ba,Sr})^{2+}$  acceptor ions, and forces a net lowering in the concentration of oxygen vacancies and that of *p*-type carriers. As a consequence, as seen from Fig. 3.5, the electrical conductivity is lowered by increasing the level of Nb-substitution in BSCF. The electrical conductivities of Nb-substituted BSCF specimens are rather low, noting that conductivities of at least  $100 \text{ S cm}^{-1}$  are required for use as cathodes in SOFCs.



**Figure 3.5** Temperature dependence of the electrical conductivity ( $\sigma$ ) of  $\text{Ba}_{0.5}\text{Sr}_{0.5}(\text{Co}_{0.8}\text{Fe}_{0.2})_{1-x}\text{Nb}_x\text{O}_{3-\delta}$  measured in air: (a) linear plot, and (b) Arrhenius plot. Numbers in (a) denote the mole percentage (mol%) of Nb.

### 3.3.5 Oxygen permeation

In view of the prevailing electronic conductivity of BSCF, the rate of oxygen permeation is dominated by its ionic conductivity. The data of oxygen permeation measurements from this study confirm the lowering in oxygen vacancy concentration and, hence, in ionic conductivity of BSCF upon partial substitution of (Co,Fe) by Nb. Fig. 3.6 shows that under identical conditions of temperature and flow rates of purge gases, the oxygen flux of BSCFN20 is lower by almost 65% relative to that observed for the parent BSCF phase. For BSCFN10, the lowering in oxygen flux is only ~10% relative to that of BSCF. Due to problems encountered in the densification of BSCFN05 ceramics, permeation measurements were not performed for this composition. Furthermore, as mentioned in the Introduction section, the oxygen permeation rate of the parent BSCF phase is subject to degradation when operated below ~850 °C [11, 12, 14, 15].

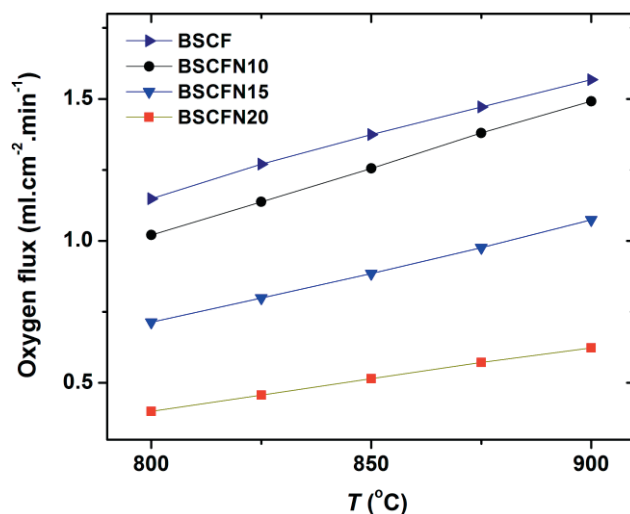


**Figure 3.6** Temperature dependence of the oxygen permeation flux of BSCF, BSCFN10, BSCFN15, and BSCFN20. Membrane thickness: 1 mm, feed gas: air (100 ml min<sup>-1</sup>), sweep gas: He (50 ml min<sup>-1</sup>).

As an example, the oxygen flux at 750 °C is found to deteriorate about 50% after 240 h [14]. In the present study, the oxygen flux was allowed to equilibrate for a few hours at each temperature set-point before actual data acquisition. For pure BSCF, the degradation of the oxygen flux within these equilibration periods was within 1-2%. Consistent with the results from XRD (See Section 3.3.2), no inherent degradation of the oxygen flux was found for the Nb-substituted solid solutions, which renders these compositions, especially at low Nb-concentrations, as attractive alternatives to BSCF membranes.

Another incentive to partial substitution of niobium for (Co,Fe) in this study has been to increase the surface acidity of BSCF, attempting to improve its CO<sub>2</sub> tolerance. Exposure of BSCF-membranes to CO<sub>2</sub>-containing gas streams is known to induce deterioration of the oxygen fluxes over time due to formation of surface carbonates and concomitant partial decomposition of the perovskite phase [17, 18]. Fig. 3.7 shows that changing from helium to pure CO<sub>2</sub> as purge gas, at 875 °C, results in an immediate cessation of the oxygen flux through a BSCFN10 membrane, and to full recovery of the oxygen flux when the sweep gas is switched back to helium. The latter suggests reformation of the cubic perovskite phase when the membrane is exposed to helium again. A degradation of the oxygen flux is also observed when 10% CO<sub>2</sub>/He is used as sweep gas, albeit that 6-8 h are needed to establish a new steady-state, where the flux is reduced by almost 60% (see Fig. 3.7). Similar performance degradations have been reported for pure BSCF [17, 19] and Ba-Co<sub>0.4</sub>Fe<sub>0.4</sub>Nb<sub>0.2</sub>O<sub>3-δ</sub> [33]. The authors from these studies demonstrated the growth of a carbonate surface layer during exposure to CO<sub>2</sub>, which is limited by the outward diffusion of barium and/or strontium cations, and formation of an adjacent multi-phase decomposed zone.

The above results indicate that other strategies than partial substitution of (Co,Fe) in BSCF by Nb need to be developed to increase its CO<sub>2</sub>-tolerance. An

obvious consideration is to avoid the use of barium in the perovskite phase, and to replace it by its smaller alkaline-earth counterparts. Another strategy is to operate the membrane below the equilibrium partial pressure of  $\text{CO}_2$  for the decarboxylation reaction of  $\text{BaCO}_3$ ,  $\text{BaCO}_3 \rightarrow \text{BaO} + \text{CO}_2$ , suppressing its formation. Simple calculation, using thermodynamic data in [34], yields equilibrium  $\text{CO}_2$  pressures due to decomposition of  $\text{BaCO}_3$  and  $\text{SrCO}_3$  of 87 and 3302 Pa at 900 °C, and 270 and 8854 Pa at 950 °C, respectively (see Fig. 3.8). Unless demanded by the targeted application, however, increasing the membrane operation temperature is not a preferred way to go as this will have a major impact on stability-related issues, such as creep, which is known to be strongly thermally activated ( $> 250 \text{ kJ mol}^{-1}$ ) [35].

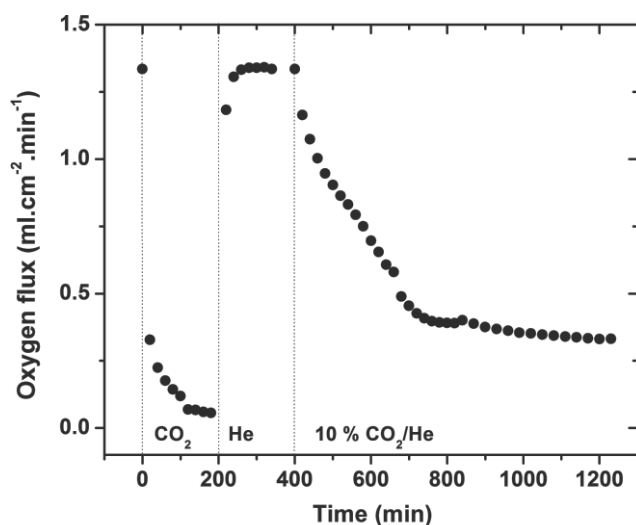


**Figure 3.7** Time dependence of the oxygen permeation flux of a BSCFN10 membrane at 875 °C after switching from pure helium to 10%  $\text{CO}_2/\text{He}$  (at 0 min), in reverse direction (at 200 min), and from pure helium to pure  $\text{CO}_2$  (at 400 min). Membrane thickness: 1 mm, feed gas: air ( $100 \text{ ml min}^{-1}$ ), sweep gas: He, 10%  $\text{CO}_2/\text{He}$  or pure  $\text{CO}_2$  ( $50 \text{ ml min}^{-1}$ ).

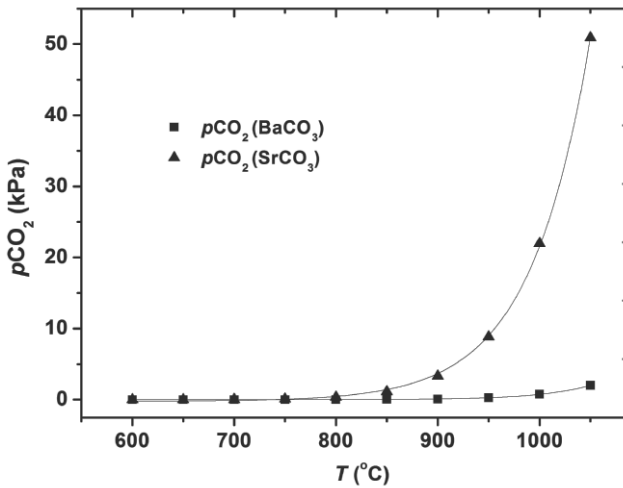


**Figure 3.8** Temperature dependences of the calculated equilibrium  $\text{CO}_2$  pressure over  $\text{BaCO}_3$  and  $\text{SrCO}_3$ .

### 3.4 Conclusions

It is demonstrated that partial substitution of niobium for (Co,Fe) in BSCF suppresses the phase instability as apparent in the parent oxide at intermediate temperatures (below  $\sim 850^\circ\text{C}$ ). As expected, the rate of oxygen permeation decreases with the extent of Nb-substitution. The oxygen permeation flux of 10 mol% Nb-substituted BSCF in the range  $800\text{--}900^\circ\text{C}$  decreases only 10% relative to that observed for pure BSCF, rendering Nb-substituted BSCF as an attractive alternative for use as an oxygen separation membrane. The linear thermal expansion coefficient (TEC) in the range  $500\text{--}1050^\circ\text{C}$  gradually decreases from  $19 \times 10^{-6}^\circ\text{C}^{-1}$  for BSCF to  $16 \times 10^{-6}^\circ\text{C}^{-1}$  for 20 mol% Nb-substituted BSCF. In the low-temperature range  $200\text{--}500^\circ\text{C}$ , the TECs vary between  $9 \times 10^{-6}$  and  $11 \times 10^{-6}^\circ\text{C}^{-1}$ . Nb-substitution, however, leads to undesirable lowering of the electrical conductivity, which may restrict use of the substituted oxides as cathodes in SOFCs. Furthermore, though Nb-substitution

of BSCF stabilizes the cubic perovskite phase, it does not improve its CO<sub>2</sub> tolerance. Switching from helium to a CO<sub>2</sub>-containing purge gas results in a severe reduction or cessation of the oxygen flux, as is observed for parent BSCF. Options are discussed to avoid undesired formation of surface carbonates, blocking the oxygen fluxes.



## References

1. S. McIntosh, J.F. Vente, W.G. Haije, D.H.A. Blank, H.J.M. Bouwmeester, *Chem. Mater.* 18 (2006) 2187.
2. E. Bucher, A. Egger, P. Ried, W. Sitte, P. Holtappe Is, *Solid State Ionics* 179 (2008) 1032.
3. R. Kriegel, R. Kircheisen, J. Topfer, *Solid State Ionics* 181 (2010) 64.
4. Z.P. Shao, G.X. Xiong, J.H. Tong, H. Dong, W.S. Yang, *Sep. Purif. Technol.* 25 (2001) 419.
5. Z.P. Shao, S.M. Haile, *Nature* 431 (2004) 170.
6. Y. Teraoka, H.M. Zhang, S. Furukawa, N. Yamazoe, *Chem. Lett.* (1985) 1743.
7. Z.Q. Deng, W.S. Yang, W. Liu, C.S. Chen, *J. Solid State Chem.* 179 (2006) 362.
8. L.M. Liu, T.H. Lee, L. Qiu, Y.L. Yang, A.J. Jacobson, *Mater. Res. Bull.* 31 (1996) 29.
9. S. McIntosh, J.F. Vente, W.G. Haije, D.H.A. Blank, H.J.M. Bouwmeester, *Solid State Ionics* 177 (2006) 833.
10. S. McIntosh, J.F. Vente, W.G. Haije, D.H.A. Blank, H.J.M. Bouwmeester, *Solid State Ionics* 177 (2006) 1737.
11. S. Švarcová, K. Wiik, J. Tolchard, H.J.M. Bouwmeester, T. Grande, *Solid State Ionics* 178 (2008) 1787.
12. M. Arnold, T.M. Gesing, J. Martynczuk, A. Feldhoff, *Chem. Mater.* 20 (2008) 5851.
13. D.N. Mueller, R.A. De Souza, T.E. Weirich, D. Roehrens, J. Mayer, M. Martin, *Phys. Chem. Chem. Phys.* 12 (2010) 10320.
14. K. Efimov, Q. Xu, A. Feldhoff, *Chem. Mater.* 22 (2010) 5866.
15. Z.P. Shao, G.X. Xiong, H. Dong, W.H. Yang, L.W. Lin, *Sep. Purif. Technol.* 25 (2001) 97.
16. A.C. van Veen, M. Rebeilleau, D. Farrusseng, C. Mirodatos, *Chem. Commun.* (2003) 32.
17. M. Arnold, H.H. Wang, A. Feldhoff, *J. Membr. Sci.* 293 (2007) 44.
18. A.Y. Yan, L. Bin, Y.L. Dong, Z.J. Tian, D.Z. Wang, M.J. Cheng, *Appl. Catal. B* 80 (2008) 24.
19. J. Yi, M. Schroeder, *J. Membr. Sci.* 378 (2011) 163.
20. J. Rodríguez-Carvajal, *Commission on Powder Diffraction* 26 (2001) 12.
21. J.E. ten Elshof, H.J.M. Bouwmeester, H. Verweij, *Solid State Ionics* 81 (1995) 97.
22. R.D. Shannon, *Acta Crystallogr. A* 32 (1976) 751.
23. P.Y. Zeng, Z.H. Chen, W. Zhou, H.X. Gu, Z.P. Shao, S.M. Liu, *J. Membr. Sci.* 291 (2007) 148.
24. B.W. Liu, Y. Zhang, L.D. Tang, *Int. J. Hydrogen. Energ* 34 (2009) 435.
25. V.M. Goldschmidt, *Naturwissenschaften* 14 (1926) 477.

26. S. Yakovlev, C.-Y. Yoo, S. Fang, H.J.M. Bouwmeester, *Appl. Phys. Lett.* 96 (2010) 254101.
27. K. Zhang, R. Ran, L. Ge, Z. Shao, W. Jin, N. Xu, *J. Membr. Sci.* 323 (2008) 436.
28. S.Y. Li, Z. Lu, B. Wei, X.Q. Huang, J.P. Miao, G. Cao, R.B. Zhu, W.H. Su, *J. Alloys Compd.* 426 (2006) 408.
29. B. Wei, Z. Lu, X.Q. Huang, J.P. Miao, X.Q. Sha, X.S. Xin, W.H. Su, *J. Eur. Ceram. Soc.* 26 (2006) 2827.
30. H. Lu, Y. Cong, W.S. Yang, *Solid State Ionics* 177 (2006) 595.
31. J.-I. Jung, S.T. Misture, D.D. Edwards, *Solid State Ionics* 181 (2010) 1287.
32. J.-I. Jung, S. Misture, D. Edwards, *J. Electroceram.* 24 (2010) 261.
33. J. Yi, M. Schroeder, T. Weirich, J. Mayer, *Chem. Mater.* 22 (2010) 6246.
34. J.G. Speight, *Lange's Handbook of Chemistry*, 16th ed. McGraw-Hill, 2005.
35. J.X. Yi, H.L. Lein, T. Grande, S. Yakovlev, H.J.M. Bouwmeester, *Solid State Ionics* 180 (2009) 1564.



---

## Chapter 4

### *In-situ* neutron diffraction study of zirconium- and niobium-substituted $\text{Ba}_{0.5}\text{Sr}_{0.5}\text{Co}_{0.8}\text{Fe}_{0.2}\text{O}_{3-\delta}$

#### Abstract

Neutron powder diffraction measurements have been performed on the perovskite-type oxide  $\text{Ba}_{0.5}\text{Sr}_{0.5}\text{Co}_{0.8}\text{Fe}_{0.2}\text{O}_{3-\delta}$ , substituted with either Zr or Nb for (Co,Fe). Rietveld analyses of the diffraction patterns recorded in the temperature range 27-900 °C shows that the phase obtained upon substitution of 3 mol% Zr (BSCFZ3) like parent BSCF is cubic with space group  $Pm\bar{3}m$ , while substitution of 10 mol% Nb (BSCFN10) yields an orthorhombic structure, with space group  $Pnma$ . The latter originates from the tilting of  $\text{BO}_6$  octahedra in the perovskite structure. The thermal expansion coefficients in the range 600-900 °C are  $25.3 (1) \times 10^{-6} \text{ }^\circ\text{C}^{-1}$  and  $15.9 (1) \times 10^{-6} \text{ }^\circ\text{C}^{-1}$  for BSCFZ3 and BSCFN10, respectively.

## 4.1 Introduction

$\text{Ba}_{0.5}\text{Sr}_{0.5}\text{Co}_{0.8}\text{Fe}_{0.2}\text{O}_{3-\delta}$  (BSCF) has potential for use as oxygen transport membrane [1], cathode for solid oxide fuel cells [2], and as a catalyst for lithium air batteries [3]. BSCF exhibits fast oxygen ionic conductivity due to its high oxygen deficiency ( $\delta = 0.66$  at  $600\text{ }^\circ\text{C}$  and  $p\text{O}_2 = 1\text{ atm}$ , and  $\delta = 0.81$  at  $900\text{ }^\circ\text{C}$  and  $p\text{O}_2 = 10^{-3}\text{ atm}$ ) [4]. Superior surface exchange ( $k^*$ ) and tracer diffusion ( $D^*$ ) coefficients have been confirmed by  $^{18}\text{O}$ - $^{16}\text{O}$  isotope exchange and electrochemical impedance spectroscopy measurements [5-7]. However, BSCF undergoes a structural phase transition to hexagonal polymorphs during long-term operation below  $825\text{ }^\circ\text{C}$  [8-10]. Recently, we have demonstrated that a small co-doping of zirconium [11] or niobium [12] on the B-site can suppress the phase transition. In response to these findings, we have examined the crystal structure of 3 mol% zirconium-substituted BSCF and 10 mol% niobium-substituted BSCF using *in-situ* neutron diffraction data between  $27$  and  $900\text{ }^\circ\text{C}$ .

## 4.2 Experimental

$\text{Ba}_{0.5}\text{Sr}_{0.5}\text{Co}_{0.776}\text{Fe}_{0.194}\text{Zr}_{0.03}\text{O}_{3-\delta}$  (BSCFZ3) powder was prepared by spray pyrolysis, and subsequently calcined, at  $950\text{ }^\circ\text{C}$ , for 10 h in air.  $\text{Ba}_{0.5}\text{Sr}_{0.5}\text{Co}_{0.72}\text{Fe}_{0.18}\text{Nb}_{0.1}\text{O}_{3-\delta}$  (BSCFN10) was prepared by a solid state reaction as described previously [12]. Prior to the neutron diffraction measurements, both compositions were examined by conventional X-ray powder diffraction (Bruker D2 PHASER) to confirm their phase purity.

Neutron diffraction measurements were carried out at the high-resolution HRPT diffractometer at SINQ neutron spallation source (Paul Scherrer Institute, Switzerland) [13]. The high-intensity mode of HRPT was used with neutron wavelength  $\lambda = 1.49\text{ \AA}$ . All samples were investigated, at  $27\text{ }^\circ\text{C}$ , using a vanadium container. For *in-situ* high temperature measurements, about 5 g of

the powder was loaded in a steel sample holder. The holder was placed in a vacuum furnace with the sample exposed to the incident neutron beam. Measurements were conducted under flowing air. Prior to the high temperature measurements, diffraction patterns were collected at 27 °C. Subsequently, the sample was heated to 900 °C, and the temperature decreased stepwise from 900 °C to 600 °C with 100 °C intervals, using heating/cooling rates of 10 °C min<sup>-1</sup>. The sample was equilibrated at each temperature. Equilibration was considered to be complete when no shift occurred in the position of the diffraction peaks. Each pattern was recorded three times. The total measurement time, including equilibration, lasted about three hours at each temperature. Diffraction patterns were collected in the range of  $10^\circ \leq 2\theta \leq 150^\circ$  with a step size of 0.05° (2  $\theta$  range).

The neutron diffraction data were analyzed by Rietveld refinements using the FullProf program [14]. The shape of the diffraction peaks was generated by a Thompson-Cox-Hastings pseudo-Voigt function. Manual background correction was used in all refinements. The occupancy of the cation sites was fixed according to the stoichiometric composition, whereas the isotropic atomic displacement parameters of cations on the same site were constrained to be the same. The oxygen occupancy was refined to evaluate the oxygen nonstoichiometry. In the final run, the following parameters were refined: zero shift, peak width/shape/asymmetry, scale factor, and crystal structure parameters (lattice parameters, atomic positions, isotropic atomic displacement parameters, and occupancy factors for oxygen).

### **4.3 Results and discussion**

Fig. 4.1 shows the observed, calculated, and difference profiles from refinement of the neutron diffraction data of BSCFZ3 collected at 27 °C. Fig. 4.2 shows the corresponding profiles for BSCFN10, which were fitted both in

space groups  $Pm\bar{3}m$  and  $Pnma$ . A G-type antiferromagnetic structure of BSCF was reported by McIntosh *et al.* [4]. In the present study, the magnetic peaks were excluded in the refinement of the diffraction patterns at 27 °C. Fig. 4.3 shows the evolution of the neutron diffraction patterns for the two materials in the temperature range 27-900 °C. Representative structural parameters, residual indices and bond lengths obtained from refinements of the diffraction patterns obtained for both materials at 27 °C and 900 °C are listed in Tables 4.1-4.3.

Pure BSCF has been described as a cubic perovskite structure with space group  $Pm\bar{3}m$  [4]. Likewise the neutron diffraction pattern for BSCFZ3 was well fitted with space group  $Pm\bar{3}m$ . As expected in view of the low Zr-substitution, the refined lattice parameter of 3.9898 (1) Å at 27 °C and 4.0542 (1) Å at 900 °C are in close agreement with published values for pure BSCF [4]. This is further exemplified below where we discuss the thermal evolution of the lattice parameter, cell volume and oxygen nonstoichiometry for the two materials under investigation.

BSCFN10 is found to exhibit orthorhombic symmetry. As illustrated in Fig. 4.2 (b) excellent fits are obtained in space group  $Pnma$ . Poor results were obtained when the corresponding patterns were fitted on the basis of a simple cubic structure in space group  $Pm\bar{3}m$ , as illustrated for the pattern collected at 27 °C in Fig. 4.2 (a).  $ABO_3$  perovskite oxides often possess pseudo-cubic symmetry which originates from tilting of the  $BO_6$  octahedra. For space group  $Pnma$ , the tilting behavior is described as  $a^-b^+a^-$  according to Glazer's notation [15]. Barium and strontium are statistically distributed over the 4c sites ( $x$ , 0.25,  $z$ ) of space group  $Pnma$ . Cobalt, iron, and niobium are statistically distributed over the 4a sites (0.5, 0, 0). Due to tilting of the  $BO_6$  octahedra, there are two types of oxygen atoms: O1 is at the 4c site ( $x$ , 0.25,  $z$ ) and O2 at the

general  $8d$  site ( $x, y, z$ ). As a consequence, the oxygen coordination of A-site cations barium and strontium is significantly distorted with average A-O bond lengths in the range of 2.8-3 Å, as shown in Table 4.3.

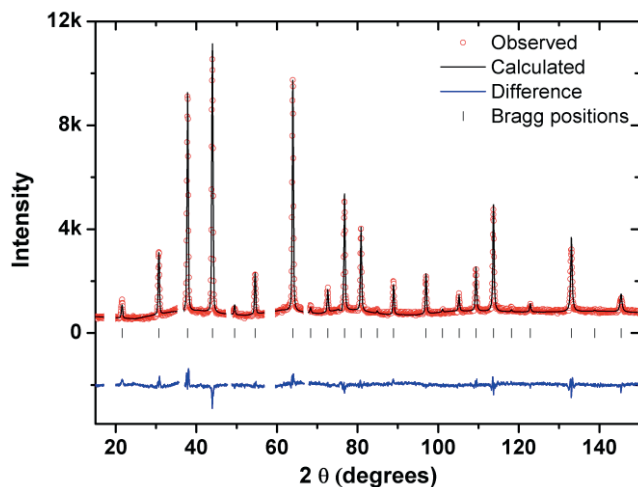


**Figure 4.1** Neutron powder diffraction pattern for BSCFZ3 at 27 °C. The observed data are presented by circles, and the solid lines is the result from Rietveld refinements in space group  $Pm\bar{3}m$ . Also shown is the difference profile (lower line). Tick markers indicate the Bragg positions.



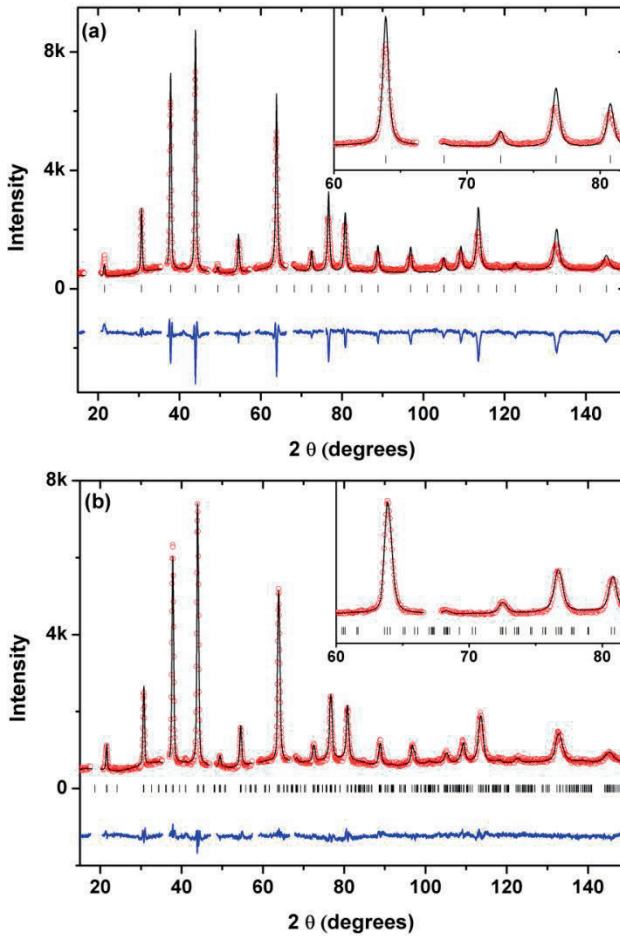


**Figure 4.2** Neutron powder diffraction pattern for BSCFN10 at 27 °C. The observed data are presented by circles, and the solid line is the result from Rietveld refinements in space group (a)  $Pm\bar{3}m$  and (b)  $Pnma$ . Also shown are the difference profiles (lower lines). Tick markers indicate the Bragg positions. The inserts highlight portions of the diffraction patterns to better show the quality of the fit.

**Table 4.1** Structural parameters from Rietveld refinements of neutron powder diffraction data, collected at 27 °C, for (a) BSCFZ3 and (b) BSCFN10.

(a)  $\text{Ba}_{0.5}\text{Sr}_{0.5}\text{Co}_{0.776}\text{Fe}_{0.194}\text{Zr}_{0.03}\text{O}_{3-\delta}$  (BSCFZ3) - Space group :  $Pm\bar{3}m$ ,  $Z = 1$   
 $a = 3.9898$  (1) Å,  $R_p = 4.72$  %,  $R_{wp} = 5.99$  %,  $R_{exp} = 3.17$  %,  $\chi^2 = 3.58$

	site	occupancy	$x$	$y$	$z$	$U_{iso}$ (100*Å <sup>2</sup> )
(Ba,Sr)	1b	1	0.5	0.5	0.5	1.99 (3)
(Co,Fe,Zr)	1a	1	0	0	0	1.69 (4)
O	3c	0.804 (4)	0.5	0	0	2.55 (3)

(b)  $\text{Ba}_{0.5}\text{Sr}_{0.5}\text{Co}_{0.72}\text{Fe}_{0.18}\text{Nb}_{0.1}\text{O}_{3-\delta}$  (BSCFN10) - Space group :  $Pnma$ ,  $Z = 4$   
 $a = 5.6653$  (3) Å,  $b = 7.9628$  (3) Å,  $c = 5.6447$  (3) Å  
 $R_p = 4.75$  %,  $R_{wp} = 6.08$  %,  $R_{exp} = 3.40$  %,  $\chi^2 = 3.19$

	site	occupancy	$x$	$y$	$z$	$U_{iso}$ (100*Å <sup>2</sup> )
(Ba,Sr)	4c	1	-0.009 (2)	0.25	0.000 (2)	1.66 (5)
(Co,Fe,Nb)	4a	1	0.5	0	0	1.28 (5)
O1	4c	0.638 (1)	0.009 (2)	0.25	0.509 (2)	1.23 (9)
O2	8d	0.916 (2)	0.759 (5)	-0.004 (3)	0.241 (3)	3.6 (1)

**Table 4.2** Structural parameters from Rietveld refinements of neutron powder diffraction data, collected at 900 °C, for (a) BSCFZ3 and (b) BSCFN10.

(a)  $\text{Ba}_{0.5}\text{Sr}_{0.5}\text{Co}_{0.776}\text{Fe}_{0.194}\text{Zr}_{0.03}\text{O}_{3-\delta}$  (BSCFZ3) - Space group :  $Pm\bar{3}m$ ,  $Z = 1$   
 $a = 4.0542$  (1) Å,  $R_p = 3.89$  %,  $R_{wp} = 4.95$  %,  $R_{exp} = 2.50$  %,  $\chi^2 = 3.94$

	site	occupancy	$x$	$y$	$z$	$U_{iso}$ ( $100 \cdot \text{Å}^2$ )
(Ba,Sr)	$1b$	1	0.5	0.5	0.5	3.42 (11)
(Co,Fe,Zr)	$1a$	1	0	0	0	3.84 (14)
O	$3c$	0.765 (7)	0.5	0	0	5.33 (10)

(b)  $\text{Ba}_{0.5}\text{Sr}_{0.5}\text{Co}_{0.72}\text{Fe}_{0.18}\text{Nb}_{0.1}\text{O}_{3-\delta}$  (BSCFN10) - Space group :  $Pnma$ ,  $Z = 4$   
 $a = 5.7477$  (1) Å,  $b = 8.1293$  (1) Å,  $c = 5.7062$  (1) Å  
 $R_p = 3.58$  %,  $R_{wp} = 4.60$  %,  $R_{exp} = 2.57$  %,  $\chi^2 = 3.19$

	site	occupancy	$x$	$y$	$z$	$U_{iso}$ ( $100 \cdot \text{Å}^2$ )
(Ba,Sr)	$4c$	1	0.019 (1)	0.25	0.021 (1)	2.08 (12)
(Co,Fe,Nb)	$4a$	1	0.5	0	0	4.40 (19)
O1	$4c$	0.475 (15)	-0.003 (7)	0.25	0.506 (3)	1.8 (4)
O2	$8d$	0.940 (14)	0.742 (6)	-0.004 (4)	0.265 (4)	7.5 (3)

**Table 4.3** Representative atomic distances and angles for BSCFZ3 and BSCFN10 at 27 °C and 900 °C.

Distance/angle	27 °C	900 °C
BSCFZ3		
(Ba,Sr)-O × 12 (Å)	2.8212 (1)	2.8668 (1)
(Co,Fe,Zr)-O × 6 (Å)	1.9949 (1)	2.0271 (1)
(Co,Fe,Zr)-O-(Co,Fe,Zr) (°)	180	180
BSCFN10		
(Ba,Sr)-O1 × 1 (Å)	2.773 (16)	2.771 (19)
(Ba,Sr)-O1 × 1 (Å)	2.875 (16)	2.780 (40)
(Ba,Sr)-O1 × 1 (Å)	2.833 (16)	2.942 (19)
(Ba,Sr)-O1 × 1 (Å)	2.833 (16)	2.970 (40)
(Ba,Sr)-O2 × 2 (Å)	2.770 (20)	2.670 (30)
(Ba,Sr)-O2 × 2 (Å)	2.770 (20)	2.920 (30)
(Ba,Sr)-O2 × 2 (Å)	2.870 (20)	2.940 (30)
(Ba,Sr)-O2 × 2 (Å)	2.880 (30)	2.960 (30)
(Co,Fe,Nb)-O1 × 2 (Å)	1.9920 (4)	2.0327 (4)
(Co,Fe,Nb)-O2 × 2 (Å)	2.000 (20)	2.000 (30)
(Co,Fe,Nb)-O2 × 2 (Å)	2.000 (20)	2.050 (30)
(Co,Fe,Nb)-O1-(Co,Fe,Nb) (°)	175.86 (2)	177.84 (2)
(Co,Fe,Nb)-O2-(Co,Fe,Nb) (°)	175.5 (9)	174.4 (12)

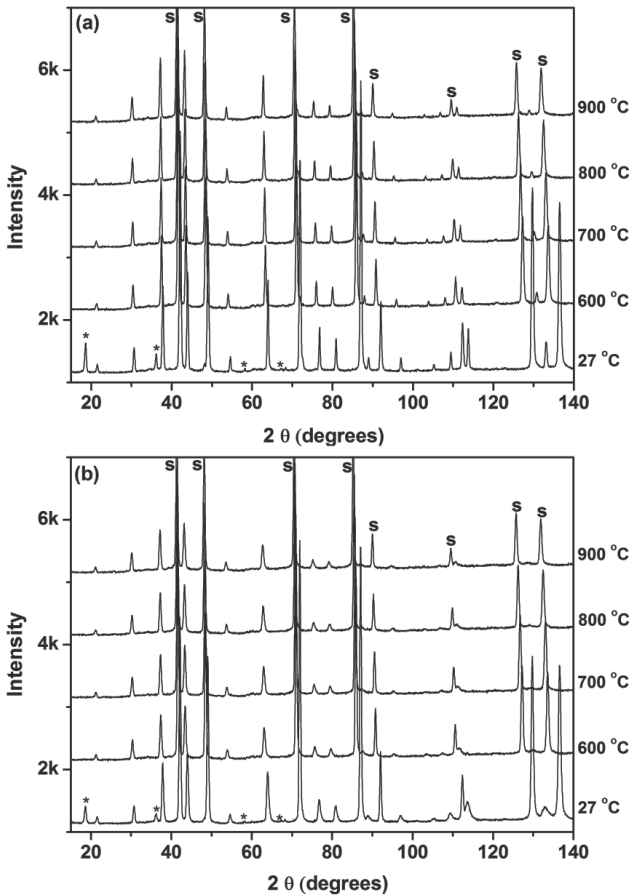


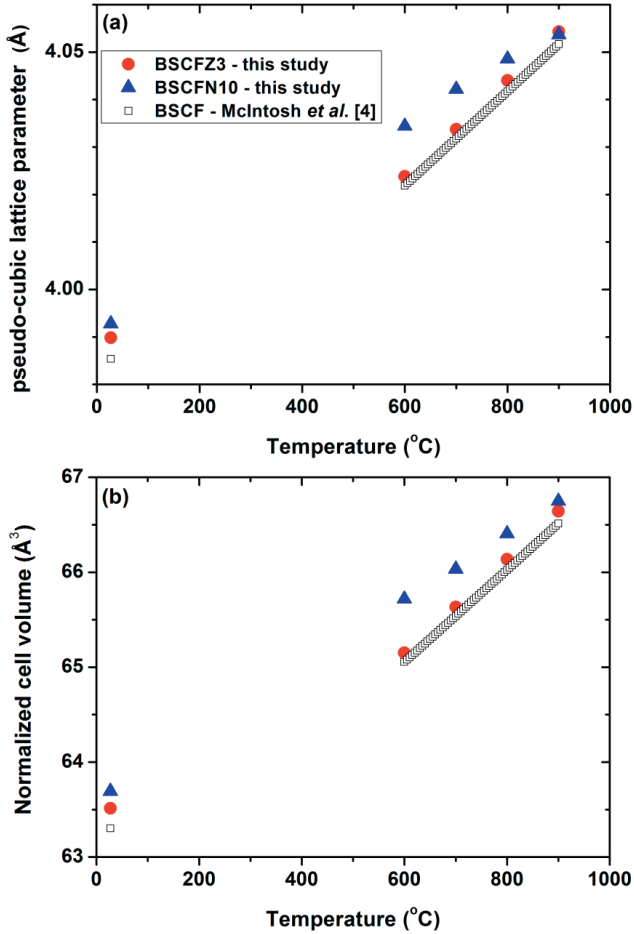
**Figure 4.3** Neutron diffraction patterns of (a) BSCFZ3 and (b) BSCFN10 recorded in the temperature range 27-900 °C. Steel sample holder peaks are marked with character *s*. Magnetic peaks are marked with an asterisk.

The temperature dependences of the cubic or pseudo-cubic lattice parameter and cell volume from Rietveld analysis of the diffraction patterns for the two materials under investigation are shown in Fig. 4.4. Also included are data for pure BSCF reported by McIntosh *et al.* [4]. At elevated temperature, the loss of oxygen and associated reduction of the number of B-site cations cobalt

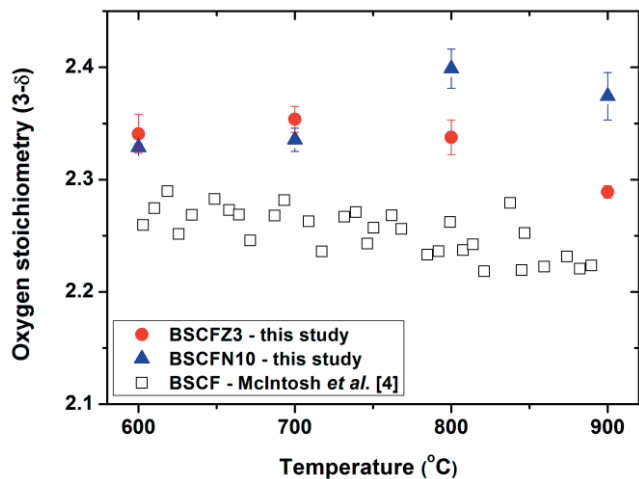
and iron, referred to as chemical expansion [16], contributes to the total thermal expansion. The calculated thermal expansion coefficients for BSCFZ3 and BSCFN10 are  $25.3 (1) \times 10^{-6} \text{ }^\circ\text{C}^{-1}$  and  $15.9 (1) \times 10^{-6} \text{ }^\circ\text{C}^{-1}$ , respectively, using  $600 \text{ }^\circ\text{C}$  as a reference temperature. These may be compared with the value of  $24 (1) \times 10^{-6} \text{ }^\circ\text{C}^{-1}$ , evaluated previously for BSCF from data of neutron powder diffraction [4]. For BSCFZ3, the thermal expansion coefficient compares favorably with that of BSCF, as expected. Relative to BSCF, the thermal expansion coefficient of BSCFN10 has decreased by  $\sim 30\%$ , which may, at least partly, be accounted for by the non-redox behavior of the niobium dopant. Finally, it is noted that the thermal expansion coefficient evaluated for BSCFN10 is in excellent agreement with that measured previously by conventional dilatometry [12].

Fig. 4.5 shows the temperature dependence of the oxygen stoichiometry from Rietveld analysis of the neutron diffraction patterns of BSCFZ3 and BSCFN10 in the range  $600\text{-}900 \text{ }^\circ\text{C}$ , which data were calculated from the refined oxygen site occupancies. Corresponding data for BSCF published by McIntosh *et al.* [4] is included for comparison. The slightly higher oxygen contents observed for both substituted phases, relative to parent BSCF, is more or less expected in view of the non-redox behavior and the high valences of the dopant cations  $\text{Zr}^{4+}$  and  $\text{Nb}^{5+}$ . The corresponding temperature dependences are not very pronounced, although, admittedly, the behavior is somewhat difficult to judge for both phases due to the limited number of scattered data points. The total variation of the oxygen stoichiometry of BSCFZ3 in the investigated temperature range is only  $\Delta(3-\delta) \approx 0.05$ . For BSCFN10 this change is slightly larger, but the trend (*i.e.*, increase of oxygen stoichiometry with increasing temperature) is somewhat unexpected. As discussed by Satto *et al.* [17], it cannot be excluded that there is a certain correlation between the site occupancy and the atomic displacement parameter. Additional measurements are re-

quired to elucidate the probably subtle variations of the oxygen stoichiometry of BSCFZ3 and BSCFN10 with temperature.



**Figure 4.4** Temperature dependence of the (a) cubic or pseudo-cubic lattice parameter, and (b) normalized cell volume ( $Z=1$ ) for BSCFZ3 and BSCFN10 obtained from the neutron diffraction measurements. Included for comparison are data for BSCF from literature.



**Figure 4.5** Temperature dependence of the oxygen stoichiometry of BSCFZ3 and BSCFN10 obtained from the neutron diffraction measurements. Included for comparison are data for BSCF from literature.

#### 4.4 Conclusions

The crystal structures of BSCFZ3 and BSCFN10 have been investigated by neutron powder diffraction from 300 to 1173 K. Rietveld analysis of the diffraction patterns shows that BSCFZ3 adopts a cubic perovskite structure with space group  $Pm\bar{3}m$ , like parent BSCF, while BSCFN10 adopts an orthorhombic perovskite structure with space group  $Pnma$ . The thermal expansion coefficients in the range of 600 to 900 °C are  $25.3 (1) \times 10^{-6} \text{ }^\circ\text{C}^{-1}$  and  $15.9 (1) \times 10^{-6} \text{ }^\circ\text{C}^{-1}$ , respectively.

#### Acknowledgement

Dr. Denis Sheptyakov (Paul Scherrer Institute, Switzerland) is gratefully acknowledged for experimental support.



## References

1. J.F. Vente, S. McIntosh, W.G. Haije, H.J.M. Bouwmeester, *J. Solid State Electrochem.* 10 (2006) 581.
2. Z.P. Shao, S.M. Haile, *Nature* 431 (2004) 170.
3. J. Suntivich, K.J. May, H.A. Gasteiger, J.B. Goodenough, S.H. Yang, *Science* 334 (2011) 1383.
4. S. McIntosh, J.F. Vente, W.G. Haije, D.H.A. Blank, H.J.M. Bouwmeester, *Chem. Mater.* 18 (2006) 2187.
5. H.J.M. Bouwmeester, C. Song, J. Zhu, J. Yi, M. van Sint Annaland, B.A. Boukamp, *Phys. Chem. Chem. Phys.* 11 (2009) 9640.
6. L. Wang, R. Merkle, J. Maier, T. Acartuerk, U. Starke, *Appl. Phys. Lett.* 94 (2009) 071908.
7. L. Wang, R. Merkle, J. Maier, *J. Electrochem. Soc.* 157 (2010) B1802.
8. S. Švarcová, K. Wiik, J. Tolchard, H.J.M. Bouwmeester, T. Grande, *Solid State Ionics* 178 (2008) 1787.
9. M. Arnold, T.M. Gesing, J. Martynczuk, A. Feldhoff, *Chem. Mater.* 20 (2008) 5851.
10. D.N. Mueller, R.A. De Souza, T.E. Weirich, D. Roehrens, J. Mayer, M. Martin, *Phys. Chem. Chem. Phys.* 12 (2010) 10320.
11. S. Yakovlev, C.-Y. Yoo, S. Fang, H.J.M. Bouwmeester, *Appl. Phys. Lett.* 96 (2010) 254101.
12. S.M. Fang, C.-Y. Yoo, H.J.M. Bouwmeester, *Solid State Ionics* 195 (2011) 1.
13. P. Fischer, G. Frey, M. Koch, M. Konnecke, V. Pomjakushin, J. Schefer, R. Thut, N. Schlumpf, R. Burge, U. Greuter, S. Bondt, E. Berruyer, *Physica. B* 276 (2000) 146.
14. J. Rodríguez-Carvajal, *Commission on Powder Diffraction* 26 (2001) 12.
15. A.M. Glazer, *Acta Crystallogr. B* 28 (1972) 3384.
16. S.B. Adler, *J. Am. Ceram. Soc.* 84 (2001) 2117.
17. C. Satto, J. Jansen, C. LExcellent, D. Schryvers, *Solid State Commun.* 116 (2000) 273.

---

## Chapter 5

# Oxygen surface exchange kinetics of erbia-stabilized bismuth oxide

### Abstract

The surface oxygen exchange kinetics of bismuth oxide stabilized with 25 mol% erbia (BE25) has been studied in the temperature and oxygen partial pressure ( $pO_2$ ) ranges 500-750 °C and 0.1-0.95 atm, respectively, using pulse-response  $^{18}O$ - $^{16}O$  isotope exchange measurements. The results indicate that BE25 exhibits a comparatively high exchange rate, which is rate determined by the dissociative adsorption of oxygen. Defect chemical considerations and the observed  $pO_2^{1/2}$  dependence of the rate of dissociative oxygen adsorption suggest electron transfer to intermediate superoxide ions as the rate determining step in surface oxygen exchange on BE25.

## 5.1 Introduction

Stabilized phases of  $\delta\text{-Bi}_2\text{O}_3$  exhibit high oxide ion conductivity, which is related to a high polarizability of the bismuth ion and a high concentration of oxygen vacancies. In the parent cubic fluorite structure of  $\delta\text{-Bi}_2\text{O}_3$ , 25% of the sites in the oxygen sublattice are vacant. Pure  $\text{Bi}_2\text{O}_3$ , however, transforms from the  $\delta$ -phase to the monoclinic  $\alpha$ -phase upon cooling below  $\sim 730^\circ\text{C}$  [1], showing a discontinuity in the ionic conductivity. The high temperature  $\delta\text{-Bi}_2\text{O}_3$  phase can be stabilized to room temperature by the addition of rare earth oxides [2-6]. Erbium-stabilized bismuth oxide,  $(\text{Bi}_2\text{O}_3)_{0.75}\text{-(Er}_2\text{O}_3)_{0.25}$ , referred to as BE25, shows an ionic conductivity more than two orders of magnitude higher than that of conventional yttria-stabilized zirconia (YSZ), and has been investigated for its possible use as electrolyte for the low-temperature solid oxide fuel cell [5, 6].

Stabilization of  $\delta\text{-Bi}_2\text{O}_3$  with isovalent  $\text{Er}_2\text{O}_3$  preserves its high vacancy concentration albeit that, in general, a higher  $\text{Er}_2\text{O}_3$  concentration results in a lower conductivity. At low  $\text{Er}_2\text{O}_3$  concentrations and when operating at temperatures in the range  $600\text{-}700^\circ\text{C}$ , the ionic conductivity is found to slowly decay with time due to transformation of the cubic phase into a rhombohedral phase. Kruidhof *et al.* [7] claimed that, when operating at  $700^\circ\text{C}$ , a dopant concentration of at least 27.5%  $\text{Er}_2\text{O}_3$  is necessary to prevent phase separation. Jiang *et al.* [8] showed that even at a concentration of 40%  $\text{Er}_2\text{O}_3$  the conductivity of phase-stabilized  $\delta\text{-Bi}_2\text{O}_3$  is subject to aging due to gradual ordering of the anion sublattice when operating below  $600^\circ\text{C}$ . In addition to phase and structural instability, the potential application of bismuth-containing electrolytes in solid oxide fuel cells (SOFCs) is regarded to be limited. The poor redox stability of the bismuth ion easily leads to decomposition (to metallic bismuth) of the bismuth-containing electrolyte under the low oxygen partial pressures at the anode (fuel) side.

Compared with YSZ [9] and gadolinia-doped ceria [10], BE25 shows a remarkably high oxygen surface exchange rate. Current-voltage and impedance measurements of the properties of porous sputtered platinum and gold electrodes on BE25 show that the type of electrode material has little effect on the exchange current density, suggesting that for BE25 the entire electrolyte surface is active in the oxygen transfer reaction [11]. Reasonable agreement is found between the exchange current density from current-voltage measurements and the corresponding value calculated from data of  $^{18}\text{O}$ - $^{16}\text{O}$  isotopic exchange measurements. The very high oxide ion diffusivity in BE25 relative to the rate of surface exchange is found to create rather flat diffusion profiles in tracer diffusion experiments. For BE25, a critical thickness of 1.7 cm at 500 °C and 1 atm was deduced by Steele *et al.* [12] and of 10.3 cm at 650 °C at 0.2 atm by Capoen *et al.* [13] from data of  $^{18}\text{O}$ - $^{16}\text{O}$  isotopic exchange depth-profiling (IEDP) using secondary ion mass spectrometry (SIMS) analysis. The critical thickness,  $L_c$ , reflects the length scale below which the surface exchange is rate limiting, and in tracer diffusion experiments is given by  $L_c = D^*/k_s$ , where  $D^*$  is the tracer-diffusion coefficient and  $k_s$  the surface exchange coefficient [14]. The critical thickness at which oxygen diffusion and surface exchange determines equally the rate of oxygen permeation through BE25 was estimated by Bouwmeester *et al.* [15] to be 0.16 mm at 650 °C and 0.09 mm at 910 °C. Note that the critical thickness deduced from oxygen permeation data is two to three orders magnitude lower than that from the tracer diffusion experiments. While in tracer experiments,  $D^*$  governs the diffusion behavior, it is the ambipolar conductivity which controls the rate of oxygen permeation. The ambipolar conductivity in the solid electrolyte BE25 in usual ranges of oxygen partial pressure and temperature is determined by the partial  $p$ -type electronic conductivity, following a  $p\text{O}_2^{1/4}$  power law dependence.

In this study, the surface exchange kinetics of BE25 is re-investigated using the pulse-response  $^{18}\text{O}$ - $^{16}\text{O}$  isotope exchange (PIE) technique. The method recently developed in our laboratory is based upon isotope analysis of an  $^{18}\text{O}$ -enriched gas phase pulse after passage of a continuous-flow packed-bed microreactor loaded with the oxide powder [16]. The measurements are carried out under isothermal and iso- $p\text{O}_2$  conditions. Since the method relies on gas phase analysis of the fractions of oxygen isotopomers with masses 36, 34, and 32 ( $^{18}\text{O}_2$ ,  $^{16}\text{O}^{18}\text{O}$ , and  $^{16}\text{O}_2$ , respectively) also mechanistic information on the exchange reaction can be extracted from experiment contrary to, for example, data obtained by means of the IEDP-SIMS method.

## 5.2 Experimental

BE25 powder prepared by a conventional solid state reaction was provided by the Fraunhofer-Institut für Keramische Technologien und Systeme, IKTS (Institutsteil Hermsdorf). The as-received powder was uniaxially pressed at 30 MPa into a disk, followed by cold isostatic pressing at 400 MPa. The disk was sintered at 850 °C for 10 h in air, and crushed into a coarse powder. The fraction passing a 125  $\mu\text{m}$  stainless steel sieve was pre-annealed at 800 °C for 10 h in air, and sieved again to remove formed agglomerates. Prior to pulse-response isotope exchange measurements, the powders were characterized by X-ray diffraction (PANanalytical PW1830), BET surface area (Micromeritics ASAP 2020 M), and particle size (Malvern Mastersizer 2000) measurements.

The pulse-response isotope exchange measurements were performed in the temperature and  $p\text{O}_2$  ranges 500-750 °C and 0.1-0.95 atm, respectively, using a continuous flow packed-bed micro-reactor. During the measurement, approximately 0.08 g of BE25 powder was loaded between two quartz wool plugs in the center of a quartz tubular microreactor with inner diameter 2 mm.

The length of the packed-bed was typically 13 mm. A  $^{16}\text{O}_2$  with Ar was used as carrier gas fed through the reactor with a total flow rate  $50 \text{ ml min}^{-1}$  (NTP). The response to  $^{18}\text{O}_2/\text{N}_2$  pulse with the same  $p\text{O}_2$  as the carrier gas, passing through the reactor was analyzed by on-line mass spectrometry (Omni Star TM GSD 301 Pfeiffer-Vacuum) at the exit of the reactor as illustrated in Fig. 5.1.

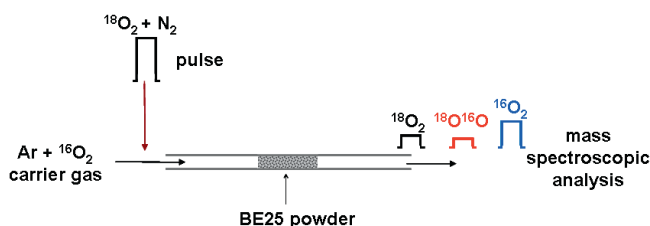


**Figure 5.1** Schematic representation of the pulse-response isotope exchange technique.

A six-port valve with  $500 \mu\text{l}$  sample loop was used for injection of the  $^{18}\text{O}_2/\text{N}_2$  pulse into the  $^{16}\text{O}_2/\text{Ar}$  carrier gas flow stream. Oxygen isotope gas was purchased from Cambridge Isotope Laboratory ( $> 97 \text{ atom}\% \text{ }^{18}\text{O}_2$ ). Nitrogen used as diluent for the  $^{18}\text{O}_2$  gas was also used for internal calibration of the mass spectrometer. The mean residence time of the reactor varied between 10 and 35 ms, being a function of flow rate and temperature. Prior to measurements, the BE25 powder packed-bed was pre-treated at  $800 \text{ }^\circ\text{C}$  for 0.5 h under flowing synthetic air in order to remove possibly adsorbed water and  $\text{CO}_2$ , and subsequently cooled to room temperature at a rate of  $5 \text{ }^\circ\text{C min}^{-1}$ . The pulse isotopic exchange measurements were conducted in the  $p\text{O}_2$  range 0.1-0.95 atm from room temperature onwards up to  $750 \text{ }^\circ\text{C}$ . The reactor was equilibrated 0.5 h at fixed temperature and  $p\text{O}_2$  before and after data collection. Blank experiments revealed no exchange activity of the quartz microreactor.

The packed-bed microreactor was designed to approximate ideal plug flow behavior [14]. The isotopic exchange measurements were performed under conditions of negligible uptake of  $^{18}\text{O}$  by the BE25 powder relative to the number of  $^{16}\text{O}$  oxygen present in the oxide. The overall surface exchange rate,  $\mathfrak{R}_0$  ( $\text{mol O m}^{-2} \text{s}^{-1}$ ), was calculated from

$$\mathfrak{R}_0 = \frac{n}{\tau_r S} \ln \left( \frac{f_{g,i}^{18}}{f_{g,e}^{18}} \right) \quad (5.1)$$

where  $f_{g,i}^{18}$  and  $f_{g,e}^{18}$  are the  $^{18}\text{O}$  isotope fractions in the pulse at the inlet and exit of the reactor, respectively,  $n$  is the total number of oxygen atoms in the free volume of the oxide packed bed,  $S$  the total surface area of the oxide powder, and  $\tau_r$  the average residence time of the labeled gas in the reactor.  $f_g^{18}$  was calculated from the measured pulse integral values of the isotope fractions with mass 36 and 34: ( $f_g^{18} = 0.5f_g^{34} + f_g^{36}$ ) at the exit of the reactor. Average values of three pulse experiments at a given temperature and  $p\text{O}_2$  were taken for evaluation of the surface exchange rate.

### 5.3 Results and discussion

The XRD powder diffractogram (Fig. 5.2 (a)) confirms the presence of a single cubic phase with a lattice parameter of  $a = 5.4736$  (6) Å, which is in agreement with data reported in literature [17]. No evidence for the formation of second phases is found. The particle size distribution of the crushed BE25 ceramics as measured by laser light scattering is shown in Fig. 5.2 (b). The estimated average particle size,  $d_{50} = 0.4 \mu\text{m}$ , is much smaller than the critical thickness (see section 5.1), ensuring that the overall oxygen isotope equilibration is governed by the surface exchange kinetics rather than by bulk diffusion. The associated surface area calculated by the BET method using  $\text{N}_2$  (-196 °C)

gas adsorption data amounts to  $0.2407(5) \text{ m}^2 \text{ g}^{-1}$ . The low value reflects the dense nature of the used BE25 powder, and is due to sintering prior to crushing the ceramic disk into a powder. The sintering step is made to avoid diffusion limitations in narrow pores during oxygen isotope equilibration.

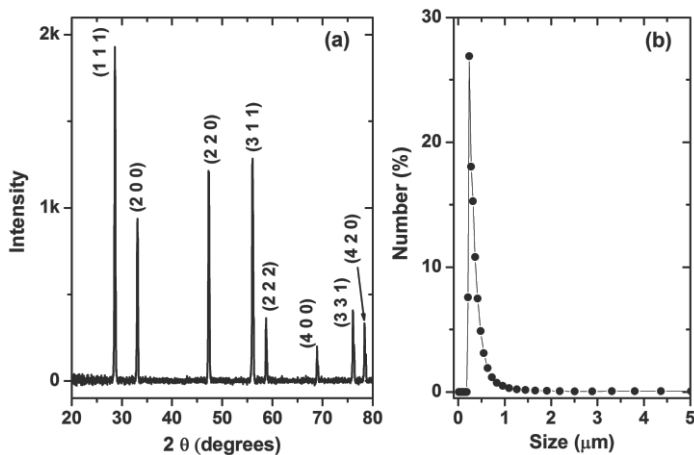
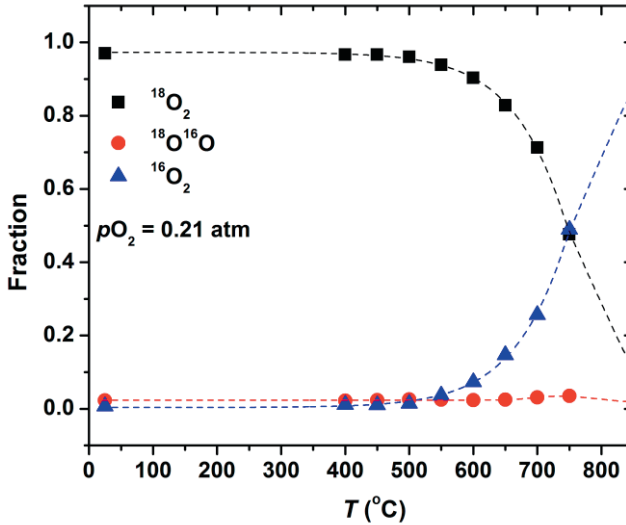


**Figure 5.2** (a) XRD pattern and (b) particle size distribution of BE25 powder used for the PIE experiments.

Fig. 5.3 shows the fractions of oxygen isotopomers in the gas phase volume associated with the pulse at the exit of the reactor as measured at different temperatures. It is seen that under the conditions maintained during the experiments, the exchange reaction starts around  $500 \text{ }^\circ\text{C}$ . Above this temperature, the  $^{18}\text{O}_2$  fraction decreases profoundly with increase of temperature, *i.e.*, more  $^{18}\text{O}$  is taken up by the sample, which is exchanged for  $^{16}\text{O}$  as evidenced by the simultaneous increase of the  $^{16}\text{O}_2$  fraction. The  $^{18}\text{O}^{16}\text{O}$  fraction remains comparatively low at all temperatures. The latter provides evidence that oxygen surface exchange on BE25 is limited by the dissociative adsorption of oxygen, as is further discussed below. The highest temperature of measurement ( $750 \text{ }^\circ\text{C}$ )

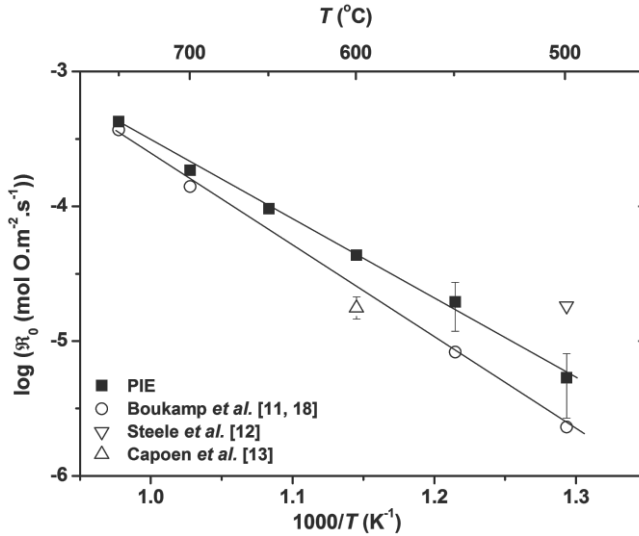


was chosen 50 °C lower than the temperature of the pre-annealing in order to prevent microstructural changes to the powder.



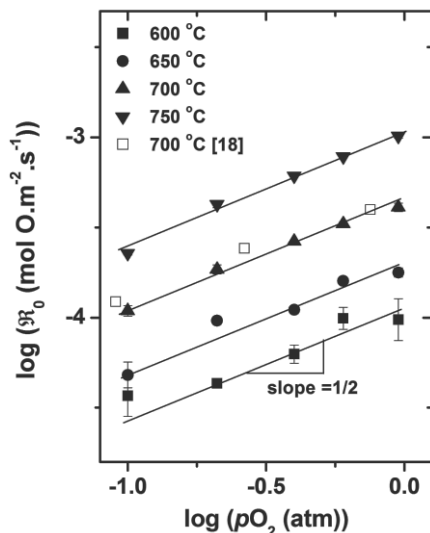
**Figure 5.3** Oxygen isotope fractions ( $^{18}\text{O}_2$ ,  $^{18}\text{O}^{16}\text{O}$ , and  $^{16}\text{O}_2$ ) as a function of temperature from PIE measurements at a nominal pressure of 0.21 atm. The drawn line is from model calculations, assuming constant activation energies for dissociative adsorption and incorporation over the entire temperature range. Error bars (for the 95% confidence interval of the mean) are smaller than the size of the symbols.

The temperature dependence of the surface exchange rate,  $\mathfrak{R}_0$ , calculated using Eq. (5.1) is well described by an Arrhenius equation, as shown in Fig. 5.4. Also shown in this figure are results from previous studies [11-13, 18], showing good agreement with those from the present study. The calculated activation energy of 111 (3)  $\text{kJ mol}^{-1}$  is in reasonable agreement with 130 (5)  $\text{kJ mol}^{-1}$  calculated from data obtained by monitoring the time-dependent  $^{18}\text{O}$ - $^{16}\text{O}$  isotopic equilibration on a polished BE25 dense ceramic disk in a closed volume [11, 18].



**Figure 5.4** Overall surface oxygen exchange rate for BE25 as a function of inverse temperature at a nominal pressure of 0.21 atm. Also shown are data from prior studies on BE25, obtained using time-dependent  $^{18}\text{O}$ - $^{16}\text{O}$  gas phase equilibration (Boukamp *et al.* [11, 18]) and  $^{18}\text{O}$ - $^{16}\text{O}$  isotope exchange followed by depth profiling (Steele *et al.* [12] and Capoen *et al.* [13]) methods. Error bars represent the 95% confidence interval of the mean; when not shown, these are smaller than the symbol size.

The surface exchange rates extracted from data of the depth-profiling studies displayed in Fig. 5.4 were recalculated using  $\mathfrak{R}_0 = k_s c_{\text{O}}$ , where  $k_s$  ( $\text{cm s}^{-1}$ ) is the surface exchange coefficient and  $c_{\text{O}}$  the concentration of oxygen ions in the oxide. It should be mentioned that it cannot be excluded that different preparation routes and pre-annealing temperatures, and departures from the targeted composition and/or contaminations may influence the magnitude of the surface exchange rate.



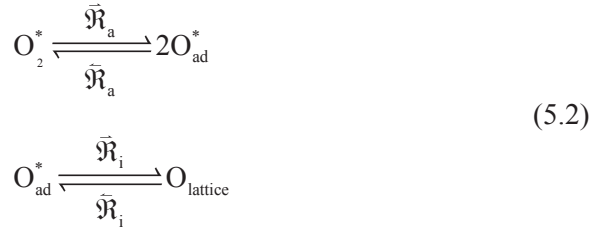
**Figure 5.5** Oxygen partial pressure dependence of the overall exchange rate on BE25 at different temperatures using PIE (filled symbol). Lines with slope 1/2 are given to guide the eye. Error bars represent the 95% confidence interval of the mean; when not shown, these are smaller than the symbol size. The data from time-dependent  $^{18}\text{O}$ - $^{16}\text{O}$  gas phase equilibration on BE25 dense ceramic at 700 °C reported by Boukamp *et al.* [18] (empty square symbol) is also included.

Fig. 5.5 shows the  $p\text{O}_2$  dependence of the overall surface exchange rate at different temperatures. At all four different temperatures,  $\mathfrak{R}_0$  is found approximately proportional to  $(p\text{O}_2)^n$  with  $n = 0.5$ , in nice agreement with results published previously [18].

The above results demonstrate the usefulness of PIE as a technique for acquisition of the oxygen surface exchange rate of fast oxygen-ionic conducting solids. The  $^{18}\text{O}$ -containing gas phase pulse passes through a ‘sea of  $^{16}\text{O}$ ’ captured by the oxide powder bed, ensuring in this way that  $^{16}\text{O}$  is returned to the gas phase upon every act of exchange. Measurements of the surface exchange rate are enabled as long as the effective time constant associated with

isotopic exchange is of similar order as the time scale of the experiment, *i.e.*, the residence time of the packed-bed reactor. These are determined by oxide characteristics, such as the powder surface area, and by design and operating conditions, such as the length of the packed-bed reactor, gas flow rate, and temperature, as can be inferred from Eq. (5.1). The design of the packed bed reactor to approximate plug flow conditions ensures that the distribution of residence times is small, and its average value simply can be calculated from the void volume of the reactor bed and the volumetric flow rate.

An advantage of methods based upon gas phase analysis to monitor  $^{18}\text{O}$ - $^{16}\text{O}$  isotope equilibration between the gas phase and the oxide over that of depth profiling methods is that kinetic information can be extracted from the mass isotopomer distribution resulting from isotopic scrambling. The isotopic exchange reaction can be modeled as a sequence of two steps, dissociative adsorption occurring with a rate  $\mathfrak{R}_a$ , and subsequent incorporation of oxygen in the oxide lattice with a rate  $\mathfrak{R}_i$ ,



and includes oxygen adatoms  $\text{O}_{\text{ad}}$  on the oxide surface as reaction intermediates. The  $^{18}\text{O}$  isotope fraction at the oxide surface is balanced by the reversible rates  $\mathfrak{R}_a$  and  $\mathfrak{R}_i$  in conjunction with the isotopic compositions of the gas phase and oxide. The validity of the two-step scheme for modeling isotopic exchange relies on the assumption that isotopic scrambling can only occur after dissociative adsorption of oxygen on the oxide surface, excluding for example, the

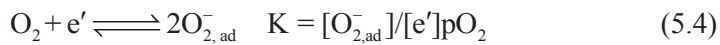
possibility that exchange may occur via a three-atom intermediate. In a quasi steady-state approximation for the isotopic exchange reaction, it follows

$$\frac{1}{\mathfrak{R}_0} = \frac{1}{\mathfrak{R}_a} + \frac{1}{\mathfrak{R}_i}. \quad (5.3)$$

The overall exchange process can be conceptually viewed as a series of resistances. Expressions for the corresponding molar gas phase fractions of  $^{18}\text{O}_2$ ,  $^{16}\text{O}^{18}\text{O}$ , and  $^{16}\text{O}_2$  after exchange for a given time within the framework of the two-step scheme are presented elsewhere [16, 18]. Finally, it should be noted that the surface exchange reaction may involve a series of steps with several possible intermediates, *e.g.*,  $\text{O}_2$ ,  $\text{O}_2^{2-}$ , and  $\text{O}^-$ . Both steps in the given two-step scheme still may represent a lumped reaction sequence with, for example, charge transfer and surface diffusion of atoms or ions as possible rate determining steps.

Fig. 5.6 (a)-(d) show the  $p\text{O}_2$  dependences of  $\mathfrak{R}_a$  and  $\mathfrak{R}_i$  for BE25 at different temperatures. The results indicate that the surface exchange reaction on BE25 is mainly limited by the rate of oxygen dissociative adsorption  $\mathfrak{R}_a$ . This result can be deduced intuitively from the very small molar  $^{18}\text{O}^{16}\text{O}$  fraction observed during isotopic exchange, as illustrated in Fig. 5.3. At all temperatures,  $\mathfrak{R}_a$  appears proportional to  $p\text{O}_2^{1/2}$ , in obvious correspondence with the  $p\text{O}_2$  dependence of  $\mathfrak{R}_0$ , and found one to two orders of magnitude lower than  $\mathfrak{R}_i$ .

The dissociative adsorption of oxygen on the surface can be represented by the successive reaction steps



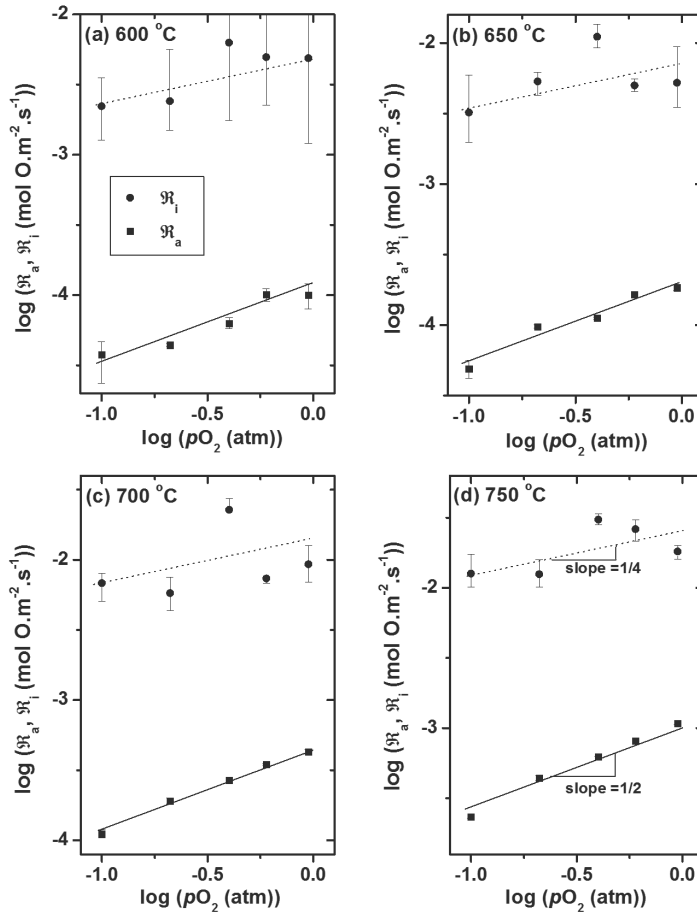


**Figure 5.6** The oxygen partial pressure dependence of the rates of dissociative adsorption ( $\mathcal{R}_a$ , filled square) and oxygen incorporation ( $\mathcal{R}_i$ , filled circle) at different temperatures. Trendlines with slopes 1/2 and 1/4 are given to guide the eye. Error bars represent the 95% confidence interval of the mean; when not shown, these are smaller than the symbol size.

where  $K$  is the mass action constant of reaction (5.4). The observed  $p\text{O}_2^{1/2}$  dependence of  $\mathcal{R}_a$  can be explained by assuming that electron transfer to in-

intermediate superoxide ions,  $O_2^-$ , according to reaction (5.5), is the rate determining step in oxygen dissociative adsorption. Noting that the isotopic exchange experiment is carried out under conditions of equilibrium,  $\mathfrak{R}_a = \bar{\mathfrak{R}}_a = \tilde{\mathfrak{R}}_a$ , where  $\bar{\mathfrak{R}}_a = \bar{k}[O_{2,ad}^-][e']$  and  $\tilde{\mathfrak{R}}_a = \bar{k}[O_{ad}^-]^2$  are the balanced forward and backward reaction rates, respectively, and  $\bar{k}$  and  $\bar{k}$  the corresponding rate constants. In deriving these kinetic equations, a low surface coverage of adsorbed oxygen species is assumed. To infer the  $pO_2$  dependence of  $\mathfrak{R}_a$ , those of the concentrations entering these kinetic equations must be derived from preceding or succeeding equilibria. Under the experimental conditions, the bulk concentration of oxygen vacancies in BE25 is invariant with  $pO_2$ . From defect chemical considerations, it follows that for BE25 the concentration of electrons varies according to  $[e'] \propto pO_2^{1/4}$ . Substitution in the expression for  $\bar{\mathfrak{R}}_a$  ( $= \bar{k}[O_{2,ad}^-][e'] = K\bar{k}[e']^2 pO_2$ ) shows that in accord with the experimental observations  $\mathfrak{R}_a$  is predicted to follow a  $pO_2^{1/2}$  dependence. Reaction (5.5) may proceed via formation of a transient peroxide intermediate,  $O_2^{2-}$ , which is known to be very unstable, before actual splitting of the adsorbed oxygen molecule into oxygen adatoms  $O_{ad}^-$ .

As seen from Fig. 5.6 (a)-(d), the rate of oxygen incorporation  $\mathfrak{R}_i$  shows a weak dependence on  $pO_2$ . The trend lines in these figures with a slope of 1/4 should be considered with care given the large scatter in the obtained values of  $\mathfrak{R}_i$ .  $\mathfrak{R}_i$  may either refer to a successive reaction step or to diffusion of  $O_{ad}^-$  or electron holes to the reaction site. More research is, however, needed for clarification.

Finally, Fig. 5.7 shows a graphical collection of data obtained for the surface oxygen exchange rate observed on various oxides using different tech-

niques. It is seen that BE25 shows a comparatively high surface exchange rate, much higher than well-known solid electrolytes YSZ and gadolinia-doped ceria, and even higher than  $\text{La}_2\text{NiO}_4$ , which has been proposed as a cathode material for intermediate-temperature SOFCs [19, 20].

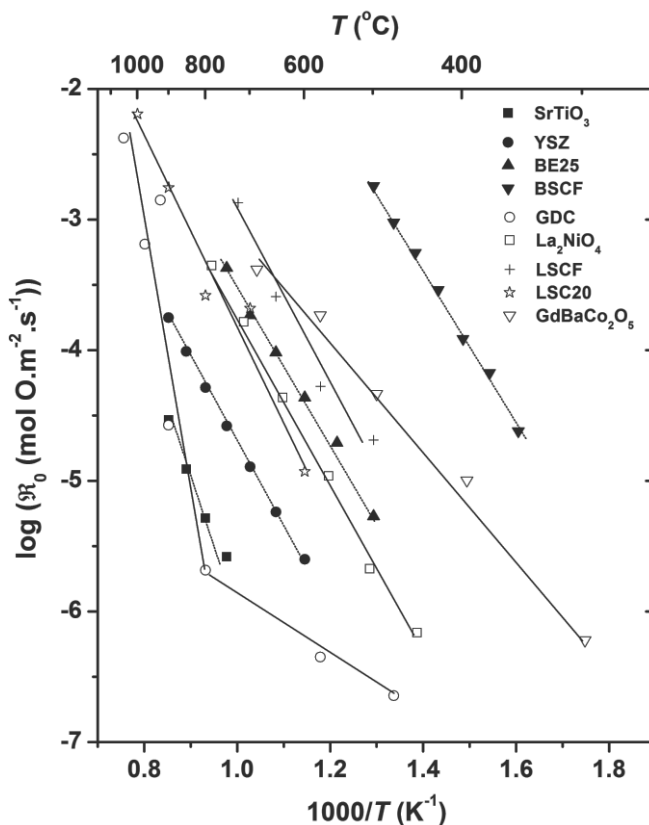


**Figure 5.7** Surface oxygen exchange rates for different oxides as a function of inverse temperature.  $\text{SrTiO}_3$  [21], 8 mol% yttria-stabilized zirconia (YSZ) [16], BE25 (this study),  $\text{Ba}_{0.5}\text{Sr}_{0.5}\text{Co}_{0.8}\text{Fe}_{0.2}\text{O}_{3-\delta}$  (BSCF) [16], 10 mol% gadolinia-doped  $\text{CeO}_2$  (GDC) [22],  $\text{La}_2\text{NiO}_4$  [19],  $\text{La}_{0.6}\text{Sr}_{0.4}\text{Co}_{0.2}\text{Fe}_{0.8}\text{O}_{3-\delta}$  (LSCF) [23],  $\text{La}_{0.8}\text{Sr}_{0.2}\text{CoO}_{3-\delta}$  (LSC20) [24], and  $\text{GdBaCo}_2\text{O}_5$  [25].



## **5.4 Conclusions**

The results obtained from this study indicate that in the temperature and  $pO_2$  ranges investigated BE25 exhibits a comparatively high exchange rate, which is rate determined by the dissociative adsorption of oxygen. Electron transfer to intermediate superoxide ions is proposed as the rate determining step. The results further demonstrate the usefulness of pulse-based measurements of  $^{18}O$ - $^{16}O$  isotope exchange, which method employs a continuous flow packed bed microreactor, for kinetic and mechanistic studies of surface oxygen exchange of fast ionic conducting solids.

## References

1. T. Takahashi, T. Esaka, H. Iwahara, J. Solid State Chem. 16 (1976) 317.
2. P. Shuk, H.D. Wiemhofer, U. Guth, W. Gopel, M. Greenblatt, Solid State Ionics 89 (1996) 179.
3. N.M. Sammes, G.A. Tompsett, H. Nafe, F. Aldinger, J. Eur. Ceram. Soc. 19 (1999) 1801.
4. N.X. Jiang, E.D. Wachsman, S.H. Jung, Solid State Ionics 150 (2002) 347.
5. M.J. Verkerk, A.J. Burggraaf, J. Electrochem. Soc. 130 (1983) 78.
6. M.J. Verkerk, M.W.J. Hammink, A.J. Burggraaf, J. Electrochem. Soc. 130 (1983) 70.
7. H. Kruidhof, H.J.M. Bouwmeester, K.J. de Vries, P.J. Gellings, A.J. Burggraaf, Solid State Ionics 50 (1992) 181.
8. N.X. Jiang, E.D. Wachsman, J. Am. Ceram. Soc. 82 (1999) 3057.
9. H.S. Isaacs, L.J. Olmer, J. Electrochem. Soc. 129 (1982) 436.
10. D.Y. Wang, A.S. Nowick, J. Electrochem. Soc. 128 (1981) 55.
11. B.A. Boukamp, B.A. van Hassel, I.C. Vinke, K.J. de Vries, A.J. Burggraaf, Electrochim. Acta 38 (1993) 1817.
12. B.C.H. Steele, J.A. Kilner, P.F. Dennis, A.E. McHale, M. van Hemert, A.J. Burggraaf, Solid State Ionics 18-19 (1986) 1038.
13. E. Capoen, G. Nowogrocki, R.J. Chater, S.J. Skinner, J.A. Kilner, M. Mays, J.C. Boivin, G. Mairesse, R.N. Vannier, Solid State Ionics 177 (2006) 489.
14. H.J.M. Bouwmeester, H. Kruidhof, A.J. Burggraaf, Solid State Ionics 72 (1994) 185.
15. H.J.M. Bouwmeester, H. Kruidhof, A.J. Burggraaf, P.J. Gellings, Solid State Ionics 53-56 (1992) 460.
16. H.J.M. Bouwmeester, C. Song, J. Zhu, J. Yi, M. van Sint Annaland, B.A. Boukamp, Phys. Chem. Chem. Phys. 11 (2009) 9640.
17. M.J. Verkerk, K. Keizer, A.J. Burggraaf, J. Appl. Electrochem. 10 (1980) 81.
18. B.A. Boukamp, I.C. Vinke, K.J. de Vries, A.J. Burggraaf, Solid State Ionics 32-33 (1989) 918.
19. S.J. Skinner, J.A. Kilner, Solid State Ionics 135 (2000) 709.
20. R. Sayers, J. Liu, B. Rustumji, S.J. Skinner, Fuel Cells 8 (2008) 338.
21. Chapter 6 of this thesis.
22. J.A. Lane, J.A. Kilner, Solid State Ionics 136 (2000) 927.
23. A. Esquirol, J.A. Kilner, N. Brandon, Solid State Ionics 175 (2004) 63.
24. R.A. De Souza, J.A. Kilner, Solid State Ionics 126 (1999) 153.

*Chapter 5*

---

25. A. Tarancon, S.J. Skinner, R.J. Chater, F. Hernandez-Ramirez, J.A. Kilner, J. Mater. Chem. 17 (2007) 3175.

---

## Chapter 6

# Oxygen surface exchange kinetics of $\text{SrTi}_{1-x}\text{Fe}_x\text{O}_{3-\delta}$ mixed conducting oxides

### Abstract

The oxygen surface exchange kinetics of mixed conducting perovskite oxides  $\text{SrTi}_{1-x}\text{Fe}_x\text{O}_{3-\delta}$  ( $x = 0, 0.01, 0.05, 0.35, 0.5$ ) has been investigated as a function of temperature and oxygen partial pressure using the pulse-response  $^{18}\text{O}$ - $^{16}\text{O}$  isotope exchange (PIE) technique. Arrhenius activation energies range from  $140 \text{ kJ mol}^{-1}$  for  $x = 0$  to  $86 \text{ kJ mol}^{-1}$  for  $x = 0.5$ . Extrapolating the temperature dependence to the intermediate temperature range,  $500\text{-}600 \text{ }^\circ\text{C}$ , indicates that the rate of oxygen exchange, in air, increases with increasing iron mole fraction, but saturates at the highest iron mole fraction for the given series. The observed behavior is concomitant with corresponding increases of both electronic and ionic conductivity with increasing  $x$  in  $\text{SrTi}_{1-x}\text{Fe}_x\text{O}_{3-\delta}$ . Including literature data of related perovskite-type oxides  $\text{Ba}_{0.5}\text{Sr}_{0.5}\text{Co}_{0.8}\text{Fe}_{0.2}\text{O}_{3-\delta}$ ,  $\text{La}_{0.6}\text{Sr}_{0.4}\text{Co}_{0.2}\text{Fe}_{0.8}\text{O}_{3-\delta}$ ,  $\text{La}_{0.6}\text{Sr}_{0.4}\text{CoO}_{3-\delta}$ , and  $\text{Sm}_{0.5}\text{Sr}_{0.5}\text{CoO}_{3-\delta}$ , a linear relationship is observed in the log-log plot between oxygen exchange rate and oxide ionic conductivity with a slope fairly close to unity, suggesting that it is the magnitude of the oxide ionic conductivity that governs the rate of oxygen exchange in these solids. The distribution of oxygen isotopomers ( $^{16}\text{O}_2$ ,  $^{16}\text{O}^{18}\text{O}$ ,

$^{18}\text{O}_2$ ) in the effluent pulse can be interpreted on the basis of a two-step exchange mechanism for the isotopic exchange reaction. Accordingly, the observed power law dependence of the overall surface exchange rate on oxygen partial pressure turns out to be an apparent one, depending on the relative rates of both steps involved in the adopted two-step scheme. Supplementary research is, however, required to elucidate which of the two possible reaction schemes better reflects the actual kinetics of oxygen surface exchange on  $\text{SrTi}_{1-x}\text{Fe}_x\text{O}_{3-\delta}$ .

## 6.1 Introduction

The non-stoichiometric perovskite oxides  $\text{SrTi}_{1-x}\text{Fe}_x\text{O}_{3-\delta}$  (STF) have received considerable attention for use as resistive oxygen sensor in lean burn engines [1-3], as cathode for the solid oxide fuel cell [4], and as oxygen separation membrane [5]. The series  $\text{SrTi}_{1-x}\text{Fe}_x\text{O}_{3-\delta}$  forms a continuous solid solution between end members  $\text{SrTiO}_3$  and  $\text{SrFeO}_3$ . The partial ionic and electronic conductivities can be varied over several orders of magnitude by partial substitution of iron for titanium in  $\text{SrTiO}_3$ . Whereas  $\text{SrTiO}_3$ , is essentially a wide band gap semiconductor with low conductivity [6, 7], nonstoichiometric  $\text{SrFeO}_{3-\delta}$  is a mixed ionic-electronic conductor with high electronic and ionic conductivities [8]. Pure  $\text{SrFeO}_{3-\delta}$ , however, undergoes an order-disorder phase transition below 850 °C from disordered perovskite ( $\text{SrFeO}_{3-\delta}$ , space group  $Pm\bar{3}m$ ) to ordered brownmillerite ( $\text{Sr}_2\text{Fe}_2\text{O}_5$ , space group  $Icmm$ ), which limits its application [9, 10]. The substitution of iron for titanium stabilizes the disordered perovskite phase, retaining a high electronic and ionic conductivity over a wide range of oxygen partial pressure and temperature [10, 11].

Recently, Jung and Tuller [12-14] found the area specific resistance of  $\text{SrTi}_{1-x}\text{Fe}_x\text{O}_{3-\delta}$  ( $x = 0.35$  and  $0.5$ ) to be significantly lower than those of more typical SOFC electrodes such as  $\text{La}_{0.8}\text{Sr}_{0.2}\text{CoO}_{3-\delta}$  and  $\text{La}_{0.6}\text{Sr}_{0.4}\text{Co}_{0.2}\text{Fe}_{0.8}\text{O}_{3-\delta}$

[15]. The observations inspired us to conduct a systematic study towards surface oxygen exchange on SrTi<sub>1-x</sub>Fe<sub>x</sub>O<sub>3-δ</sub>. In this paper, we report a study on oxygen surface exchange of SrTi<sub>1-x</sub>Fe<sub>x</sub>O<sub>3-δ</sub> ( $x = 0, 0.01, 0.05, 0.35, \text{ and } 0.5$ ) as a function of temperature and oxygen partial pressure, using the <sup>18</sup>O-<sup>16</sup>O pulse isotope exchange (PIE) technique recently developed in our laboratory [16, 17].

## **6.2 Experimental**

### **6.2.1 Sample preparation and analysis**

SrTiO<sub>3</sub> (STO) was purchased from Sigma Aldrich. Using X-ray fluorescence (Philips PW1480), 0.4 mol% Ba, 0.02 mol% Fe, 0.05 mol% Ca and 0.01 mol% K were found to be present as major impurities. Powders of SrTi<sub>0.99</sub>Fe<sub>0.01</sub>O<sub>3-δ</sub> (STF1), SrTi<sub>0.95</sub>Fe<sub>0.05</sub>O<sub>3-δ</sub> (STF5), SrTi<sub>0.65</sub>Fe<sub>0.35</sub>O<sub>3-δ</sub> (STF35), and SrTi<sub>0.5</sub>Fe<sub>0.5</sub>O<sub>3-δ</sub> (STF50) were prepared by conventional solid state reaction at 1000-1200 °C for 12-24 h using commercial SrCO<sub>3</sub>, TiO<sub>2</sub>, and Fe<sub>2</sub>O<sub>3</sub> (Sigma Aldrich) with intermediate grinding steps. The commercial powders were used as received from the manufacturer. Prior to use, STO and prepared STF powders were uniaxially pressed at 25 MPa into a pellet, followed by cold isostatic pressing at 400 MPa, and then sintered in air at 1200-1400 °C for 10-15 h. Each of the sintered pellets was then crushed into a coarse powder, which was sieved with a 120 mesh metal sieve. The sieved powder was annealed in air at 950 °C for 10 h, and then sieved again with a 120 mesh metal sieve to remove possibly formed agglomerates. The phase purity and morphology of the powders thus obtained were examined by X-ray diffraction (PANalytical PW1830) and scanning electron microscopy (JEOL JSM-5600LV). Lattice parameters were calculated using the FullProf program [18]. Particle size and BET surface area measurements were conducted using a Mastersizer 2000 (Malvern Instruments) and an ASAP 2020M (Micromeritics), respectively.

Particle sizes ( $d_{50}$ ) and BET surface areas were in the range of 0.6-1.5  $\mu\text{m}$  and 0.2-1.2  $\text{m}^2 \text{g}^{-1}$ , respectively.

### 6.2.2 Pulse-response $^{18}\text{O}$ - $^{16}\text{O}$ isotope exchange measurements

Pulse  $^{18}\text{O}$ - $^{16}\text{O}$  isotope exchange (PIE) measurements were performed in the range of temperature and oxygen partial pressure 300-900  $^{\circ}\text{C}$  and 0.1-0.95 atm, respectively, using a continuous flow packed-bed micro-reactor. During the measurement, the sample powder was loaded in the center of the quartz tubular micro-reactor having an inner diameter of 2 mm. Quartz wool plugs were used on both sides of the packed-powder bed to ensure its integrity. Typical values for the powder mass and length of the powder bed were in the range 0.05-0.09 g and 10-14 mm, respectively. A  $^{16}\text{O}_2/\text{Ar}$  gas mixture was used as the carrier gas with a flow rate of 50  $\text{ml min}^{-1}$  (NTP). The response to an  $^{18}\text{O}_2$ -enriched  $\text{N}_2$  gas pulse (500  $\mu\text{l}$ ) fed through the reactor, with the same  $p\text{O}_2$  as carrier gas, was analyzed by on-line mass spectrometry (Omni Star TM GSD 301 Pfeiffer-Vacuum). Oxygen isotope gas ( $> 97$  atom%  $^{18}\text{O}_2$ ) was purchased from Cambridge Isotope Laboratory. A six-port valve was used for injection of the  $^{18}\text{O}_2/\text{N}_2$  pulse into the  $^{16}\text{O}_2/\text{Ar}$  carrier gas flow stream. Nitrogen used as diluent gas for  $^{18}\text{O}_2$  was also used for calibration of the mass spectrometer. The mean residence time of the reactor varied between 8 to 30 ms, depending on the volumetric flow rate at the temperature of the measurement and the packed bed length. Prior to measurements, the packed powder bed was pre-treated at 850  $^{\circ}\text{C}$  for 0.5 h under flowing, synthetic air to remove any adsorbed water and  $\text{CO}_2$ , and subsequently cooled to room temperature at a rate of 5  $^{\circ}\text{C min}^{-1}$ . The powder-packed bed microreactor was pre-equilibrated 0.5 h at each temperature and  $p\text{O}_2$  before data collection. Within the experimental range of temperature, blank experiments revealed no significant exchange activity of the empty quartz micro-reactor.

Data acquisition during PIE experiments was carried out by measuring the isotope fractions of <sup>18</sup>O<sub>2</sub> and <sup>16</sup>O<sup>18</sup>O in the effluent pulse. The integrated peak area for <sup>16</sup>O<sup>18</sup>O was corrected for tailing, if present, by linear interpolation of the background. The average result of three pulse experiments at a given temperature and *p*O<sub>2</sub> was used for calculation of the surface exchange rate,  $\mathfrak{R}_0$  (mol O m<sup>-2</sup> s<sup>-1</sup>), from [16, 17]

$$\mathfrak{R}_0 = \frac{n}{\tau_r S} \ln \left( \frac{f_{g,i}^{18}}{f_{g,e}^{18}} \right) \quad (6.1)$$

where  $f_{g,i}^{18}$  and  $f_{g,e}^{18}$  are the <sup>18</sup>O isotope molar fractions in the pulse at the inlet and exit of the reactor, respectively, *n* the total number of oxygen atoms in the free volume of the packed bed, *S* the total surface area within the packed bed, and  $\tau_r$  the average residence time of the labeled gas in the reactor. The value of  $f_g^{18}$  was calculated from

$$f_g^{18} = 0.5f_g^{34} + f_g^{36} \quad (6.2)$$

where  $f_g^{36}$  and  $f_g^{34}$  are the isotope fractions of <sup>18</sup>O<sub>2</sub> and <sup>16</sup>O<sup>18</sup>O, respectively. More details of the pulse isotope exchange experiments and theory are given elsewhere [16, 17].

## 6.3 Results and discussion

### 6.3.1 Sample characterization

The room temperature X-ray diffraction patterns for SrTi<sub>1-x</sub>Fe<sub>x</sub>O<sub>3-δ</sub> with *x* ranging from 0 to 0.5 confirm that all compositions exhibit a single cubic perovskite phase. The corresponding lattice parameters are listed in Table 6.1. These are found to be in good agreement with previously published data [19]. The decrease of the cubic lattice parameter with *x* in SrTi<sub>1-x</sub>Fe<sub>x</sub>O<sub>3-δ</sub> is con-



sistent with the substitution of octahedral  $\text{Ti}^{4+}$  (0.605 Å) with smaller  $\text{Fe}^{4+}$  (0.585 Å) or low-spin  $\text{Fe}^{3+}$  (0.55 Å) ions, noting that an increase is expected upon substitution with high-spin  $\text{Fe}^{3+}$  (0.645 Å) ions. Values for the listed ionic radii were taken from Shannon [20]. No evidence was found in the X-ray diffraction patterns for ordering or impurity phases. Back scattered SEM images showed a homogeneous micro-structure for all compositions.

**Table 6.1** Cubic lattice parameter (Å) of  $\text{SrTi}_{1-x}\text{Fe}_x\text{O}_{3-\delta}$ .

x = 0	x = 0.01	x = 0.05	x = 0.35	x = 0.5
3.9096 (2)	3.9064 (7)	3.9049 (3)	3.9003 (1)	3.8925 (8)

### 6.3.2 Pulse isotopic exchange (PIE) measurements

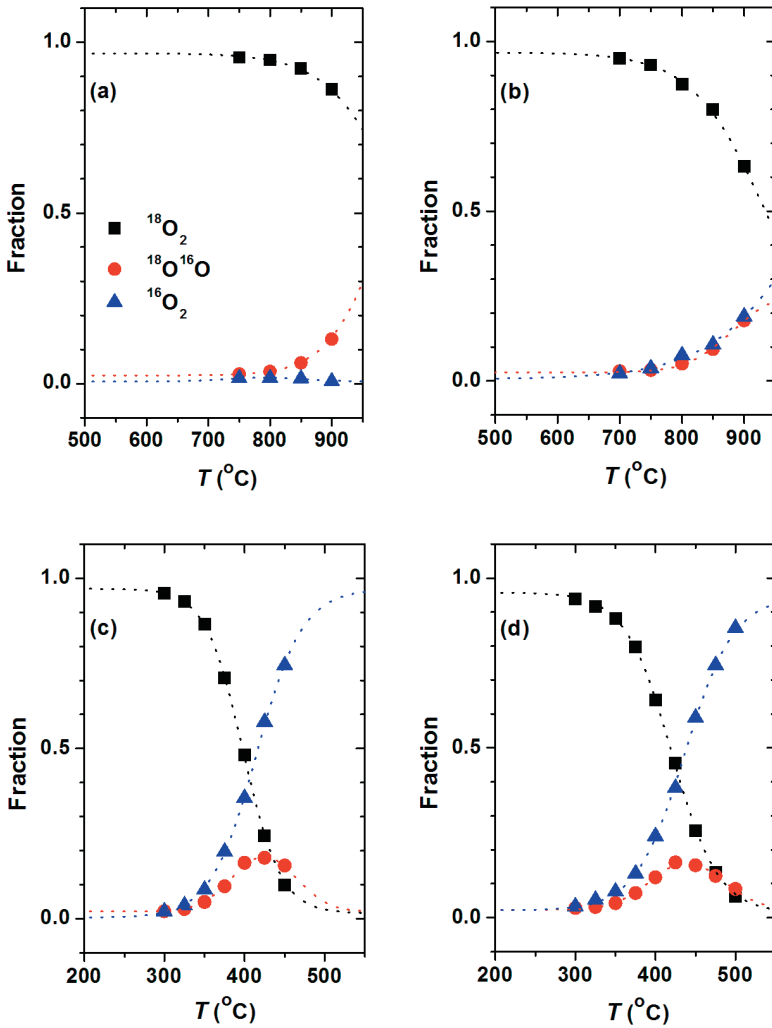
Experimental data for the oxygen isotope fractions ( $f_g^{32}$ ,  $f_g^{34}$ , and  $f_g^{36}$ ), from PIE measurements, at a  $p\text{O}_2$  of 0.21 atm, as a function of temperature for selected STF compositions is shown in Fig. 6.1. Under the conditions of the experiments, the uptake of  $^{18}\text{O}$  by STO becomes significant at  $\sim 750$  °C. For STF35 and STF50, the uptake occurs at much lower temperatures,  $\sim 300$  °C, reflecting the higher exchange activities for these solids relative to pure STO. The decrease in the isotope fraction of  $^{18}\text{O}_2$  ( $f_g^{36}$ ) with increasing temperature is balanced by increases in the fractions  $^{16}\text{O}_2$  ( $f_g^{32}$ ) and  $^{18}\text{O}^{16}\text{O}$  ( $f_g^{34}$ ). This behavior, found to be different for each of the compositions, acts as a *finger-print* for the relative rate of  $\text{O}_2$  dissociative adsorption to that of oxygen incorporation. This is further discussed in Section 6.3.4.

Fig. 6.2 shows corresponding Arrhenius plots of the overall surface exchange rate,  $\mathfrak{R}_0$ , calculated using Eq. (6.1). Though direct comparison of the

data obtained for different compositions is somewhat restricted due to the limited temperature window of the PIE measurements,  $\mathfrak{R}_0$  is seen to be remarkably enhanced by increasing the iron concentration in SrTi<sub>1-x</sub>Fe<sub>x</sub>O<sub>3-δ</sub>. Fig. 6.3 shows estimated values of  $\mathfrak{R}_0$ , obtained from extrapolation to 500 and 600 °C, as a function of iron concentration. At both temperatures,  $\mathfrak{R}_0$  increases more than 3 orders of magnitude on going from STO to STF50.  $\mathfrak{R}_0$  is seen to saturate at the highest iron concentrations, corresponding to STF35 and STF50. Activation energies of the oxygen exchange rate for SrTi<sub>1-x</sub>Fe<sub>x</sub>O<sub>3-δ</sub> calculated from the Arrhenius plots shown in Fig. 6.2 are listed in Table 6.2. These clearly show a trend of decreasing activation energy with increasing iron concentration.

**Table 6.2** Apparent activation energies (kJ mol<sup>-1</sup>) of the rates of overall oxygen surface exchange ( $\mathfrak{R}_0$ ), oxygen dissociative adsorption ( $\mathfrak{R}_a$ ), and oxygen incorporation ( $\mathfrak{R}_i$ ) for SrTi<sub>1-x</sub>Fe<sub>x</sub>O<sub>3-δ</sub> (x = 0, 0.01, 0.05, 0.35, and 0.5). Standard errors are given in parentheses and refer to the least significant decimals.

x	$\mathfrak{R}_0$	$\mathfrak{R}_a$	$\mathfrak{R}_i$
0	140 (7)	326 (57)	15 (4)
0.01	133 (5)	160 (6)	71 (13)
0.05	110 (5)	105 (8)	101 (9)
0.35	111 (3)	110 (5)	71 (6)
0.5	86 (2)	88 (4)	84 (3)



**Figure 6.1** Oxygen isotope fractions ( $^{18}\text{O}_2$ ,  $^{18}\text{O}^{16}\text{O}$ , and  $^{16}\text{O}_2$ ) as a function of temperature from PIE measurements, at  $p\text{O}_2 = 0.21$  atm, on  $\text{SrTi}_{1-x}\text{Fe}_x\text{O}_{3-\delta}$  for (a)  $x = 0$ , (b)  $x = 0.01$ , (c)  $x = 0.35$ , and (d)  $x = 0.5$ . The drawn line is from model calculations on the basis of a two-step model for isotopic exchange (scheme (6.4)), assuming constant activation energies for the rates of dissociative adsorption and oxygen incorporation, as discussed in Section 6.3.4.

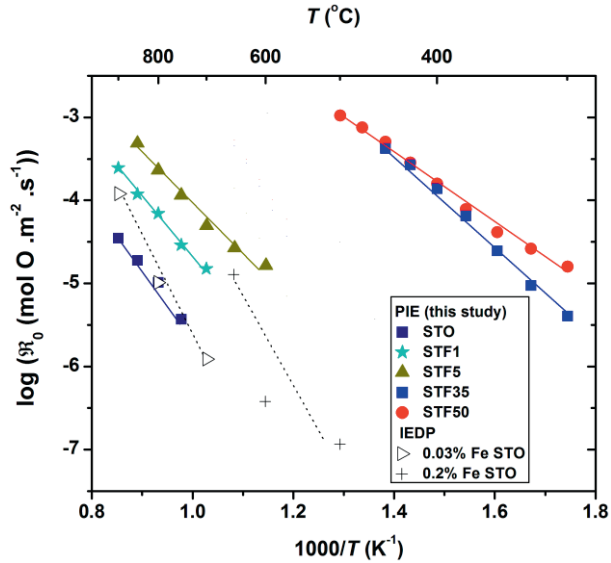


**Figure 6.2** Temperature dependence of the overall oxygen surface exchange rate,  $\mathfrak{R}_0$ , for  $\text{SrTi}_{1-x}\text{Fe}_x\text{O}_{3-\delta}$  ( $x = 0, 0.01, 0.05, 0.35,$  and  $0.5$ ) from PIE measurements, at  $p\text{O}_2 = 0.21$  atm. Data for 0.03 mol% Fe-doped STO and 0.2 mol% Fe-doped STO from isotope exchange followed by SIMS depth profiling from literature are shown for comparison [21, 22].

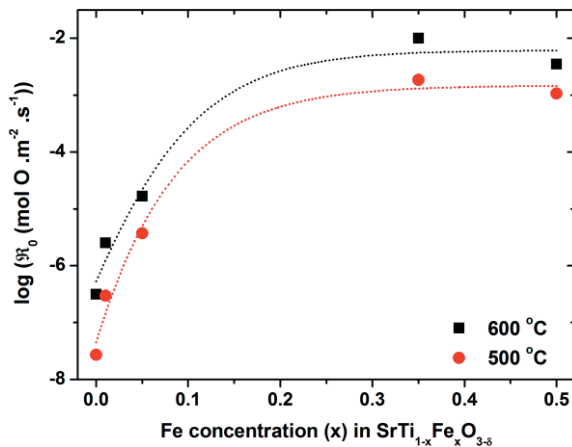


**Figure 6.3** Oxygen surface exchange rate,  $\mathfrak{R}_0$ , for  $\text{SrTi}_{1-x}\text{Fe}_x\text{O}_{3-\delta}$  as a function of iron concentration ( $x$ ).

### 6.3.3 Correlation between oxygen surface exchange rate and partial conductivities

Knowledge about the oxygen surface exchange kinetics on oxide ion conducting oxides is essential to optimize the performance of devices incorporating these solids, such as cathodes for fuel cells, and oxygen separation membranes. The nature of the interaction between gaseous  $O_2$  and surfaces, however, is one of the most fundamental issues in heterogeneous catalysis, but one which is presently still poorly understood.

It is generally conceived that oxygen surface exchange comprises a number of steps, including gas phase diffusion, adsorption, electronation, dissociation, surface diffusion of intermediate oxygen species, and oxygen incorporation. The presence of so-called coordinatively unsaturated sites (CUS), *i.e.*, surface metal atoms not capped with oxygen and onto which  $O_2$  can be chemisorbed, and surface oxygen vacancies are considered to play an essential role in the reaction pathway for oxygen incorporation. Different oxygen species have been postulated to occur as possible intermediates for the oxygen reduction reaction, such as superoxide ions ( $O_2^-$ ), peroxide ions ( $O_2^{2-}$ ), and oxygen adatoms ( $O^-$ ), before actual incorporation of these into the oxide lattice.

The overall oxygen surface exchange reaction can be written as, using Kröger-Vink notation,



from which it is intuitively apparent that lattice oxygen vacancies and electrons at the oxide surface, both in terms of concentration and mobility, are expected to play a role in determining the rate of surface exchange. Reaction (6.3) is usually written in terms of electron holes ( $h'$ ) if, rather than the transfer of electrons from the conduction band to the oxygen adsorbate at the surface, the

electrons are transferred from the valence band. Boukamp *et al.* [23] were the first to note that a high electronic conductivity is a prerequisite for an oxide to exhibit fast oxygen surface exchange kinetics. Indeed, at given  $pO_2$  and temperature, the exchange rate increases profoundly traversing from yttria-stabilized zirconia to stabilized bismuth oxide, and subsequently to the mixed-conducting perovskite oxides, *e.g.*, La<sub>1-x</sub>Sr<sub>x</sub>Co<sub>y</sub>Fe<sub>1-y</sub>O<sub>3-δ</sub>, and so does the electronic conductivity of these materials. Wang *et al.* [24] recently established a correlation between the effective oxygen exchange rate for Ba<sub>1-x</sub>Sr<sub>x</sub>Co<sub>y</sub>Fe<sub>1-y</sub>O<sub>3-δ</sub>, extracted from impedance data of dense microelectrodes, and the product of the concentration and mobility of oxygen vacancies in these materials, emphasizing on the important role of the oxygen mobility on the exchange rate. An important role of oxygen vacancies is also inferred from the empirical correlations between the surface exchange coefficient and the oxygen tracer diffusion coefficient found by De Souza and Kilner [25], after reviewing a large number of data sets from isotopic exchange depth profiling studies of acceptor-doped perovskite- and fluorite-type oxides. In a more recent study, De Souza [26] challenged this view by proposing a universal rate expression, accounting for the  $pO_2$  dependence of the exchanges rate observed for selected materials. The author claimed that rather low concentrations of oxygen vacancies and high concentrations of electronic charge carriers would lead to high exchange rates. It is clear from the above that more experimental evidence is required to resolve these ambiguities.

To examine the role of partial conductivities in affecting the surface exchange kinetics, the values of  $\mathfrak{R}_0$  obtained for compositions SrTi<sub>1-x</sub>Fe<sub>x</sub>O<sub>3-δ</sub> are plotted against published values for the electronic ( $\sigma_e$ ) and ionic conductivity ( $\sigma_i$ ) in Figs. 6.4 (a) and (b), respectively [3, 11, 27]. The plotted values refer to data obtained, at 600 °C, in air. In both figures, a correlation is apparent between  $\mathfrak{R}_0$  and the corresponding partial conductivity. However, when the data

is extended to include corresponding data for  $\text{Ba}_{0.5}\text{Sr}_{0.5}\text{Co}_{0.8}\text{Fe}_{0.2}\text{O}_{3-\delta}$  (BSCF) [16, 28, 29],  $\text{La}_{0.6}\text{Sr}_{0.4}\text{Co}_{0.2}\text{Fe}_{0.8}\text{O}_{3-\delta}$  (LSCF) [30, 31],  $\text{La}_{0.6}\text{Sr}_{0.4}\text{CoO}_{3-\delta}$  (60LSC) [32, 33], and  $\text{Sm}_{0.5}\text{Sr}_{0.5}\text{CoO}_{3-\delta}$  (50SSC) [34, 35], no longer correlation is found between  $\mathfrak{R}_0$  and  $\sigma_e$ , whereas that between  $\mathfrak{R}_0$  and  $\sigma_i$  is retained.  $\mathfrak{R}_0$  displays a power law dependence on  $\sigma_i$  with exponent  $1.2 (\pm 0.2)$  (see Fig. 6.4 (b)), which spans more than 3 orders of magnitude in the value of the ionic conductivity. Like the earlier studies conducted by De Souza and Kilner [25] and Wang *et al.* [24], the results emphasize the importance of oxide ion conductivity on the rate of oxygen surface exchange. The correlation concerns the oxide ion conductivity, *i.e.*, the product of vacancy concentration and vacancy diffusion coefficient, rather than each of these quantities separately. The observed power law exponent of  $1.2 (\pm 0.2)$  is found to be in very good agreement with the value of 1.16 evaluated by Wang *et al.* [24] for phases  $\text{Ba}_{1-x}\text{Sr}_x\text{Co}_y\text{Fe}_{1-y}\text{O}_{3-\delta}$  (at 600 °C). It must be said, however, that the present results are in conflict with data from impedance measurements on  $\text{SrTi}_{1-x}\text{Fe}_x\text{O}_{3-\delta}$  electrodes, prepared by pulsed laser deposition on oriented single crystal yttria-stabilized substrates, as reported recently by Jung and Tuller [13, 14]. In the latter study, the authors only found a weak dependence of the effective exchange rate on both  $\sigma_e$  and  $\sigma_i$ , with power law exponents of  $0.15 (\pm 0.03)$  and  $0.20 (\pm 0.02)$  at 650 °C, and  $0.07 (\pm 0.02)$  and  $0.11 (\pm 0.02)$  at 800 °C, respectively, for which we have no explanation.

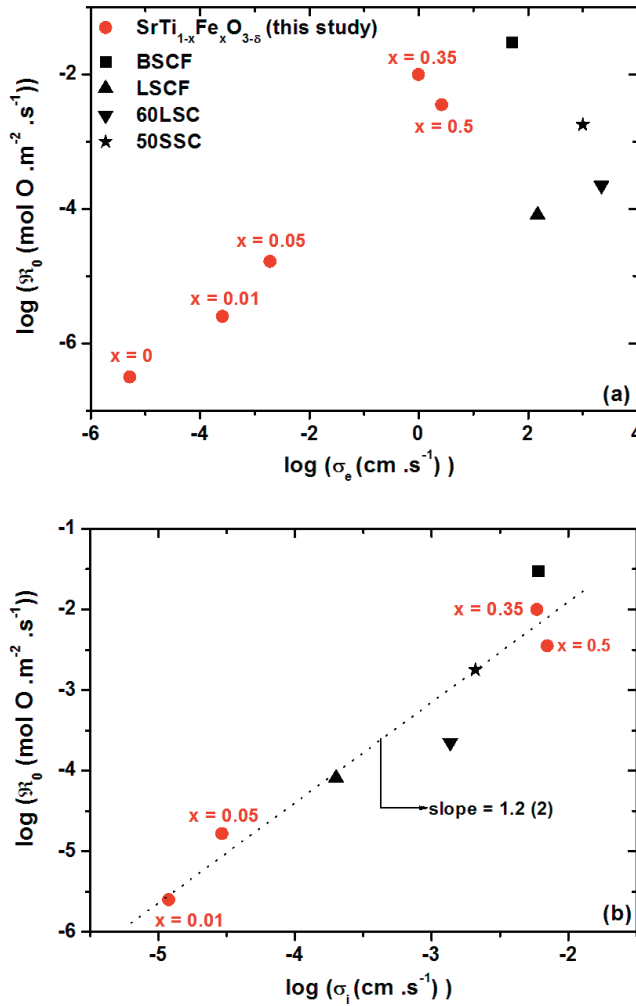
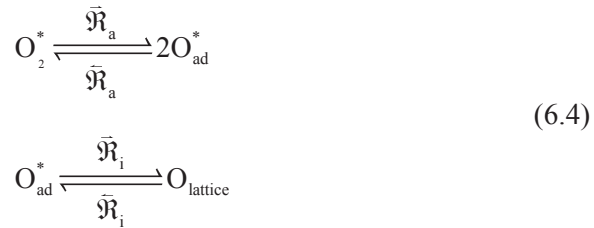


**Figure 6.4** Oxygen exchange rate ( $\mathfrak{R}_0$ ) versus partial conductivity: (a) electronic conductivity ( $\sigma_e$ ), and (b) ionic conductivity ( $\sigma_i$ ). Data refer to  $T = 600$  °C and  $p\text{O}_2 = 0.21$  atm.  $\text{SrTi}_{1-x}\text{Fe}_x\text{O}_{3-\delta}$  [this study, 3, 11, 27],  $\text{Ba}_{0.5}\text{Sr}_{0.5}\text{Co}_{0.8}\text{Fe}_{0.2}\text{O}_{3-\delta}$  (BSCF) [16, 28, 29],  $\text{La}_{0.6}\text{Sr}_{0.4}\text{Co}_{0.2}\text{Fe}_{0.8}\text{O}_{3-\delta}$  (LSCF) [30, 31],  $\text{La}_{0.6}\text{Sr}_{0.4}\text{CoO}_{3-\delta}$  (60LSC) [32, 33], and  $\text{Sm}_{0.5}\text{Sr}_{0.5}\text{CoO}_{3-\delta}$  (50SSC) [34, 35]. If not from this study, data of exchange rate and/or partial conductivity were taken from literature studies.



## 6.3.4 Two-step exchange mechanism

Fig. 6.1 displays the isotope fractions  $f_g^{32}$ ,  $f_g^{34}$ , and  $f_g^{36}$  in the effluent pulse as a function of temperature. To account for the extent of isotopic scrambling, referring to the distribution of  $^{18}\text{O}$  over gas phase  $\text{O}_2$  molecules in the effluent pulse at each temperature, the reversible oxygen exchange reaction is assumed to proceed via a consecutive two-step mechanism, as proposed earlier by Boukamp *et al.* [36]



It should be noted that each of both steps may still represent a grouping of specific elementary steps. Relevant for the interpretation of experimental data is, however, that isotopic randomization is assumed to take place only after dissociative adsorption of  $\text{O}_2$  molecules at the surface (1<sup>st</sup> step in (6.4)). During its residence time at the surface, the oxygen adatom,  $\text{O}_{\text{ad}}$ , may or may not be exchanged with lattice oxygen,  $\text{O}_{\text{lattice}}$ , before recombining with another oxygen adatom, and subsequent returning to the gas phase as an  $\text{O}_2$  molecule. Application of the quasi-steady-state-approximation yields that the overall exchange rate,  $\mathfrak{R}_0$ , can be broken down into

$$\frac{1}{\mathfrak{R}_0} = \frac{1}{\mathfrak{R}_a} + \frac{1}{\mathfrak{R}_i} \quad (6.5)$$

where  $\mathfrak{R}_a$  is the rate of homolytic dissociative adsorption of  $\text{O}_2$  molecules at the oxide surface, and  $\mathfrak{R}_i$  that of subsequent incorporation of the oxygen adatoms into the oxide lattice. In deriving Eq. (6.5), the occurrence of alternative

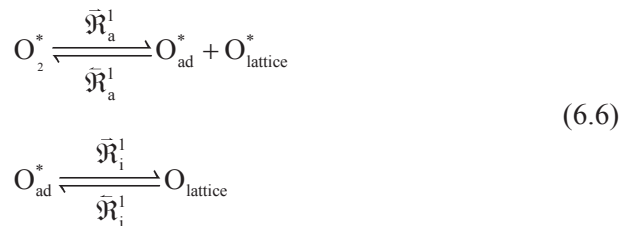
pathways for oxygen isotopic exchange has been excluded, such as (i) the mutual exchange of oxygen between O<sub>2</sub> molecules in the gas phase, and (ii) possible swapping out of one of the oxygen atoms of the O<sub>2</sub> molecule for another oxygen during hypothetical formation of a three-atom complex between a gas phase O<sub>2</sub> molecule and an adsorbed oxygen atom, O<sub>ad</sub>, or any other multi-atom complex between O<sub>2</sub> molecules and adsorbed species. For the full derivation of the equations, expressing the distribution of oxygen isotopomers <sup>18</sup>O<sub>2</sub>, <sup>16</sup>O<sup>18</sup>O, and <sup>16</sup>O<sub>2</sub> in the effluent gas phase pulse, we refer to the appendix of this chapter (Appendix 6.A). Two-step exchange scheme (6.4) was used to evaluate  $\mathfrak{R}_a$  and  $\mathfrak{R}_i$  from the measured oxygen isotope fractions (<sup>18</sup>O<sub>2</sub>, <sup>18</sup>O<sup>16</sup>O, and <sup>16</sup>O<sub>2</sub>) in the effluent pulse. Activation energies of both rates extracted from the corresponding Arrhenius plots for each of the compositions SrTi<sub>1-x</sub>Fe<sub>x</sub>O<sub>3-δ</sub> (not shown) are listed in Table 6.2. The Arrhenius expressions for both rates were used to calculate the drawn lines in Fig. 6.1.

Fig. 6.5 shows the  $pO_2$  dependencies of the surface exchange rate for STO, STF35, and STF50, respectively. Power law exponents obtained from least squares analysis of the experimental data are listed in Table 6.3. For all three compositions,  $\mathfrak{R}_0$  is found to vary with  $(pO_2)^n$  with  $n \approx 0.5$ . The two-step exchange model (scheme (6.4)) was used for calculation of  $\mathfrak{R}_a$  and  $\mathfrak{R}_i$ . Corresponding  $pO_2$  dependences of  $\mathfrak{R}_a$  and  $\mathfrak{R}_i$  calculated using two-step exchange scheme (6.4) are shown graphically in Fig. 6.6. The associated power law exponents are listed in Table 6.3.

For both STF35 and STF50,  $\mathfrak{R}_a$  is found to decrease with decreasing  $pO_2$ . The corresponding power law exponents are found to be close to unity, which is expected for molecular O<sub>2</sub> dissociative adsorption as rate determining step. On the basis of a consecutive mechanism for oxygen exchange weak and, in view of the closeness in composition, similar dependences of  $\mathfrak{R}_i$  on  $pO_2$  are

expected for STF35 and STF50. The corresponding data points are, however, too widely scattered to confirm such behavior. The ionic conductivity of both materials remains almost constant within the experimental range of  $pO_2$  [11]. Hence, a correlation between ionic conductivity and surface exchange rate, as discussed in the previous section, will not be manifested in the  $pO_2$ -dependences of both  $\mathfrak{R}_a$  and  $\mathfrak{R}_i$ . An important corollary of the results is that the observed power law exponent of  $\sim 0.5$  for  $\mathfrak{R}_0$  is an apparent value and is actually determined by the relative rates of  $\mathfrak{R}_a$  and  $\mathfrak{R}_i$ . In the temperature range of 350–450 °C, and at the lowest values of  $pO_2$ , oxygen exchange is predominantly limited by  $\mathfrak{R}_a$ . At the highest values of  $pO_2$  covered by the experiments,  $\mathfrak{R}_a$  and  $\mathfrak{R}_i$  are competing. A similar analysis could be presented for STO. Fig. 6.6 (a) shows evidence of a change-over of the rate determining step, at 900 °C, from exchange limited by  $\mathfrak{R}_a$  to one limited by  $\mathfrak{R}_i$  below  $pO_2 \approx 0.1$  atm. Given the large uncertainties in  $\mathfrak{R}_a$  and  $\mathfrak{R}_i$  for STO, the graph (Fig. 6.6) must be viewed as provisional, and treated with some caution. More measurements are necessary to provide support for the change in rate determining step for this composition.

Although the validity of scheme (6.4) has been verified by numerous isotopic exchange experiments in our laboratory, it should be mentioned that it is not the only possible two-step scheme to account for isotopic scrambling during the oxygen exchange reaction. An alternative two-step scheme is



where the superscript ‘1’ in both rates  $\mathfrak{R}_a^1$  and  $\mathfrak{R}_i^1$  designates the fact that in this scheme *one* oxygen atom of the O<sub>2</sub> molecule is immediately incorporated upon oxygen dissociative adsorption; the other, O<sub>ad</sub>, diffuses across the surface until it is either incorporated or, after recombination with lattice oxygen, returned to the gas phase as an O<sub>2</sub> molecule. The immediate incorporation of one of the oxygen atoms of an O<sub>2</sub> molecule upon adsorption affects the statistics of isotopic equilibration. For a full discussion and description of the mathematics, we refer the reader to the appendix of this chapter (Appendix 6.A). Application of scheme (6.6) to interpret the data from PIE measurements on STO, STF35, and STF50 as a function of  $pO_2$ , however, did not alter the major conclusions drawn from the previous analysis using scheme (6.4), as discussed above. Graphs showing the  $pO_2$  dependencies of  $\mathfrak{R}_a^1$  and  $\mathfrak{R}_i^1$  for these compositions, and a table listing the corresponding power law exponents obtained from least squares analysis of the experimental data are provided in Appendix 6.B. It should be noted that schemes (6.4) and (6.6) are the only two possible two-step schemes to account for isotopic scrambling during oxygen isotopic equilibration reaction with the oxide. Their relationships with the theories put forward by Boreskov and Muzykantov [37] and Klier *et al.* [38, 39] are discussed in the appendix (Appendix 6.A). Time-dependent oxygen isotopic equilibration measurements are proposed for evaluation which of both schemes better reflects the actual kinetics of oxygen surface exchange on SrTi<sub>1-x</sub>Fe<sub>x</sub>O<sub>3-δ</sub>.

**Table 6.3** Power law exponents of the  $p\text{O}_2$  dependencies of the rates of oxygen surface exchange ( $\mathfrak{R}_0$ ), oxygen dissociative adsorption ( $\mathfrak{R}_a$ ), and oxygen incorporation ( $\mathfrak{R}_i$ ) for STO, STF35, and STF50 at different temperatures. Values for  $\mathfrak{R}_a$  and  $\mathfrak{R}_i$  were calculated on the basis of two-step exchange scheme (6.4) for modeling the data from PIE measurements. Standard errors are given in parentheses and refer to the least significant decimals.

	$T$ (°C)	$\mathfrak{R}_0$	$\mathfrak{R}_a$	$\mathfrak{R}_i$
STO	900	0.46 (4)	1.8 (4)	-0.17 (20)
STF35	350	0.58 (7)	1.2 (1)	-0.31 (3)
	400	0.57 (3)	1.1 (1)	-0.41 (5)
STF50	400	0.59 (7)	0.82 (7)	0.10 (12)
	450	0.59 (7)	0.94 (9)	-0.10 (13)

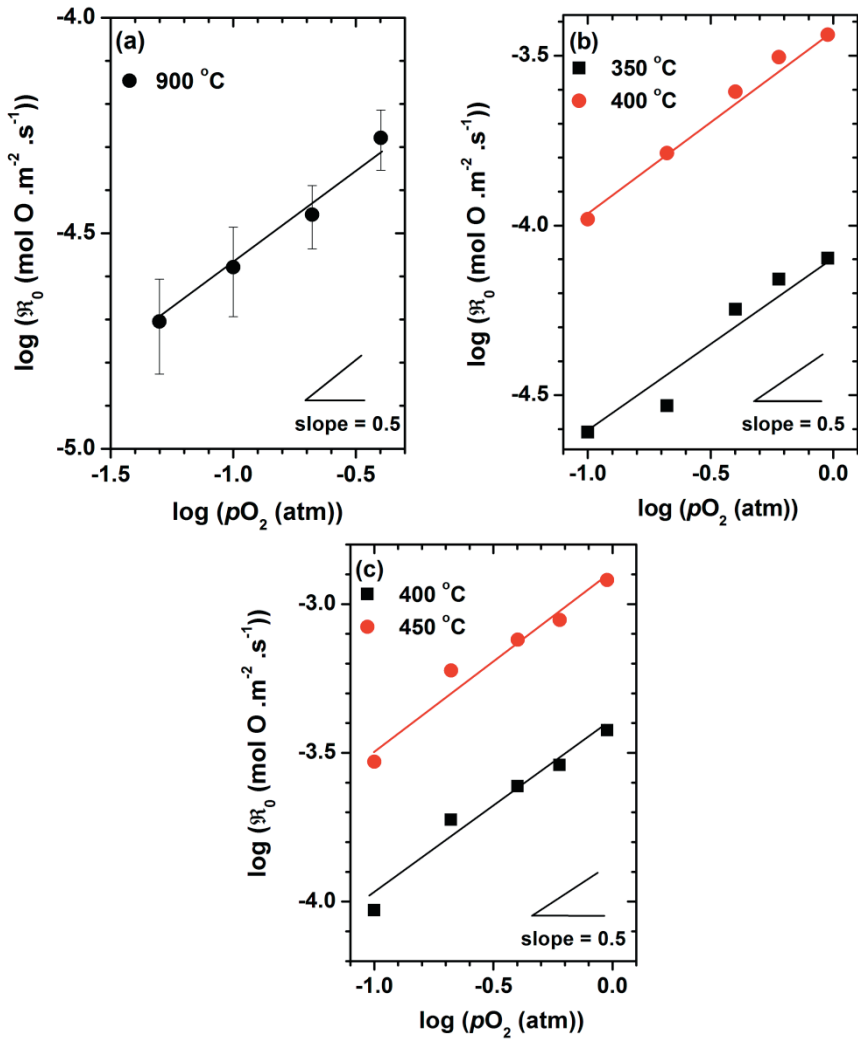


**Figure 6.5** Oxygen partial pressure dependence of the overall oxygen exchange rate,  $\mathfrak{R}_0$ , for selected  $\text{SrTi}_{1-x}\text{Fe}_x\text{O}_{3-\delta}$  compositions: (a) STO, (b) STF35, and (c) STF50.

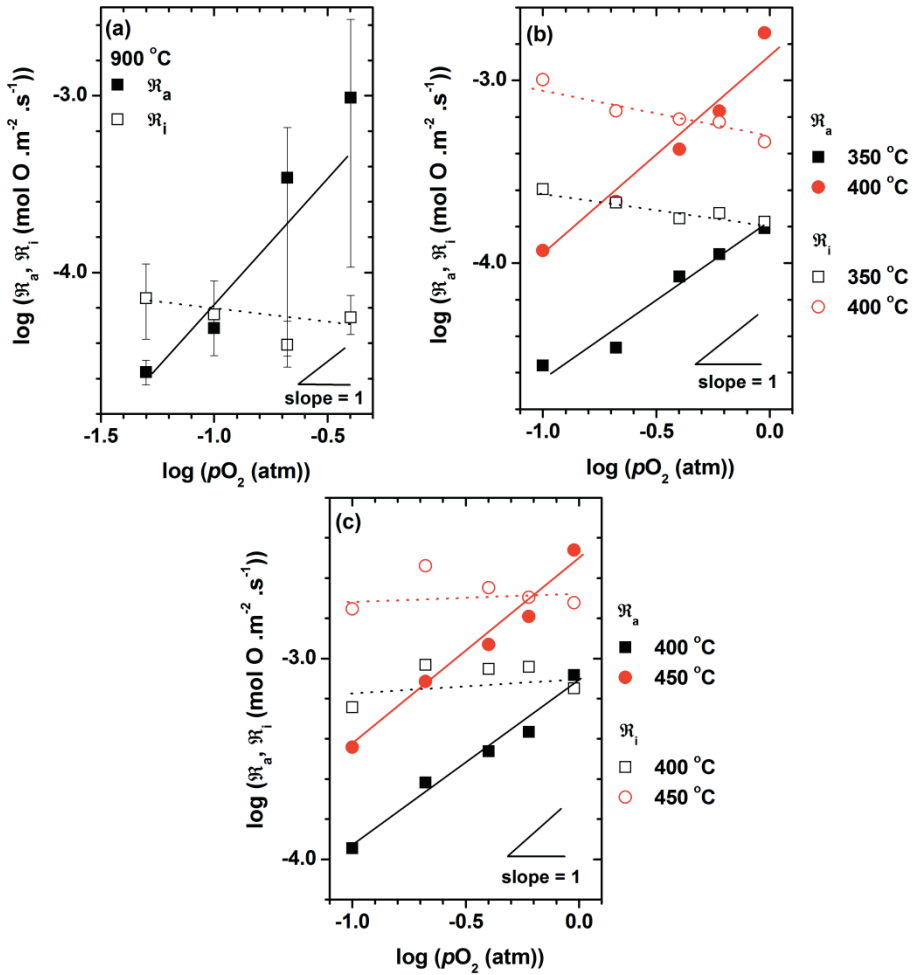


**Figure 6.6** Oxygen partial pressure dependence of the rates of oxygen dissociative adsorption ( $R_a$ ) and oxygen incorporation ( $R_i$ ) for selected  $\text{SrTi}_{1-x}\text{Fe}_x\text{O}_{3-\delta}$  compositions: (a) STO, (b) STF35, and (c) STF50. Calculations were performed on the basis of two-step exchange scheme (6.4) for modeling the data from PIE measurements. See main text.

## 6.4 Conclusions

The key results from this study can be summarized as follows:

- (1) The pulse isotopic exchange technique has been used in order to measure the rate of oxygen surface exchange,  $\mathfrak{R}_0$ , on mixed conducting perovskite oxides  $\text{SrTi}_{1-x}\text{Fe}_x\text{O}_{3-\delta}$  ( $x = 0, 0.01, 0.05, 0.35, 0.5$ ) as a function of temperature and oxygen partial pressure. Arrhenius activation energies range from  $140 \text{ kJ mol}^{-1}$  for  $x = 0$  to  $86 \text{ kJ mol}^{-1}$  for  $x = 0.5$ .
- (2) Extrapolating the temperature dependence of  $\mathfrak{R}_0$  to the intermediate temperature range,  $500\text{-}600 \text{ }^\circ\text{C}$ , indicates that  $\mathfrak{R}_0$ , in air, increases with increasing iron mole fraction in  $\text{SrTi}_{1-x}\text{Fe}_x\text{O}_{3-\delta}$ , but saturates at the highest iron mole fraction.
- (3) A linear relationship is observed in the log-log plot between  $\mathfrak{R}_0$  and oxide ionic conductivity, at  $600 \text{ }^\circ\text{C}$  in air, with slope  $\sim 1.2$ . This result suggests that it is the materials' oxide ionic conductivity that controls the rate of oxygen surface exchange. The observed relationship holds when selected literature data for other perovskite-type oxides are added.
- (4) A two-step exchange mechanisms for the isotopic exchange reaction is used to account for the distribution of  $^{16}\text{O}_2$ ,  $^{16}\text{O}^{18}\text{O}$ , and  $^{18}\text{O}_2$  in the effluent pulse. Accordingly, the power law dependence of  $\mathfrak{R}_0$  on  $p\text{O}_2$  is demonstrated to be an apparent one, depending on the relative rates of both steps involved in the adopted two-step scheme. Supplementary research is, however, required to elucidate which of the two proposed reaction schemes better reflects the actual kinetics of oxygen surface exchange reaction on  $\text{SrTi}_{1-x}\text{Fe}_x\text{O}_{3-\delta}$ .



## **Acknowledgement**

Dr. Avner Rothschild (Technion, Israel) is gratefully acknowledged for providing STO, STF35, and STF50 powders.

## References

1. A. Rothschild, S.J. Litzelman, H.L. Tuller, W. Menesklou, T. Schneider, E. Ivers-Tiffée, *Sensor Actuat. B-chem* 108 (2005) 223.
2. K. Sahner, R. Moos, M. Matam, J.J. Tunney, M. Post, *Sensor Actuat. B-chem* 108 (2005) 102.
3. W. Menesklou, H.J. Schreiner, K.H. Hardtl, E. Ivers-Tiffée, *Sensor Actuat. B-chem* 59 (1999) 184.
4. S. Molin, W. Lewandowska-Iwaniak, B. Kusz, M. Gazda, P. Jasinski, *J. Electroceram.* 28 (2012) 80.
5. J.R. Jurado, F.M. Figueiredo, B. Gharbage, J.R. Frade, *Solid State Ionics* 118 (1999) 89.
6. G.M. Choi, H.L. Tuller, *J. Am. Ceram. Soc.* 71 (1988) 201.
7. G.M. Choi, H.L. Tuller, D. Goldschmidt, *Phys. Rev. B* 34 (1986) 6972.
8. M.V. Patrakeev, I.A. Leonidov, V.L. Kozhevnikov, V. Kharton, *Solid State Sci.* 6 (2004) 907.
9. J. Mizusaki, M. Okayasu, S. Yamauchi, K. Fueki, *J. Solid State Chem.* 99 (1992) 166.
10. S. Steinsvik, R. Bugge, J. Gjønnes, J. Taftø, T. Norby, *J. Phys. Chem. Solids* 58 (1997) 969.
11. A. Rothschild, W. Menesklou, H.L. Tuller, E. Ivers-Tiffée, *Chem. Mater.* 18 (2006) 3651.
12. W. Jung, H.L. Tuller, *J. Electrochem. Soc.* 155 (2008) B1194.
13. W. Jung, H.L. Tuller, *Solid State Ionics* 180 (2009) 843.
14. W. Jung, H.L. Tuller, *Adv. Energy Mater.* 1 (2011) 1184.
15. F.S. Baumann, J. Fleig, G. Cristiani, B. Stuhlhofer, H.U. Habermeier, J. Maier, *J. Electrochem. Soc.* 154 (2007) B931.
16. H.J.M. Bouwmeester, C. Song, J. Zhu, J. Yi, M. van Sint Annaland, B.A. Boukamp, *Phys. Chem. Chem. Phys.* 11 (2009) 9640.
17. C.-Y. Yoo, B.A. Boukamp, H.J.M. Bouwmeester, *J. Solid State Electrochem.* 15 (2011) 231.
18. J. Rodríguez-Carvajal, *Commission on Powder Diffraction* 26 (2001) 12.
19. L.H. Brixner, *Mater. Res. Bull.* 3 (1968) 299.
20. R.D. Shannon, *Acta Crystallogr. A* 32 (1976) 751.
21. M. Leonhardt, R.A. De Souza, J. Claus, J. Maier, *J. Electrochem. Soc.* 149 (2002) J19.
22. S.F. Wagner, C. Warnke, W. Menesklou, C. Argiris, T. Damjanovic, G. Borchardt, E. Ivers-Tiffée, *Solid State Ionics* 177 (2006) 1607.

23. B.A. Boukamp, H.J.M. Bouwmeester, A.J. Burggraaf, Proceedings of the 2nd International Symposium on Ionic and Mixed Conducting Ceramics, ed. T.A. Ramanarayanan, W.L. Worrell and H.L. Tuller, ECS Proc, PV 94-12 (1994) 174.
24. L. Wang, R. Merkle, J. Maier, J. Electrochem. Soc. 157 (2010) B1802.
25. R.A. De Souza, J.A. Kilner, Solid State Ionics 126 (1999) 153.
26. R.A. De Souza, Phys. Chem. Chem. Phys. 8 (2006) 890.
27. U. Balachandran, N.G. Eror, J. Solid State Chem. 39 (1981) 351.
28. E. Bucher, A. Egger, P. Ried, W. Sitte, P. Holtappels, Solid State Ionics 179 (2008) 1032.
29. D.D. Edwards, J.I. Jung, S.T. Misture, J. Electroceram. 24 (2010) 261.
30. H. Ullmann, N. Trofimenko, F. Tietz, D. Stover, A. Ahmad-Khanlou, Solid State Ionics 138 (2000) 79.
31. J. Kilner, A. Esquirol, N. Brandon, Solid State Ionics 175 (2004) 63.
32. A. Egger, E. Bucher, W. Sitte, J. Electrochem. Soc. 158 (2011) B573.
33. A.V. Berenov, A. Atkinson, J.A. Kilner, E. Bucher, W. Sitte, Solid State Ionics 181 (2010) 819.
34. H.Y. Tu, Y. Takeda, N. Imanishi, O. Yamamoto, Solid State Ionics 100 (1997) 283.
35. I. Fullarton, J. Jacobs, H. van Benthem, J. Kilner, H. Brongersma, P. Scanlon, B. Steele, Ionics 1 (1995) 51.
36. B.A. Boukamp, B.A. van Hassel, I.C. Vinke, K.J. de Vries, A.J. Burggraaf, Electrochim. Acta 38 (1993) 1817.
37. G. Borskov, V. Muzykantov, Ann. Ny. Acad. Sci. 213 (1973) 137.
38. K. Klier, J. Nováková, P. Jíru, J. Catal. 2 (1963) 479.
39. K. Klier, E. Kucera, J. Phys. Chem. Solids 27 (1966) 1087.

## Appendix

### 6.A. Theory of oxygen isotopic exchange

In this appendix, the theory of oxygen isotopic exchange on solid oxides is presented. The equations provided are adapted to conditions encountered in the <sup>18</sup>O-<sup>16</sup>O pulse isotopic exchange (PIE) experiments, thereby following the more general treatment given earlier by den Otter *et al.*<sup>1</sup>

The PIE experiments are supposed to be carried out under isothermal and iso-*p*O<sub>2</sub> conditions, and under conditions that negligible accumulation of <sup>18</sup>O occurs at the oxide surface. The latter implies that the exchange time must be smaller than the time constant  $\tau = D^* / k_s^2$ , where  $D^*$  is the oxygen tracer diffusivity, and  $k_s$  the surface exchange coefficient. The latter is calculated from  $k_s = \mathfrak{R}_0 / c_o$ , where  $\mathfrak{R}_0$  is the rate of oxygen exchange, and  $c_o$  the concentration of oxide ions in the solid oxide. The time constant  $\tau$  dictates how fast <sup>18</sup>O piles up at the surface.<sup>2</sup> In the PIE experiments, the actual exchange time corresponds to the duration of a pulse. The number of <sup>18</sup>O atoms in the gas phase pulse is maintained substantially smaller than the number of oxide ions in the oxide, preventing significant accumulation of <sup>18</sup>O in the oxide.

The expectation values to find <sup>18</sup>O-labeled oxygen in the O<sub>2</sub> molecule after an exchange act are

$$\begin{aligned}\alpha_1 &= p_1 f_b^* + (1 - p_1) f_g^* \\ \alpha_2 &= p_2 f_b^* + (1 - p_2) f_g^*\end{aligned}\tag{6.A.1}$$

where  $p_1$  and  $p_2$  designate the probabilities of both atoms for exchange with lattice oxygen, and  $f_g^*$  and  $f_b^*$  are the <sup>18</sup>O-fractions in the gas phase and oxide,

---

<sup>1</sup> M.W. den Otter, B.A. Boukamp, H.J.M. Bouwmeester, *Solid State Ionics* 139 (2001) 89.

<sup>2</sup> P. Fielitz, G. Borchardt, *Solid State Ionics* 144 (2001) 71.

respectively. The differential equations describing the time dependence of  $x$ ,  $y$ , and  $z$ , denoting the gas phase fractions of  $^{36}\text{O}_2$ ,  $^{34}\text{O}_2$ , and  $^{32}\text{O}_2$ , respectively, in a volume element, traversing through the reactor can be written as

$$\begin{aligned} n \cdot \frac{\partial x}{\partial t} &= S \cdot \mathfrak{R}_a [-x + (\alpha_1 \cdot \alpha_2)] \\ n \cdot \frac{\partial y}{\partial t} &= S \cdot \mathfrak{R}_a [-y + (\alpha_1(1 - \alpha_2) + \alpha_2(1 - \alpha_1))] \\ n \cdot \frac{\partial z}{\partial t} &= S \cdot \mathfrak{R}_a [-z + ((1 - \alpha_1)(1 - \alpha_2))] \end{aligned} \quad (6.A.2)$$

where  $n$  (mol O) denotes the number of O atoms in the gas phase of a volume element (which is twice the number of  $\text{O}_2$  molecules),  $\mathfrak{R}_a$  (mol O  $\text{m}^{-2} \text{s}^{-1}$ ) the rate of adsorption, and  $S$  the oxide surface area. Quantities  $n$  and  $S$  are normalized over the entire volume of the reactor. Since in the PIE experiments,  $f_b^* \approx 0$ , Eq. (6.A.2) can be rewritten as

$$\begin{aligned} n \cdot \frac{\partial x}{\partial t} &= S \cdot \mathfrak{R}_a [-x + f_g^{*2} \cdot (1 - p_1)(1 - p_2)] \\ n \cdot \frac{\partial y}{\partial t} &= S \cdot \mathfrak{R}_a [-y + f_g^{*2} \cdot ((1 - p_1)p_2 + p_1(1 - p_2))] \\ n \cdot \frac{\partial z}{\partial t} &= S \cdot \mathfrak{R}_a [-z + f_g^{*2} \cdot (p_1 p_2)] \end{aligned} \quad (6.A.3)$$

The  $^{18}\text{O}$ -fraction in the gas phase can be calculated from

$$f_g^* = x + \frac{1}{2} y \quad (6.A.4)$$

Hence, its time dependence follows from the first order linear differential equation,

$$n \cdot \frac{\partial f_g^*}{\partial t} = -S \cdot \left( \frac{1}{2} (p_1 + p_2) \cdot \mathfrak{R}_a \right) \cdot f_g^* \quad (6.A.5)$$

which is in accord with McKay's law for isotopic exchange reactions.<sup>3</sup> Integration with respect to time yields

$$f_g^*(t) = f_{g,i}^* \cdot \exp\left(-\frac{t}{\tau_0}\right) \quad (6.A.6)$$

where

$$\tau_0 = \frac{n}{\mathfrak{R}_0 S} \quad (6.A.7)$$

Hence, the overall <sup>18</sup>O-<sup>16</sup>O exchange rate  $\mathfrak{R}_0$  is given by

$$\mathfrak{R}_0 = \frac{1}{2}(p_1 + p_2) \cdot \mathfrak{R}_a \quad (6.A.8)$$

Eq. (6.A.6) is equivalent to Eq. (6.1) for  $t = \tau_r$ , where  $\tau_r$  is the time of residence in the reactor.

So far the two oxygen atoms in the gaseous O<sub>2</sub> molecule are considered to have independent probabilities ( $p_1, p_2$ ) for exchange with lattice oxygen, *i.e.*, not determined by the pathway for oxygen exchange. In the isotopic exchange theory developed by Klier *et al.*,<sup>4</sup> and independently by Boreskov and Muzykantov,<sup>5</sup> the exchange is described by three parallel one-step mechanisms. In the theory developed by these authors, it is conceived that the O<sub>2</sub> molecule may exchange either one or both atoms with lattice oxygen (referred to as hetero exchange) at a rate  $R^1$  and  $R^2$ , respectively, or, without the involvement of lattice oxygen, *i.e.*, only with oxygen atoms from the gas phase (referred to as homo exchange), at a rate  $R^0$ . The stochastic theory developed by the above cited authors is mathematically consistent with the present theory. Its relation-

---

<sup>3</sup> H.A.C. McKay, Nature 142 (1938) 997.

<sup>4</sup> K. Klier, J. Nováková, P. Jíru, J. Catal. 2 (1963) 479.

<sup>5</sup> G. Boreskov, V. Muzykantov, Ann. Ny. Acad. Sci. 213 (1973) 137.

ship becomes more clear if we write the rates associated with each of the one-step mechanisms as

$$\begin{aligned} R^0 &= \mathfrak{R}_a [(1-p_1) \cdot (1-p_2)] \\ R^1 &= \mathfrak{R}_a [p_1(1-p_2) + (1-p_1)p_2] \\ R^2 &= \mathfrak{R}_a [p_1 p_2] \end{aligned} \tag{6.A.9}$$

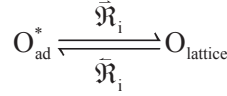
noting that

$$\mathfrak{R}_a = R^0 + R^1 + R^2 \tag{6.A.10}$$

When  $(p_1, p_2) = (0, 0)$ ,  $(p_1, p_2) = (1, 0)$  or  $(0, 1)$ , or  $(p_1, p_2) = (1, 1)$ , either mechanism  $R^0$ ,  $R^1$  or  $R^2$  occurs exclusively. When both  $p_1$  and  $p_2$  depart from 0 or 1, all three one-step mechanisms will occur simultaneously. The charm of the theory developed by den Otter *et al.*,<sup>1</sup> in which the parameter set  $(\mathfrak{R}_a, p_1, p_2)$  is used, rather than  $(R^0, R^1, R^2)$ , is that mechanistic models for the oxygen isotopic exchange are easily implemented.

In the following, we exclude *i*) mutual exchange of oxygen between  $O_2$  molecules in the gas phase, and *ii*) possible swapping out of one of the oxygen atoms of the  $O_2$  molecule for another oxygen during hypothetical formation of a three-atom complex between a gas phase  $O_2$  molecule and an adsorbed O adatom, or of any other multi-atom complex between  $O_2$  molecules and adsorbed species. Analysis of the mechanistic pathways, and associated statistics, shows that the exchange of oxygen between the gas phase and oxide can be described to proceed via two reversible two-step mechanisms, following dissociative adsorption of oxygen.

In the first of these mechanisms, both O-adatoms,  $O_{ad}$ , formed after homolytic dissociative adsorption of  $O_2$ , have equal probability (*i.e.*,  $p_1 = p_2 = p$ ) to be converted into lattice oxygen,



The incorporation of  $O_{ad}$  into the oxide lattice is bounded by rates  $\mathfrak{R}_a$  and  $\mathfrak{R}_i$ . It is easily verified that

$$\mathfrak{R}_0 = \mathfrak{R}_a \cdot p = \frac{\mathfrak{R}_a \mathfrak{R}_i}{\mathfrak{R}_a + \mathfrak{R}_i} \quad (6.A.11)$$

and, by substitution of  $p_1 = p_2 = p$  into Eq. (6.A.9),

$$\begin{aligned} R^0 &= \mathfrak{R}_a \cdot (1-p)^2 \\ R^1 &= \mathfrak{R}_a \cdot 2p(1-p) \\ R^2 &= \mathfrak{R}_a \cdot p^2 \end{aligned} \quad (6.A.12)$$

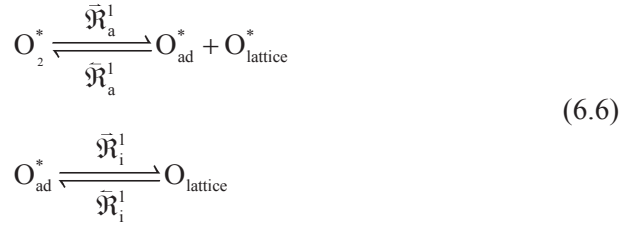
It follows that by adopting scheme (6.4) as the mechanism for isotopic exchange, the rates  $R_0$ ,  $R_1$ , and  $R_2$  are subject to constraint  $R^1 = \sqrt{4R^0 R^2}$ . Substitution of Eq. (6.A.6) in Eq. (6.A.3), followed by integration over the time of residence yields

$$x = \left( \frac{(1-p)}{(1-2p)^{\frac{1}{2}}} \cdot f_{g,i}^* \right)^2 \cdot \exp\left(-\frac{t}{\tau_0}\right) + \left( x_i - \left( \frac{(1-p)}{(1-2p)^{\frac{1}{2}}} \cdot f_{g,i}^* \right)^2 \right) \cdot \exp\left(-\frac{t}{p\tau_0}\right) \quad (6.A.13)$$

where  $x_i = x(0)$  denotes the fraction  $x$  in the inlet pulse. Eq. (6.A.13) can be used to calculate  $p$  from the value of  $x$  in the pulse at the exit of the reactor. Explicit expressions for  $y$  and  $z$  follow from the use of equations (6.A.4) and  $x + y + z = 1$ .



In the second of these mechanisms, one oxygen atom is immediately incorporated ( $p_1 = 1$ ) upon adsorption, the other is an oxygen adatom,  $O_{ad}$ , migrating over the surface until it either recombines with lattice oxygen and desorbs as an oxygen molecule or is incorporated (with probability  $p_2 = p'$ ) into the oxide lattice,



where the superscripts in  $\mathfrak{R}_a^1$  and  $\mathfrak{R}_i^1$  have been adapted (to designate that in this model one oxygen atom is immediately incorporated upon adsorption). It follows that

$$\mathfrak{R}_0 = \frac{1}{2} \mathfrak{R}_a^1 \cdot (1 + p') = \frac{1}{2} \mathfrak{R}_a^1 \cdot \left( 1 + \frac{\mathfrak{R}_i^1}{\frac{1}{2} \mathfrak{R}_a^1 + \mathfrak{R}_i^1} \right) \quad (6.A.14)$$

and, by substitution of  $p_1 = 1; p_2 = p$  into Eq. (6.A.9),

$$\begin{aligned} R^0 &= 0 \\ R^1 &= \mathfrak{R}_a^1 \cdot p' \\ R^2 &= \mathfrak{R}_a^1 \cdot (1 - p') \end{aligned} \quad (6.A.15)$$

Making the appropriate substitutions, one may derive from Eq. (6.A.3),

$$x = x_i \cdot \exp\left(-\frac{2}{(1 + p')} \cdot \frac{t}{\tau_0}\right) \quad (6.A.16)$$

which can be used to evaluate  $p'$  from the fraction  $x$  in the exit pulse. Both mechanisms (6.4) and (6.6) converge into a one-step  $R^2$ -mechanism if both

oxygen atoms in the  $\text{O}_2$  molecule have a probability of unity for incorporation into the oxide lattice. It is further noted that both steps in schemes (6.4) and (6.6) may involve a consecutive set of elementary reactions. Finally, it is stressed that PIE measurements alone cannot discriminate between the validity of two-step schemes (6.4) and (6.6). To this end, the isotopic equilibration between gas phase and oxide needs to be monitored as a function of time. Proper account needs to be taken in such experiments when the isotopic equilibration is partly governed by diffusion of  $^{18}\text{O}$  in the oxide.<sup>6</sup>

---

<sup>6</sup> K. Klier, E. Kucera, J. Phys. Chem. Solids 27 (1966) 1087.

## 6.B. Data for alternative two-step exchange mechanism

**Table 6.B.1** Power law exponents of the  $p\text{O}_2$  dependencies of the rates of oxygen dissociative adsorption ( $\mathfrak{R}_a^1$ ), and oxygen incorporation ( $\mathfrak{R}_i^1$ ) for STO, STF35, and STF50 at different temperatures. Values for  $\mathfrak{R}_a^1$  and  $\mathfrak{R}_i^1$  were calculated on the basis of two-step exchange scheme (6.6) for modeling the data from PIE measurements. Standard errors are given in parentheses and refer to the least significant decimals.

	$T$ ( $^{\circ}\text{C}$ )	$\mathfrak{R}_a^1$	$\mathfrak{R}_i^1$
STO	900	0.65 (8)	-
STF35	350	0.72 (9)	-0.29 (3)
	400	0.66 (6)	-0.84 (6)
STF50	400	0.8 (1)	0.1 (2)
	450	0.8 (1)	-0.2 (2)

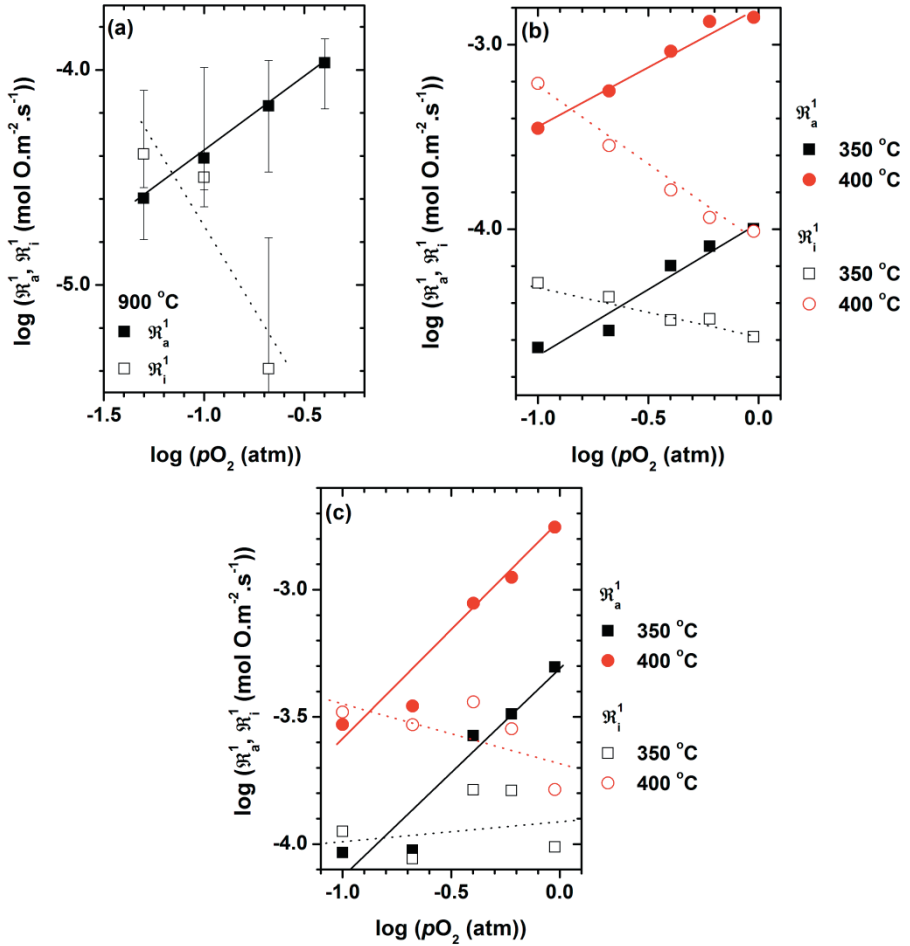


**Figure 6.B.1** Oxygen partial pressure dependence of the rates of oxygen dissociative adsorption ( $\mathcal{R}_a^1$ ) and oxygen incorporation ( $\mathcal{R}_i^1$ ) rate for selected  $\text{SrTi}_{1-x}\text{Fe}_x\text{O}_{3-\delta}$  compositions: (a) STO, (b) STF35, and (c) STF50. Calculations were performed on the basis of two-step exchange scheme (6.6) for modeling the data from PIE measurements. See main text.



---

## Chapter 7

# Oxygen surface exchange kinetics of 20 mol% rare-earth oxide-doped ceria

### Abstract

The oxygen exchange kinetics of 20 mol% rare-earth oxide-doped ceria,  $\text{RE}_{0.2}\text{Ce}_{0.8}\text{O}_{2-\delta}$  (RE = Gd, Sm, Pr, Tb), has been investigated using the pulse-response  $^{18}\text{O}$ - $^{16}\text{O}$  isotope exchange technique in the range of temperature 500-950 °C and oxygen partial pressure 0.1-0.95 atm. The results indicate that  $\text{Gd}_{0.2}\text{Ce}_{0.8}\text{O}_{2-\delta}$ ,  $\text{Sm}_{0.2}\text{Ce}_{0.8}\text{O}_{2-\delta}$ , and  $\text{Pr}_{0.2}\text{Ce}_{0.8}\text{O}_{2-\delta}$  exhibit comparable exchange rate, whereas  $\text{Tb}_{0.2}\text{Ce}_{0.8}\text{O}_{2-\delta}$  exhibits an exchange rate about an order of magnitude lower than the other compositions. The exchange rate of  $\text{RE}_{0.2}\text{Ce}_{0.8}\text{O}_{2-\delta}$  is found to be independent of ionic, electronic, and ambipolar conductivities. The dissociative adsorption of the oxygen molecule is the rate determining step of the oxygen exchange reaction on  $\text{RE}_{0.2}\text{Ce}_{0.8}\text{O}_{2-\delta}$ .

## 7.1 Introduction

Doped ceria are promising electrolytes for use in solid oxide fuel cells (SOFC) [1, 2]. These materials exhibit high ionic conductivity and a good chemical stability towards high performance cobalt-containing cathodes [3]. Among all rare earth oxide dopants, gadolinia- and samaria-doped ceria are found to exhibit the highest ionic conductivities [4]. The maximum ionic conductivities are found for  $\text{Gd}_{0.2}\text{Ce}_{0.8}\text{O}_{2-\delta}$  [5] and  $\text{Sm}_{0.2}\text{Ce}_{0.8}\text{O}_{2-\delta}$  [6]. Recent studies show that  $\text{Gd}_{0.1}\text{Ce}_{0.9}\text{O}_{2-\delta}$ ,  $\text{Pr}_{0.2}\text{Ce}_{0.8}\text{O}_{2-\delta}$ , and  $\text{Tb}_{0.2}\text{Ce}_{0.8}\text{O}_{2-\delta}$  have potential for use as an oxygen transport membrane [7-10]. The oxygen exchange kinetics is a crucial parameter for the performance of doped ceria as oxygen ion conducting membranes. However, the oxygen exchange kinetics of doped ceria has not been investigated systematically.

In this study, the oxygen exchange kinetics of 20 mol% rare-earth oxide-doped ceria,  $\text{RE}_{0.2}\text{Ce}_{0.8}\text{O}_{2-\delta}$  (RE = Gd, Sm, Pr, and Tb), is investigated using the pulse-response  $^{18}\text{O}$ - $^{16}\text{O}$  isotope exchange (PIE) technique [11, 12]. Also, an attempt is made to make a correlation between the exchange rate and conductivity of  $\text{RE}_{0.2}\text{Ce}_{0.8}\text{O}_{2-\delta}$ .

## 7.2 Experimental

### 7.2.1 Sample preparation and analysis

Powders of  $\text{Gd}_{0.1}\text{Ce}_{0.9}\text{O}_{2-\delta}$  (GDC10),  $\text{Gd}_{0.2}\text{Ce}_{0.8}\text{O}_{2-\delta}$  (GDC20),  $\text{Sm}_{0.1}\text{Ce}_{0.9}\text{O}_{2-\delta}$  (SDC10),  $\text{Sm}_{0.2}\text{Ce}_{0.8}\text{O}_{2-\delta}$  (SDC20),  $\text{Tb}_{0.1}\text{Ce}_{0.9}\text{O}_{2-\delta}$  (TDC10),  $\text{Tb}_{0.2}\text{Ce}_{0.8}\text{O}_{2-\delta}$  (TDC20), and  $\text{Pr}_{0.2}\text{Ce}_{0.8}\text{O}_{2-\delta}$  (PDC20) were prepared by a coprecipitation method using metal nitrate precursors. All powders were calcined in air at 950-1000 °C for 10 h. The obtained single phase powders were uniaxially pressed at 25 MPa into a pellet, followed by cold isostatic pressing at 400 MPa, and then sintered in air at 1400 °C for 10 h. The sintered pellets were crushed into coarse powders, sieved with a 120 mesh metal grid. The sieved

powders were annealed in air at 1200 °C for 10 h, and then sieved again with a 120 mesh metal grid to remove agglomerates. The phase purity was examined by X-ray diffraction (PANanalytical PW1830). The particle size and BET surface area measurements were conducted using a Mastersizer 2000 (Malvern Instruments) and a Gemini VII (Micromeritics), respectively.

### 7.2.2 Pulse-response $^{18}\text{O}$ - $^{16}\text{O}$ isotope exchange measurements

Pulse-response isotope exchange (PIE) measurements were performed in the range of temperature and oxygen partial pressure ( $p\text{O}_2$ ) 500-950 °C and 0.1-0.95 atm, respectively, using a continuous flow packed-bed micro-reactor. During the measurement, the sample powder was loaded in the center of the quartz tubular reactor with inner diameter 2 mm. Quartz wool plugs were used on both sides of the powder to secure the packed-bed. The length and mass of the packed-bed were typically in the range of 11-13 mm and 100-120 mg, respectively.  $^{16}\text{O}_2$  with Ar was used as carrier gas with a total flow rate of 50 ml  $\text{min}^{-1}$  (NTP). The response to a  $^{18}\text{O}_2/\text{N}_2$  pulse, with the same oxygen partial pressure as in the carrier gas, passing through the reactor was analyzed by on-line mass spectrometry (Omni Star TM GSD 301 Pfeiffer-Vacuum) at the exit of the reactor. A six-port valve with a 500  $\mu\text{l}$  sample loop was used for injection of the  $^{18}\text{O}_2/\text{N}_2$  pulse into the  $^{16}\text{O}_2/\text{Ar}$  gas flow stream. Oxygen isotope gas was purchased from Cambridge Isotope Laboratory (> 97 atom%  $^{18}\text{O}_2$ ). Nitrogen, used as diluent for the  $^{18}\text{O}_2$  gas was also used for internal calibration of the mass spectrometer. The mean residence time of the reactor varied between 10 and 30 ms, depending on temperature. The packed-bed was pre-treated at 850 °C in synthetic air to remove adsorbed water and  $\text{CO}_2$ , and cooled down to 50 °C before the measurement. The pulse isotopic exchange measurements were conducted from 50 °C onwards up to 950 °C. The packed-bed reactor was equilibrated for 0.5 h at each temperature and  $p\text{O}_2$  before the measurement.



Averaged values of three pulse experiments at a given temperature and  $pO_2$  were used for evaluating the surface exchange rate.

The overall surface exchange rate,  $\mathfrak{R}_0$  (mol O m<sup>-2</sup> s<sup>-1</sup>), is calculated from [11, 12]

$$\mathfrak{R}_0 = \frac{n}{\tau_r S} \ln \left( \frac{f_{g,i}^{18}}{f_{g,e}^{18}} \right) \quad (7.1)$$

where  $f_{g,i}^{18}$  and  $f_{g,e}^{18}$  are the <sup>18</sup>O isotope fractions in the pulse at the inlet and exit of the reactor, respectively,  $n$  is the total number of oxygen atoms in the free volume of the oxide packed bed,  $S$  the total surface area of the oxide powder, and  $\tau_r$  the average residence time of the labeled gas in the reactor.  $f_g^{18}$  is calculated from the measured pulse integral values of the isotope fractions with mass 36 and 34: ( $f_g^{18} = 0.5f_g^{34} + f_g^{36}$ ) at the exit of the reactor.  $\mathfrak{R}_0$  is a lumped parameter and can be broken down, assuming a two-step consecutive mechanism for the exchange reaction, into

$$\mathfrak{R}_0 = \frac{\mathfrak{R}_a \mathfrak{R}_i}{\mathfrak{R}_a + \mathfrak{R}_i} = p\mathfrak{R}_a \quad (7.2)$$

where  $\mathfrak{R}_a$  and  $\mathfrak{R}_i$  are the rates of oxygen dissociative adsorption and incorporation, respectively. The quantity  $p$  is calculated from

$$f_{g,e}^{36} = \left( \frac{(1-p)}{1-2p} \cdot f_{g,i}^{18} \right)^2 \cdot \exp\left(-\frac{2\tau_r}{\tau_u}\right) + \left( f_{g,i}^{36} - \left( \frac{(1-p)}{(1-2p)^{\frac{1}{2}}} \cdot f_{g,i}^{18} \right)^2 \right) \cdot \exp\left(-\frac{\tau_r}{p\tau_u}\right) \quad (7.3)$$

where  $\tau_u = n/\mathfrak{R}_0 S$ . Under the equilibrium conditions maintained during the isotope exchange experiments,  $p$  corresponds to the fraction of dissociatively adsorbed oxygen atoms that are successfully exchanged with oxygen from the

oxide. More details of the pulse isotope exchange experiments and theory are given elsewhere [11, 12].

### 7.3 Results and discussion

Fig. 7.1 shows the oxygen isotope fractions of (a) GDC20, (b) SDC20, (c) PDC20, and (d) TDC20 as a function of temperature in air. The oxygen exchange reaction is initiated at 500 °C for GDC20, SDC20, and PDC20 and at 700 °C for TDC20. Accordingly, the  $^{18}\text{O}_2$  fraction decreases with increasing temperature. The  $^{18}\text{O}$  in the gas phase is exchanged for  $^{16}\text{O}$  in the oxide, giving rise to the formation of  $^{18}\text{O}^{16}\text{O}$  and  $^{16}\text{O}_2$ . The  $^{18}\text{O}^{16}\text{O}$  fractions reach a maximum, 15% at 650 °C and 30% at 700 °C for GDC20 and SDC20, respectively, then decrease with increasing temperature, while both  $^{18}\text{O}^{16}\text{O}$  and  $^{16}\text{O}_2$  fractions of PDC20 and TDC20 increase with increasing temperature. The distribution of three oxygen isotopomers ( $^{18}\text{O}_2$ ,  $^{18}\text{O}^{16}\text{O}$ , and  $^{16}\text{O}_2$ ) allows to study the mechanism of the oxygen exchange reaction. This is further discussed below.

Fig. 7.2 shows Arrhenius plots of the overall exchange rate ( $\mathfrak{R}_0$ ) for GDC20, SDC20, PDC20, and TDC20 from PIE measurements. GDC20, SDC20, and PDC20 exhibit comparable exchange rate within a half order of magnitude, whereas TDC20 shows a much slower exchange rate of about an order of magnitude lower than GDC20, SDC20, and PDC20. Activation energies for GDC20, SDC20, PDC20, and TDC20 are 108 (3), 105 (3), 135 (5), and 137 (9)  $\text{kJ mol}^{-1}$ , respectively.

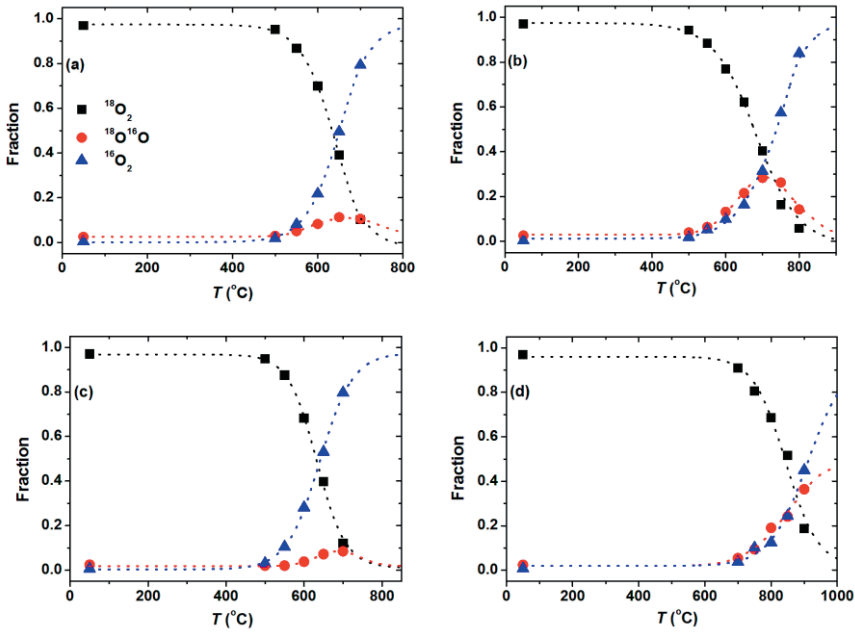


**Figure 7.1** Oxygen isotope fractions ( $^{18}\text{O}_2$ ,  $^{18}\text{O}^{16}\text{O}$ , and  $^{16}\text{O}_2$ ) as a function of temperature from PIE in synthetic air for (a)  $\text{Gd}_{0.2}\text{Ce}_{0.8}\text{O}_{2-\delta}$  (GDC20), (b)  $\text{Sm}_{0.2}\text{Ce}_{0.8}\text{O}_{2-\delta}$  (SDC20), (c)  $\text{Pr}_{0.2}\text{Ce}_{0.8}\text{O}_{2-\delta}$  (PDC20), and (d)  $\text{Tb}_{0.2}\text{Ce}_{0.8}\text{O}_{2-\delta}$  (TDC20). The drawn line is from model calculations, assuming constant activation energies for the dissociative adsorption and incorporation rate over the entire temperature range.

The oxygen exchange kinetics of gadolinia-doped ceria has been extensively studied by means of  $^{18}\text{O}$ - $^{16}\text{O}$  isotope exchange followed by depth profiling (IEDP) [13-16], while for other doped ceria compositions no exchange data are available in literature. Fig. 7.3 compares surface exchange rate data of GDC10 and GDC20 from PIE and  $^{18}\text{O}$ - $^{16}\text{O}$  isotope exchange followed by depth profiling (IEDP) measurements. To enable comparison, the surface exchange coefficient from IEDP measurements,  $k_s$  ( $\text{cm s}^{-1}$ ), was calculated using  $\mathfrak{R}_0 = k_s c_{\text{O}}$ , where  $c_{\text{O}}$  is the concentration of oxygen ions in the oxide. It is seen

from Fig. 7.3 that the surface exchange rate of gadolinia-doped ceria from literature and those obtained in this study significantly deviate. This may be partly accounted for by the different sample types (single crystal or polycrystalline) and oxygen partial pressures. Further systematic studies are necessary to clarify the observed discrepancies.

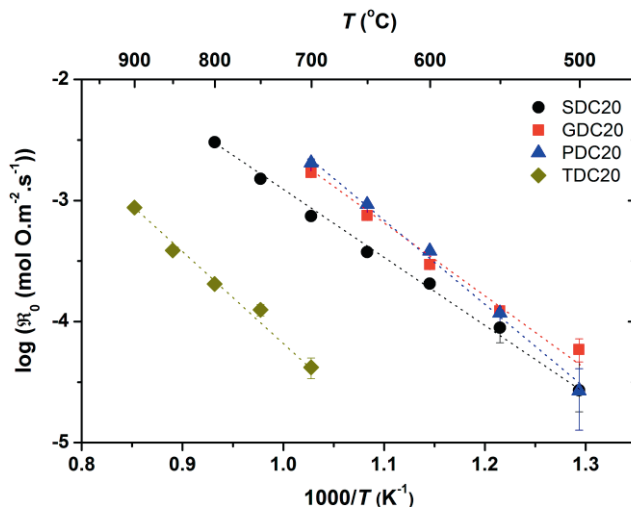


**Figure 7.2** Overall exchange rate ( $\mathfrak{R}_0$ ) of  $\text{Gd}_{0.2}\text{Ce}_{0.8}\text{O}_{2-\delta}$  (GDC20) and  $\text{Sm}_{0.2}\text{Ce}_{0.8}\text{O}_{2-\delta}$  (SDC20),  $\text{Pr}_{0.2}\text{Ce}_{0.8}\text{O}_{2-\delta}$  (PDC20), and  $\text{Tb}_{0.2}\text{Ce}_{0.8}\text{O}_{2-\delta}$  (TDC20) in air as a function of inverse temperature.

Recently, Wang *et al.* [17] have performed systematic study on perovskite-type oxides,  $\text{Ba}_{1-x}\text{Sr}_x\text{Co}_y\text{Fe}_{1-y}\text{O}_{3-\delta}$  using IEDP, and found that the surface exchange rate scales with the ionic conductivity, which emphasize that the surface oxygen exchange mechanism is strongly related to both the oxygen vacancy concentration and diffusivity. In this study, an attempt is made to correlate  $\mathfrak{R}_0$  with conductivities for doped ceria with varying doping element and concentration. Fig. 7.4 shows the log-log plot of (a) ionic, (b) electronic, and (c) ambipolar conductivities [4, 5, 18-21] vs.  $\mathfrak{R}_0$  at 600 °C in air. GDC10 and

SDC10 are excluded in Fig. 7.4 (b) and (c) due to lack of electrical and ambipolar conductivities in the literature. No apparent correlation is found between conductivities and  $\mathfrak{R}_0$  for doped ceria. Only a weak correlation as shown in Fig. 7.4 (a) between  $\mathfrak{R}_0$  and ionic conductivities is found for doped ceria except for PDC20. Although the ionic conductivity of PDC20 is about 1.5 orders of magnitudes lower than those of GDC20 and SDC20,  $\mathfrak{R}_0$  of PDC20 is nearly the same as that of GDC20 and SDC20, which is partly due to the excellent oxygen exchange activity of praseodymium oxide [22, 23]. In cases of gadolinia-, samaria-, and terbia-doped ceria,  $\mathfrak{R}_0$  increases with increasing dopant concentration from 10 to 20 mol%. Even though the thermodynamic and bulk transport properties of rare-earth oxide-doped ceria are well-understood, the relationship between surface oxygen exchange and bulk properties is still unclear.

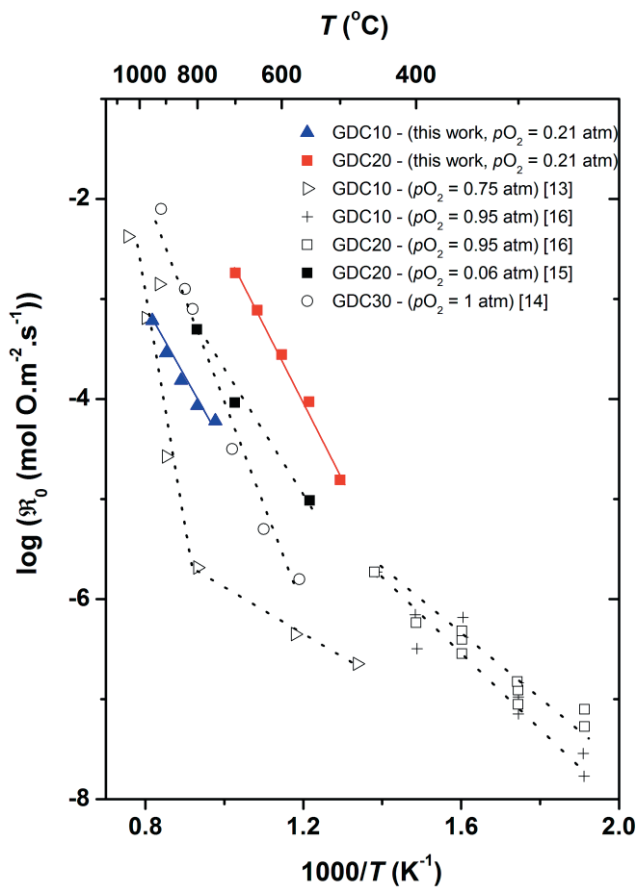


**Figure 7.3** The comparison of  $\mathfrak{R}_0$  of  $\text{Gd}_{0.1}\text{Ce}_{0.9}\text{O}_{2-\delta}$  (GDC10),  $\text{Gd}_{0.2}\text{Ce}_{0.8}\text{O}_{2-\delta}$  (GDC20), and  $\text{Gd}_{0.3}\text{Ce}_{0.7}\text{O}_{2-\delta}$  (GDC30) from pulse-response isotope exchange (PIE) and isotope exchange followed by depth profiling (IEDP) measurements [13-16].

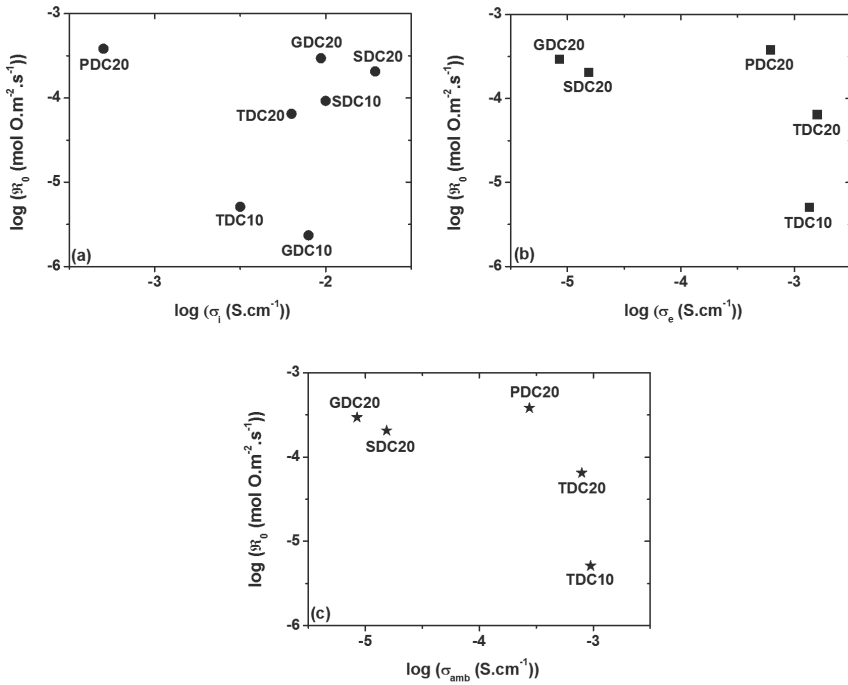


**Figure 7.4** Double-logarithmic plots of  $\mathfrak{R}_0$  vs. (a) ionic conductivity ( $\sigma_i$ ), (b) electronic conductivity ( $\sigma_e$ ), and (c) ambipolar conductivity ( $\sigma_{amb}$ ) for  $Gd_{0.1}Ce_{0.9}O_{2-\delta}$  (GDC10),  $Gd_{0.2}Ce_{0.8}O_{2-\delta}$  (GDC20),  $Sm_{0.1}Ce_{0.9}O_{2-\delta}$  (SDC10),  $Sm_{0.2}Ce_{0.8}O_{2-\delta}$  (SDC20),  $Tb_{0.1}Ce_{0.9}O_{2-\delta}$  (TDC10),  $Tb_{0.2}Ce_{0.8}O_{2-\delta}$  (TDC20), and  $Pr_{0.2}Ce_{0.8}O_{2-\delta}$  (PDC20) at 600 °C in air.

The dissociative adsorption ( $\mathfrak{R}_a$ ) and incorporation ( $\mathfrak{R}_i$ ) rates are calculated from Eqs. (7.2) and (7.3). Fig. 7.5 shows Arrhenius plots of  $\mathfrak{R}_0$ ,  $\mathfrak{R}_a$ , and  $\mathfrak{R}_i$  for (a) GDC20, (b) SDC20, (c) PDC20, and (d) TDC20. It is seen from Fig. 7.5 that the oxygen exchange rates of all compositions are limited by the rate of dissociated adsorption. Supplementary  $pO_2$  dependence measurements are performed for GDC20 and SDC20 to gain more insight in the underlying mechanism. Fig. 7.6 shows the  $pO_2$  dependence of  $\mathfrak{R}_0$ ,  $\mathfrak{R}_a$ , and  $\mathfrak{R}_i$  for (a) GDC20 and (b) SDC20 at 700 °C. It is remarkable that  $\mathfrak{R}_i$  of GDC20 is much higher than  $\mathfrak{R}_a$ , whereas  $\mathfrak{R}_i$  is comparable with  $\mathfrak{R}_a$  in the case of SDC20. Even though the bulk properties such as conductivity and defect chemistry of GDC20 and SDC20 are similar [4, 5, 18], observed  $pO_2$  dependencies of  $\mathfrak{R}_0$ ,  $\mathfrak{R}_a$ , and  $\mathfrak{R}_i$  are different each other. Hence, the difference in surface chemistry might provide an explanation for the observed discrepancies in the  $pO_2$  dependent measurements between GDC20 and SDC20. Scanlon *et al.* [24] observed by means of low energy ion scattering and Rutherford backscattering spectroscopy that the surface of GDC20 is highly enriched with gadolinium by about 250% (Ce/Gd ratio is 1 at the outermost surface) as compared to the bulk composition (Ce/Gd ratio is 4.2 in the bulk). Unfortunately, the surface chemistry of SDC20 is still unknown. More investigations are needed to clarify the relationship between surface chemistry and oxygen exchange kinetics for these doped ceria compositions.



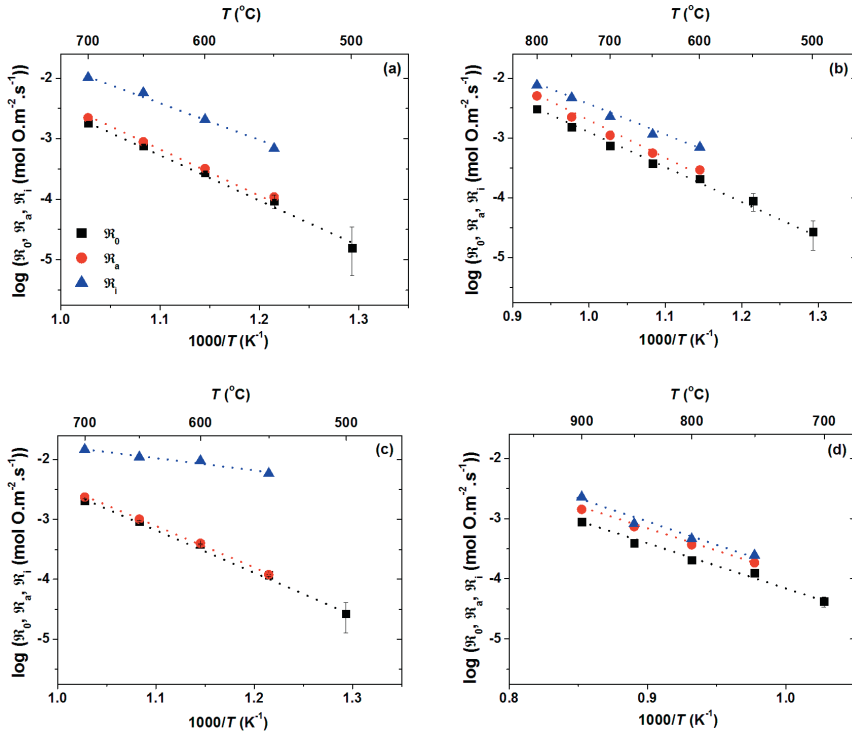


**Figure 7.5** Rate of overall oxygen exchange ( $\mathfrak{R}_0$ ), dissociative adsorption ( $\mathfrak{R}_a$ ), and oxygen incorporation ( $\mathfrak{R}_i$ ) of (a)  $\text{Gd}_{0.2}\text{Ce}_{0.8}\text{O}_{2-\delta}$  (GDC20), (b)  $\text{Sm}_{0.2}\text{Ce}_{0.8}\text{O}_{2-\delta}$  (SDC20), (c)  $\text{Pr}_{0.2}\text{Ce}_{0.8}\text{O}_{2-\delta}$  (PDC20), and (d)  $\text{Tb}_{0.2}\text{Ce}_{0.8}\text{O}_{2-\delta}$  (TDC20) in air as a function of inverse temperature.

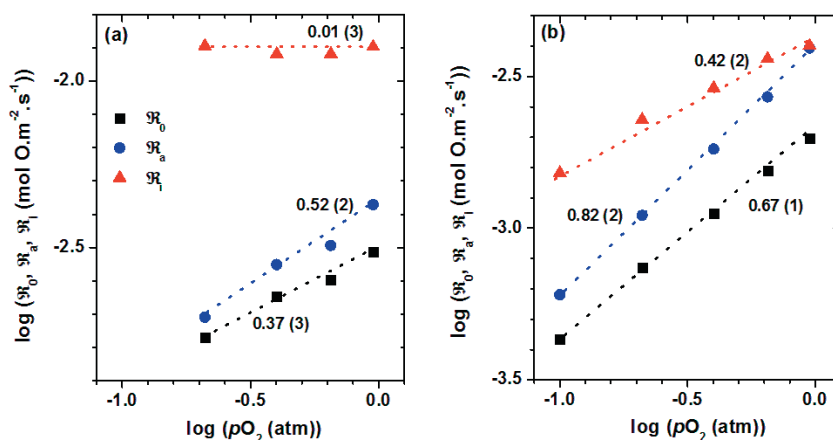


**Figure 7.6** Oxygen partial pressure dependence ( $p\text{O}_2$ ) of overall exchange rate ( $\mathfrak{R}_0$ ), dissociative adsorption ( $\mathfrak{R}_a$ ), and oxygen incorporation ( $\mathfrak{R}_i$ ) on (a)  $\text{Gd}_{0.2}\text{Ce}_{0.8}\text{O}_{2-\delta}$  (GDC20) and (b)  $\text{Sm}_{0.2}\text{Ce}_{0.8}\text{O}_{2-\delta}$  (SDC20) at 700 °C. The numbers denote the slope of each line.

## 7.4 Conclusions

The results obtained in this study show that  $\text{Gd}_{0.2}\text{Ce}_{0.8}\text{O}_{2-\delta}$ ,  $\text{Sm}_{0.2}\text{Ce}_{0.8}\text{O}_{2-\delta}$ , and  $\text{Pr}_{0.2}\text{Ce}_{0.8}\text{O}_{2-\delta}$  exhibit comparable exchange rate, while  $\text{Tb}_{0.2}\text{Ce}_{0.8}\text{O}_{2-\delta}$  exhibits an exchange rate of about an order of magnitude lower than the other compositions. No strong correlation between the exchange rate and bulk conductivity is found for  $\text{RE}_{0.2}\text{Ce}_{0.8}\text{O}_{2-\delta}$  (RE = Gd, Sm, Pr, and Tb). The surface oxygen exchange on  $\text{RE}_{0.2}\text{Ce}_{0.8}\text{O}_{2-\delta}$  is limited by the dissociative adsorption of oxygen.

## Acknowledgement

Tingfang Tian (University of Science and Technology of China, China) and María Balaguer (Universidad Politécnica de Valencia, Spain) are gratefully acknowledged for preparation of samples and PIE measurements.

## References

1. B.C.H. Steele, *Solid State Ionics* 129 (2000) 95.
2. S. Wang, T. Kato, S. Nagata, T. Kaneko, N. Iwashita, T. Honda, M. Dokiya, *Solid State Ionics* 152 (2002) 477.
3. A.J. Jacobson, *Chem. Mater.* 22 (2010) 660.
4. H. Yahiro, K. Eguchi, H. Arai, *Solid State Ionics* 36 (1989) 71.
5. Z. Tianshu, P. Hing, H. Huang, J. Kilner, *Solid State Ionics* 148 (2002) 567.
6. H. Yahiro, Y. Eguchi, K. Eguchi, H. Arai, *J. Appl. Electrochem.* 18 (1988) 527.
7. C. Chatzichristodoulou, M. Sogaard, J. Glasscock, A. Kaiser, S.P.V. Foghmoes, P.V. Hendriksen, *J. Electrochem. Soc.* 158 (2011) F73.
8. A. Kaiser, S. Foghmoes, C. Chatzichristodoulou, M. Sogaard, J. Glasscock, H.L. Frandsen, P.V. Hendriksen, *J. Membrane. Sci.* 378 (2010) 51.
9. M. Balaguer, C. Solís, J.M. Serra, *Chem. Mater.* 23 (2011) 2333.
10. D. Fagg, A. Shaula, V. Kharton, J. Frade, *J. Membrane. Sci.* 299 (2007) 1.
11. H.J.M. Bouwmeester, C. Song, J. Zhu, J. Yi, M. van Sint Annaland, B. A. Boukamp, *Phys. Chem. Chem. Phys.* 11 (2009) 9640.
12. C.-Y. Yoo, B.A. Boukamp, H.J.M. Bouwmeester, *J. Solid State Electrochem.* 15 (2011) 231.
13. J.A. Lane, J.A. Kilner, *Solid State Ionics* 136 (2000) 927.
14. E. Ruiz-Trejo, J.D. Sirman, Y.M. Baikov, J.A. Kilner, *Solid State Ionics* 113 (1998) 565.
15. N. Sakai, K. Yamaji, T. Horita, H. Kishimoto, Y.P. Xiong, H. Yokokawa, *Phys. Chem. Chem. Phys.* 5 (2003) 2253.
16. K. Kowalski, *Diffusion in Materials* 289-292 (2009) 769.
17. L. Wang, R. Merkle, J. Maier, *J. Electrochem. Soc.* 157 (2010) B1802.
18. K. Eguchi, T. Setoguchi, T. Inoue, H. Arai, *Solid State Ionics* 52 (1992) 165.
19. P. Shuk, M. Greenblatt, *Solid State Ionics* 116 (1999) 217.
20. P. Shuk, M. Greenblatt, M. Croft, *Chem. Mater.* 11 (1999) 473.
21. Y.P. Xiong, K. Yamaji, T. Horita, N. Sakai, H. Yokokawa, *J. Electrochem. Soc.* 151 (2004) A407.
22. V.N. Tikhonovich, V.V. Kharton, E.N. Naumovich, A.A. Savitsky, *Solid State Ionics* 106 (1998) 197.
23. A. Kovalevsky, C. Buysse, F. Snijkers, A. Buekenhoudt, J. Luyten, J. Kretzschmar, S. Lenaerts, *J. Memb. Sci.* 368 (2011) 223.

24. P.J. Scanlon, R.A.M. Bink, F.P.F. van Berkel, G.M. Christie, L.J. van IJzendoorn, H.H. Brongersma, R.G. van Welzenis, *Solid State Ionics* 112 (1998) 123.



---

## Chapter 8

# Oxygen surface exchange kinetics of $\text{La}_{1-x}\text{Sr}_x\text{CoO}_{3-\delta}$ ( $x = 0-0.7$ )

### Abstract

The oxygen exchange kinetics of  $\text{La}_{1-x}\text{Sr}_x\text{CoO}_{3-\delta}$  (LSC,  $x = 0, 0.2, 0.4, 0.5, 0.7$ ) has been investigated under synthetic air in the temperature range of 300-600 °C using the pulse-response  $^{18}\text{O}$ - $^{16}\text{O}$  isotope exchange technique.  $\text{LaCoO}_{3-\delta}$  and  $\text{La}_{0.8}\text{Sr}_{0.2}\text{CoO}_{3-\delta}$  are excluded in the discussion due to poor oxygen exchange capacity caused by  $^{18}\text{O}$  accumulation at the surface. The exchange rate of LSC increases with increasing strontium concentration. The activation energy of LSC is in the range of 112-114  $\text{kJ mol}^{-1}$ . The oxygen exchange mechanism on LSC is investigated employing a two-step model. The incorporation rate of adsorbed oxygen atoms is rate limiting for  $\text{La}_{0.6}\text{Sr}_{0.4}\text{CoO}_{3-\delta}$ , while the dissociative adsorption rate of oxygen molecules is rate limiting for  $\text{La}_{0.5}\text{Sr}_{0.5}\text{CoO}_{3-\delta}$  and  $\text{La}_{0.3}\text{Sr}_{0.7}\text{CoO}_{3-\delta}$ .

## 8.1 Introduction

Mixed ionic electronic conducting oxides, with compositions  $\text{La}_{1-x}\text{Sr}_x\text{CoO}_{3-\delta}$  (LSC), have been considered as cathode material for the solid oxide fuel cell (SOFC) [1-5]. The phase instability of LSC with zirconia based electrolytes can be overcome by using a ceria interlayer on top of the zirconia electrolyte [6-9]. A dense  $\text{La}_{0.6}\text{Sr}_{0.4}\text{CoO}_{3-\delta}$  thin film electrode exhibits low polarization resistance ( $< 0.1 \Omega \text{ cm}^{-2}$ ) even at 600 °C, which is attractive for the cathode in the intermediate temperature SOFC [10].

One of the crucial parameters for the polarization behavior of LSC electrode is the surface exchange rate, which can be determined by  $^{18}\text{O}$ - $^{16}\text{O}$  isotope exchange measurements. Oxygen isotope exchange measurements on LSC have been performed by many research groups using either *ex-situ*  $^{18}\text{O}$  depth profiling or line scanning after isotope exchange or *in-situ* gas phase analysis during isotope exchange at high temperatures [11-18]. Based on collected literature data and their own study, Berenov *et al.* [18] have found that the surface exchange coefficient of LSC increases with increasing strontium content. However, the surface exchange coefficients from literature are highly scattered which is partly due to the difference in sample type (single crystal or polycrystalline), sample density, temperature window, and oxygen partial pressure. The aim of this study is to provide better understanding of the oxygen exchange kinetics of LSC is through a systematic investigation using the pulse-response  $^{18}\text{O}$ - $^{16}\text{O}$  isotope exchange (PIE) technique [19, 20]. The effect of strontium concentration on the oxygen exchange kinetics will be discussed.

## 8.2 Experimental

### 8.2.1 Sample preparation and analysis

$\text{La}_{1-x}\text{Sr}_x\text{CoO}_{3-\delta}$  ( $x = 0, 0.2, 0.4, 0.5, \text{ and } 0.7$ ), abbreviated as LC, 80LSC, 60LSC, 50LSC, and 30LSC, powders were prepared by employing a glycine

nitrate process using metal nitrate precursors. All samples were calcined in air at 950-1000 °C for 10 h to obtain a pure phase. The 50LSC powder composition, prepared by spray pyrolysis, was directly obtained from Praxair Inc. (USA). The as calcined and received powders were uniaxially pressed at 25 MPa into a pellet, followed by cold isostatic pressing at 400 MPa, and then sintered at 1150 °C in air. The sintered pellets were crushed into coarse powders, sieved with a 120 mesh metal grid. The sieved powders were annealed in air at 950 °C for 10 h, and then sieved again with a 120 mesh metal grid to remove agglomerates. The phase purity was examined by X-ray diffraction (PANanalytical PW1830). The lattice parameters were obtained using FullProf program [21]. The particle size and BET surface area measurements were conducted using a Mastersizer 2000 (Malvern Instruments) and a Gemini VII (Micromeritics), respectively.

### 8.2.2 Pulse-response $^{18}\text{O}$ - $^{16}\text{O}$ isotope exchange measurements

Pulse-response isotope exchange (PIE) measurements were performed from 300 to 600 °C in synthetic air using a continuous flow packed-bed micro-reactor. During the measurement, the sample powder was loaded in the center of the quartz tubular reactor with inner diameter 2 mm. Quartz wool plugs were used on both sides of the powder to secure the packed-bed. The length and mass of the packed-bed were typically in the range of 8-10 mm and 30-60 mg, respectively.  $^{16}\text{O}_2$  with Ar was used as carrier gas and fed through the reactor with a total flow rate of 50 ml min<sup>-1</sup> (NTP). The response to a  $^{18}\text{O}_2/\text{N}_2$  pulse, with the same oxygen partial pressure, passing through the reactor was analyzed by on-line mass spectrometry (Omni Star TM GSD 301 Pfeiffer-Vacuum) at the exit of the reactor. A six-port valve with a 500 µl sample loop was used for injection of the  $^{18}\text{O}_2/\text{N}_2$  pulse into the  $^{16}\text{O}_2/\text{Ar}$  gas flow stream. Oxygen isotope gas was purchased from Cambridge Isotope Laboratory (> 97



atom%  $^{18}\text{O}_2$ ). Nitrogen, used as diluent for the  $^{18}\text{O}_2$  gas, was also used for internal calibration of the mass spectrometer. The mean residence time of the reactor varied between 10 and 30 ms, depending on temperature. The packed-bed was pre-treated at 850 °C in synthetic air to remove adsorbed water and  $\text{CO}_2$ , and cooled down to 50 °C before start of the measurement. After the pre-treatment, the measurements were performed in synthetic air as a function of temperature. The packed-bed reactor was equilibrated for 0.5 h at each temperature before the data acquisition. Averaged values of three pulse experiments at given temperature and  $p\text{O}_2$  were used for evaluating the surface exchange rate.

The overall surface exchange rate,  $\mathfrak{R}_0$  ( $\text{mol O m}^{-2} \text{ s}^{-1}$ ), is calculated from [19, 20]

$$\mathfrak{R}_0 = \frac{n}{\tau_r S} \ln \left( \frac{f_{g,i}^{18}}{f_{g,e}^{18}} \right) \quad (8.1)$$

where  $f_{g,i}^{18}$  and  $f_{g,e}^{18}$  are the  $^{18}\text{O}$  isotope fractions in the pulse at the inlet and exit of the reactor, respectively,  $n$  is the total number of oxygen atoms in the free volume of the oxide packed bed,  $S$  the total surface area of the oxide powder, and  $\tau_r$  the average residence time of the labeled gas in the reactor.  $f_g^{18}$  is calculated from the measured pulse integral values of the isotope fractions with mass 36 and 34: ( $f_g^{18} = 0.5f_g^{34} + f_g^{36}$ ) at the exit of the reactor.  $\mathfrak{R}_0$  is a lumped parameter and can be broken down, assuming a two-step consecutive mechanism for the exchange reaction, into

$$\mathfrak{R}_0 = \frac{\mathfrak{R}_a \mathfrak{R}_i}{\mathfrak{R}_a + \mathfrak{R}_i} = p\mathfrak{R}_a \quad (8.2)$$

where  $\mathfrak{R}_a$  and  $\mathfrak{R}_i$  are the rates of oxygen dissociative adsorption and incorporation, respectively. The quantity  $p$  is calculated from

$$f_{g,e}^{36} = \left( \frac{(1-p)}{1-2p} \cdot f_{g,i}^{18} \right)^2 \cdot \exp\left(-\frac{2\tau_r}{\tau_u}\right) + \left( f_{g,i}^{36} - \left( \frac{(1-p)}{(1-2p)^{\frac{1}{2}}} \cdot f_{g,i}^{18} \right)^2 \right) \cdot \exp\left(-\frac{\tau_r}{p\tau_u}\right) \quad (8.3)$$

where  $\tau_u = n / \mathfrak{R}_0 S$ . Under the equilibrium conditions maintained during the isotope exchange experiments,  $p$  corresponds to the fraction of dissociatively adsorbed oxygen atoms that are successfully exchanged with oxygen from the oxide. More details of the pulse isotope exchange experiments and theory are given elsewhere [19, 20].

### 8.3 Results and discussion

The X-ray diffraction patterns confirmed that all investigated LSC powders have a single-phase perovskite structure. Lattice parameters, particle size ( $d_{50}$ ), and BET area are summarized in Table 8.1. The lattice parameters agree well with values from literature [22].

Fig. 8.1 shows  $^{18}O_2$  and  $^{18}O^{16}O$  peaks measured for LC, 80LSC, 40LSC, 50LSC, and 30LSC. The  $^{18}O_2$  and  $^{18}O^{16}O$  peaks at 50 °C, as shown in Fig. 8.1 (a)-(b), are used to calculate the  $^{18}O$  fraction at the inlet of the reactor. The  $^{18}O_2$  peak decreases with increasing temperature due to the uptake of  $^{18}O$  by the oxide. The significant tailing of the  $^{18}O^{16}O$  peak is found for all LSC compounds at elevated temperatures, resulted from  $^{18}O^{16}O$  release by the oxide due to the recombination of exchanged  $^{18}O$  with  $^{16}O$  in the oxide. Due to this severe peak trailing, as shown in Fig 8.1 (a)-(b), integration of the  $^{18}O^{16}O$  peak area for LC and 80LSC becomes very inaccurate. Hence, it is not possible to evaluate the  $^{18}O$  uptake by LC and 80LSC. This observation indicates that only few  $^{16}O$  at the surface layers are available for the oxygen exchange due to the

poor oxygen exchange capacity of LC and 80LSC, which can be deduced from the short diffusion lengths of LC (~18 nm at 700 °C) [11] and 80LSC (~60 nm at 600 °C) [17] compared with their particle sizes. The diffusion length is estimated using  $\sqrt{6D^*t}$ , where  $D^*$  is the tracer diffusion coefficient and  $t$  the duration time of  $^{18}\text{O}_2$  pulse. LC and 80LSC are excluded from further discussion due to their poor oxygen exchange capacity. When the diffusion length is smaller than the particle size, exchanged  $^{18}\text{O}$  atoms will remain only in the layers close to the surface. Contrary to LC and 80LSC, much smaller  $^{18}\text{O}^{16}\text{O}$  signals are found for 60LSC, 50LSC, and 30LSC as shown in Fig. 8.1 (c). Particle sizes of 60LSC, 50LSC, and 30LSC are comparable with or smaller than their diffusion length (2-10  $\mu\text{m}$  at 600 °C) [16-18], hence, all  $^{16}\text{O}$  in the 60LSC, 50LSC, and 30LSC are available for the oxygen exchange reaction due to their sufficient oxygen exchange capacity.

**Table 8.1** Lattice parameters, median particle size ( $d_{50}$ ), and BET area of  $\text{La}_{1-x}\text{Sr}_x\text{CoO}_{3-\delta}$ .

Compound (preparation method)	Abbreviate	Lattice parameter (Å)	$d_{50}$ ( $\mu\text{m}$ )	BET area ( $\text{m}^2 \text{g}^{-1}$ )
$\text{LaCoO}_{3-\delta}$ (GNP)	LC	a = 5.4650 (1) c = 13.111 (2)	2	0.367 (1)
$\text{La}_{0.8}\text{Sr}_{0.2}\text{CoO}_{3-\delta}$ (GNP)	80LSC	a = 5.4347 (9) c = 13.164 (2)	3	0.621 (3)
$\text{La}_{0.6}\text{Sr}_{0.4}\text{CoO}_{3-\delta}$ (GNP)	60LSC	a = 5.4241 (8) c = 13.195 (5)	2	0.572 (2)
$\text{La}_{0.5}\text{Sr}_{0.5}\text{CoO}_{3-\delta}$ (SP)	50LSC	a = 5.4268 (8) c = 13.237 (3)	2	0.626 (15)
$\text{La}_{0.3}\text{Sr}_{0.7}\text{CoO}_{3-\delta}$ (GNP)	30LSC	a = 3.8352 (7)	3	0.289 (4)
$\text{La}_{0.3}\text{Sr}_{0.7}\text{CoO}_{3-\delta}$ (GNP, as calcined)			0.7	0.886 (11)

Preparation method: Glycine nitrate process (GNP) and spray pyrolysis (SP).

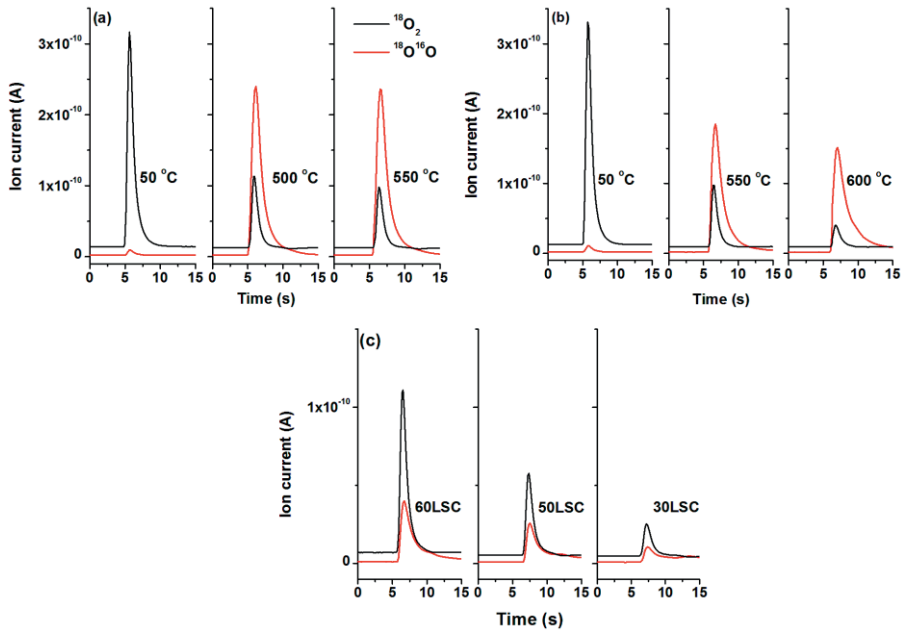


**Figure 8.1** Mass spectroscopic data for (a) LC, (b) 80LSC, and (c) 60LSC, 50LSC, and 30LSC at 400 °C from pulse-response isotopic exchange measurements.

Experimental data from PIE measurements in air for oxygen isotope fractions of 40LSC, 50LSC, and 30LSC are shown in Fig. 8.2 as a function of temperature. The  $^{18}O$  in the gas phase is exchanged for  $^{16}O$  in the oxide, giving rise to the formation of  $^{18}O^{16}O$  and  $^{16}O_2$ . The  $^{18}O^{16}O$  fractions reach a maximum, 49% at 450 °C, 30% at 425 °C, and 10% at 375 °C for 40LSC, 50LSC, and 30LSC, respectively, decreasing with increasing temperature thereafter. The  $^{18}O^{16}O$  formation is more relevant at lower strontium concentrations. The distribution of three oxygen isotopomers ( $^{18}O_2$ ,  $^{18}O^{16}O$ , and  $^{16}O_2$ ) allows to study the mechanism of the oxygen exchange reaction. This is further discussed below.

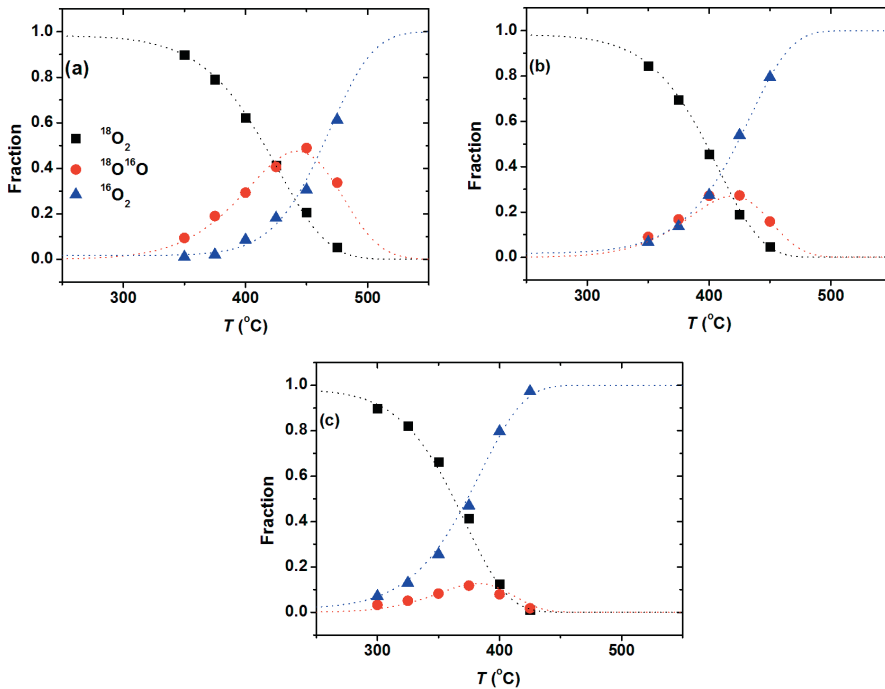


**Figure 8.2** Oxygen isotope fractions ( $^{18}\text{O}_2$ ,  $^{18}\text{O}^{16}\text{O}$ , and  $^{16}\text{O}_2$ ) as a function of temperature from PIE measurements in synthetic air for (a) 60LSC, (b) 50LSC, and (c) 30LSC. The drawn line is from model calculations, assuming constant activation energies for the dissociative adsorption and incorporation rate over the entire temperature range.

Fig. 8.3 show Arrhenius plots of the exchange rate ( $\mathfrak{R}_0$ ) for 80LSC, 40LSC, 50LSC, and 30LSC from PIE measurements. The  $\mathfrak{R}_0$  of LSC increases with increasing strontium content in agreement with observation by Berenov *et al.* [18]. In the temperature range of 350 to 400 °C, the oxygen nonstoichiometry ( $\delta$ ) of 50LSC and 30LSC is in the range of 0.04 to 0.07, in contrast to stoichiometric 60LSC ( $\delta \sim 0$ ) [2, 3, 22]. Hence, a possible explanation of the  $\mathfrak{R}_0$  enhancement with strontium is that it is due to an increase in the oxygen vacancy concentration. Activation energies for 60LSC, 50LSC, and 30LSC are

112 (5), 114 (1), and 114 (4)  $\text{kJ mol}^{-1}$ , respectively. The observed  $\mathfrak{R}_0$  of both calcined and crushed 30LSC powders are in good agreement.

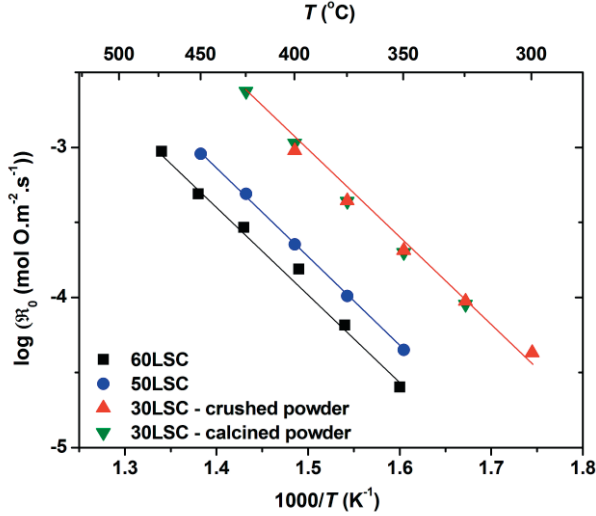


**Figure 8.3** Overall surface oxygen exchange rate ( $\mathfrak{R}_0$ ) for 60LSC, 50LSC, and 30LSC as a function of inverse temperature in synthetic air.

The dissociative adsorption ( $\mathfrak{R}_a$ ) and incorporation ( $\mathfrak{R}_i$ ) rates are calculated from Eqs. (8.2) and (8.3). Fig. 8.4 shows the overall exchange rate ( $\mathfrak{R}_0$ ), the rate of dissociated adsorption ( $\mathfrak{R}_a$ ), and incorporation ( $\mathfrak{R}_i$ ) of 60LSC, 50LSC, and 30LSC at 350 and 400 °C. The incorporation of adsorbed  $^{18}\text{O}$  atoms ( $\mathfrak{R}_i$ ) is the rate limiting step in the oxygen exchange reaction for 60LSC, whereas the dissociative adsorption ( $\mathfrak{R}_a$ ) is the rate determining step for 50LSC and 30LSC. As Fig. 8.2 shows, the formation of the  $^{18}\text{O}^{16}\text{O}$  fraction is significantly smaller for 50LSC and 30LSC than for 60LSC, which leads to the different rate determining steps. Ananyev *et al.* [23] have investigated the oxygen exchange kinetics on LSC with varying strontium content using *in-situ* gas phase analysis during  $^{18}\text{O}$ - $^{16}\text{O}$  isotope exchange at 700 °C. When the strontium content of

LSC increases, fractions of the first and third exchange type [24] decrease and increase, respectively, while that of second exchange type shows little variation. This observation supports the idea that, with increasing strontium content, the incorporation rate of dissociated oxygen atom is increasing faster than the dissociative adsorption rate of oxygen molecules, which is in agreement with this study.

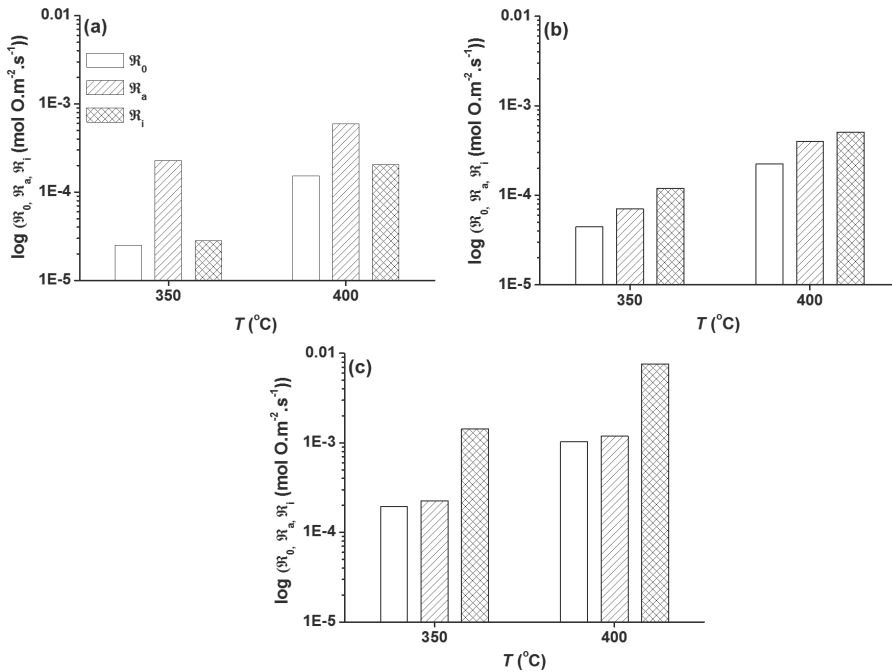


**Figure 8.4** The overall exchange ( $\mathfrak{R}_0$ ), dissociated adsorption ( $\mathfrak{R}_a$ ) and incorporation rate ( $\mathfrak{R}_i$ ) for (a) 60LSC, (b) 50LSC, and (c) 30LSC at 350 and 400 °C.

Fig. 8.5 shows the comparison of  $\mathfrak{R}_0$  between PIE and data collected from literature for 60LSC, 50LSC, and 30LSC. The surface exchange coefficient,  $k_s$  (cm s<sup>-1</sup>), was calculated using  $\mathfrak{R}_0 = k_s c_O$  equation, where  $c_O$  is the concentration of oxygen ions in the oxide. The data obtained for 50LSC show reasonable

agreement, whereas the  $\mathfrak{R}_0$  for 60LSC and 30LSC exhibit activation energies from PIE measurements that differ significantly from literature values.

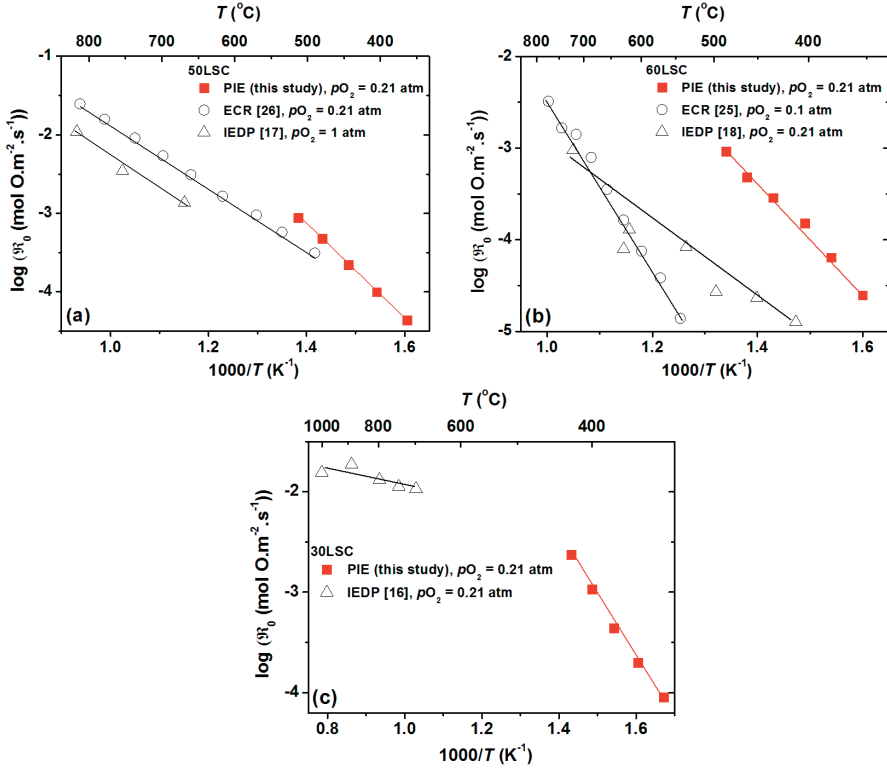


**Figure 8.5** Comparison of the oxygen surface exchange rate,  $\mathfrak{R}_0$ , for (a) 50LSC, (b) 60LSC, and (c) 30LSC obtained by pulse isotopic exchange measurements (PIE) with those from previous studies on dense ceramic samples using isotopic exchange followed by depth profiling (IEDP) [16-18] and electrical conductivity relaxation (ECR) [25, 26].

The  $\mathfrak{R}_0$  show also values that are about 1-2 orders of magnitude higher than data from isotope exchange, followed by depth profiling [16-18], and electrical conductivity relaxation [25, 26].  $\mathfrak{R}_0$  values obtained in this study and those from literature for 60LSC and 30LSC are differ largely. This could be associ-



ated with the difference in the sample preparation, surface composition, morphology, and measurement technique. Further investigation needs to be conducted to trace the origin of discrepancy.

#### 8.4 Conclusions

We have examined the exchange rate of  $\text{La}_{1-x}\text{Sr}_x\text{CoO}_{3-\delta}$  as a function of strontium content and temperature. The following facts are summarized.

1. The overall exchange rate of  $\text{La}_{1-x}\text{Sr}_x\text{CoO}_{3-\delta}$  ( $x = 0.4, 0.5, 0.7$ ) increases with strontium concentration, while the activation energies are almost identical.
2. Calcined and crushed  $\text{La}_{0.3}\text{Sr}_{0.7}\text{CoO}_{3-\delta}$  powders have comparable exchange rate.
3. The rate determining step for the oxygen exchange reaction on  $\text{La}_{0.6}\text{Sr}_{0.4}\text{CoO}_{3-\delta}$  is the incorporation of dissociated oxygen atoms, whereas for  $\text{La}_{0.5}\text{Sr}_{0.5}\text{CoO}_{3-\delta}$  and  $\text{La}_{0.3}\text{Sr}_{0.7}\text{CoO}_{3-\delta}$  it is the dissociative adsorption of oxygen molecules.

## References

1. J. Mizusaki, J. Tabuchi, T. Matsuura, S. Yamauchi, K. Fueki, *J. Electrochem. Soc.* 134 (1987) C473.
2. J. Mizusaki, Y. Mima, S. Yamauchi, K. Fueki, H. Tagawa, *J. Solid State Chem.* 80 (1989) 102.
3. J. Mizusaki, J. Tabuchi, T. Matsuura, S. Yamauchi, K. Fueki, *J. Electrochem. Soc.* 136 (1989) 2082.
4. C. Peters, A. Weber, E. Ivers-Tiffée, *J. Electrochem. Soc.* 155 (2008) B730.
5. J. Hayd, L. Dieterle, U. Guntow, D. Gerthsen, E. Ivers-Tiffée, *J. Power Sourc.* 196 (2011) 7263.
6. M. Backhaus-Ricoult, *Solid State Sci.* 10 (2008) 670.
7. S.B. Adler, *Chem. Rev.* 104 (2004) 4791.
8. A. Endo, H. Fukunaga, C. Wen, K. Yamada, *Solid State Ionics* 135 (2000) 353.
9. H. Uchida, S. Arisaka, M. Watanabe, *Electrochem. and Solid State Lett.* 2 (1999) 428.
10. J. Januschewsky, M. Ahrens, A. Opitz, F. Kubel, J. Fleig, *Adv. Func. Mater.* 19 (2009) 3151.
11. T. Ishigaki, S. Yamauchi, J. Mizusaki, K. Fueki, H. Tamura, *J. Solid State Chem.* 54 (1984) 100.
12. T. Ishigaki, S. Yamauchi, K. Kishio, J. Mizusaki, K. Fueki, *J. Solid State Chem.* 73 (1988) 179.
13. S. Carter, A. Selcuk, R.J. Chater, J. Kajda, J.A. Kilner, B.C.H. Steele, *Solid State Ionics* 53 (1992) 597.
14. J.L. Routbort, R. Doshi, M. Krumpelt, *Solid State Ionics* 90 (1996) 21.
15. A.N. Ezin, E.K. Kurumchin, I.V. Murygin, V.I. Tsidilkovski, G.K. Vdovin, *Solid State Ionics* 112 (1998) 117.
16. R.H.E. van Doorn, I.C. Fullerton, R.A. De Souza, J.A. Kilner, H.J.M. Bouwmeester, A.J. Burggraaf, *Solid State Ionics* 96 (1997) 1.
17. R.A. De Souza, J.A. Kilner, *Solid State Ionics* 126 (1999) 153.
18. A.V. Berenov, A. Atkinson, J.A. Kilner, E. Bucher, W. Sitte, *Solid State Ionics* 181 (2010) 819.
19. H.J.M. Bouwmeester, C. Song, J.J. Zhu, J.X. Yi, M. van Sint Annaland, B.A. Boukamp, *Phys. Chem. Chem. Phys.* 11 (2009) 9640.
20. C.-Y. Yoo, B.A. Boukamp, H.J.M. Bouwmeester, *J. Solid State Electrochem.* 15 (2011) 231.

## *Chapter 8*

---

21. J. Rodríguez-Carvajal, *Commission on Powder Diffraction* 26 (2001) 12.
22. R.H.E. van Doorn, A.J. Burggraaf, *Solid State Ionics* 128 (2000) 65.
23. M.V. Ananyev, N.M. Porotnikova, E.K. Kurumchin, 18th International Conference on Solid State Ionics (2011), P092.
24. G. Boreskov, V. Muzykantov, *Ann. Ny. Acad. Sci.* 213 (1973) 137.
25. A. Egger, E. Bucher, W. Sitte, *J. Electrochem. Soc.* 158 (2011) B573.
26. X. Chen, S. Wang, Y.L. Yang, L. Smith, N.J. Wu, B.I. Kim, S.S. Perry, A.J. Jacobson, A. Ignatiev, *Solid State Ionics* 146 (2002) 405.

---

## **Chapter 9**

### **Some recommendations for future research**

## 9.1 Introduction

This chapter provides some recommendations for further research based on the findings of this thesis.

## 9.2 Stability of alkaline-earth doped perovskite oxides in CO<sub>2</sub>-containing atmospheres

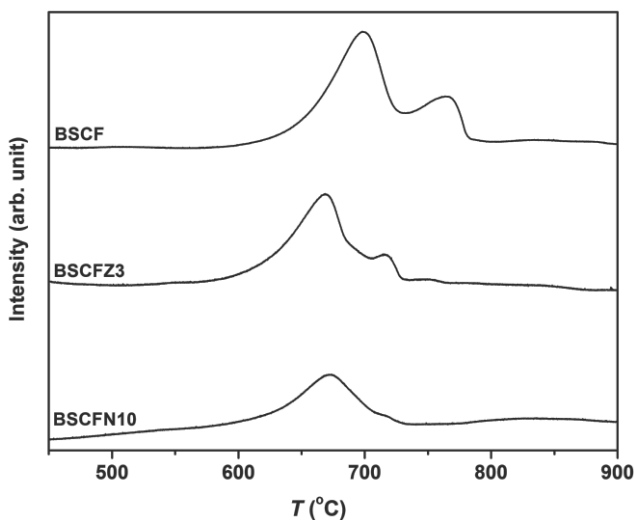


**Figure 9.1** CO<sub>2</sub>-temperature programmed desorption profiles of BSCF, BSCFZ3, and BSCFN10. Data are normalized to the total BET surface area of the powders.

Experimental studies on perovskite-type oxides Ba<sub>0.5</sub>Sr<sub>0.5</sub>Co<sub>0.8</sub>Fe<sub>0.2</sub>O<sub>3- $\delta$</sub>  (BSCF), 3 mol% Zr-substituted BSCF (BSCFZ3), and 10 mol% Nb-substituted BSCF (BSCFN10) were presented in Chapter 2 and 3 of this thesis. Fig. 9.1 shows corresponding temperature programmed desorption (TPD) profiles recorded after exposure to CO<sub>2</sub> at 700 °C for 2 h. As seen from this figure, for all three compositions the onset temperature of decarbonation occurs at ~600 °C. A noticeable observation is further that two peaks are apparent in each of the TPD diagrams, suggesting the step-wise decomposition of possibly

formed mixed (Ba,Sr) carbonates. Disregarding differences in the peak shapes, the integrated TPD peak areas indicate that distinctly less carbonates are formed during CO<sub>2</sub> exposure of BSCFZ3 and BSCFN10 (50% and 35%, respectively), relative to parent BSCF. This observation suggests that partial substitution of (Co,Fe) by redox-stable cations (*i.e.*, Zr, Nb) reduces exsolution of BaO and/or SrO from the perovskite lattice during CO<sub>2</sub> exposure, leading to formation of an alkaline-earth-deficient and/or decomposed perovskite phase, and to formation of carbonates at the surface. Similar observations have been reported in literature upon Ti- and Ta-substitution for (Co,Fe) in SrCo<sub>0.8</sub>Fe<sub>0.2</sub>O<sub>3-δ</sub> [1, 2], and Zr-substitution for Ce in BaCeO<sub>3</sub> [3, 4], which substitutions were made to enhance the CO<sub>2</sub> tolerance of these materials.

Some simple calculations of the phase stability of alkaline-earth doped perovskite phases in CO<sub>2</sub>-containing atmospheres were performed. Corresponding results are presented in Fig. 9.2. The lines in this figure indicate the partial pressure of CO<sub>2</sub>, separating the diagram of log(*p*CO<sub>2</sub>) versus reciprocal temperature into existence regions of the alkaline earth oxide, AO, (*i*) either with specified activity, *a*<sub>AO</sub>, dissolved into the perovskite oxide lattice (*oxide*), or (*ii*) in carbonated form, ACO<sub>3</sub> (*carbonate*). The calculations were performed on the basis of literature data for the equilibrium dissociation pressure of alkaline earth carbonates, according to reaction,



where A = Ba, Sr, and Ca. [5, 6]. Hence, the line with *a*<sub>AO</sub> = 1 corresponds with the equilibrium partial pressure of CO<sub>2</sub> for the coexistence of AO and ACO<sub>3</sub><sup>†</sup>. The graph clearly illustrates that the stability region of the alkaline-

---

<sup>†</sup> The equilibrium pressure of CO<sub>2</sub> for the coexistence of alkaline-earth oxides and carbonates are *i*) log (*p*CO<sub>2</sub>(atm)) = 7.704-13121/*T* for Ba, *ii*) log (*p*CO<sub>2</sub>(atm)) = 8.340-12275/*T* for Sr, and *iii*) log (*p*CO<sub>2</sub>(atm)) = 7.526-8792.3/*T* for Ca.

earth containing perovskite phase increases in the sequence Ba < Sr < Ca, and with decreasing activity of AO in the perovskite phase. With regard to the latter, more systematic research needs to be done to clarify which factors, comprising, amongst others, A-site cation deficiency, Goldschmidt tolerance factor, oxygen nonstoichiometry, A-O and B-O binding energies of A-O and B-O bonds, and ionic potential (or basicity) of dopant cations, determine the alkaline earth oxide, AO, activity in the perovskite oxide, and, hence, the stability of alkaline-earth doped perovskite oxides in CO<sub>2</sub>-containing atmospheres.

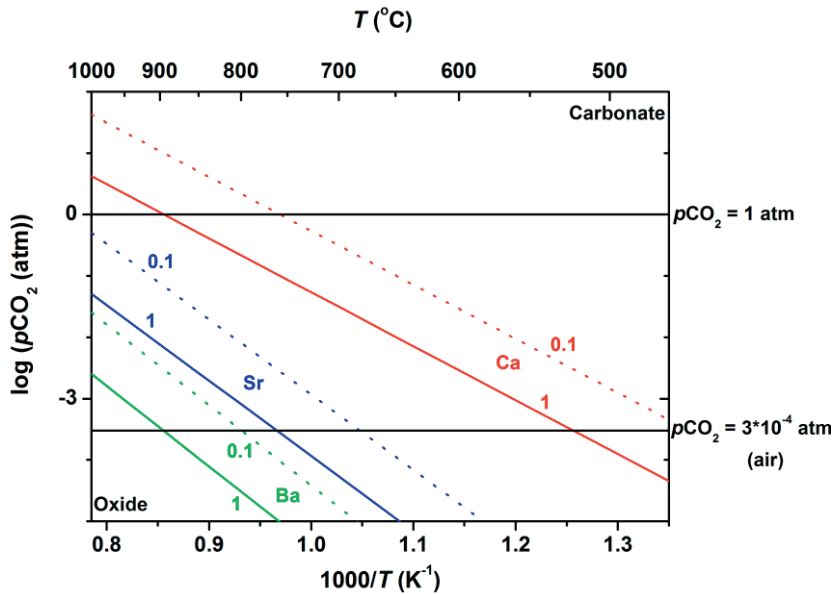


**Figure 9.2** Thermodynamic stability domain of ACO<sub>3</sub> (carbonate) versus AO (oxide, *i.e.*, dissolved in the perovskite oxide phase): A = Ba (green), Sr (blue), and Ca (red). Activities of the alkaline earth oxide,  $a_{AO}$ , used in calculation are indicated. Horizontal lines correspond to pure CO<sub>2</sub> ( $p_{CO_2} = 1$  atm) and ambient air ( $p_{CO_2} = 3 \times 10^{-4}$  atm).

### **9.3 Oxygen surface exchange kinetics**

Below, some recommendations are given to arrive at an improved understanding of the kinetics of oxygen surface exchange on solid oxide ion conducting materials.

To date, there is still a lack of understanding how the chemical nature, structure and morphology of the oxide surface affect the surface exchange kinetics. Segregation of dopants and impurities might occur in grain boundaries, but also at the surface exposed to the gas phase. Segregation may induce phase separation once the solid solubility limit is exceeded. In addition, crystallographic plane orientations and surface terminations might influence the exchange kinetics. These phenomena clearly emphasize the need for a thorough characterization of the oxide surface to aid interpretation of experimental data on oxygen surface exchange. In particular, measurements of the surface properties under operando conditions are considered to be relevant to improve current understanding of the oxygen exchange kinetics. A few methods that have attracted attention of the author are mentioned below.

Both X-ray photoelectron spectroscopy (XPS) and low energy ion scattering (LEIS) offer unique opportunities to investigate the chemical composition of the outermost surface [7, 8]. In general, however, the operating conditions of conventional XPS and LEIS are ultra-high vacuum (UHV, absolute pressures below  $10^{-12}$  atm) at room temperature, which is far from the real operating conditions of oxide-ion conducting materials. Recently, Backhaus-Ricoult *et al.* [9] demonstrated the use of *in-situ* synchrotron-based XPS measurements combination with electrochemical impedance spectroscopy to study operation of  $\text{La}_{1-x}\text{Sr}_x\text{FeO}_{3-\delta}$  in electrochemical  $\text{NO}_x$  sensors at elevated temperature and ambient pressure.



The diffraction of either photons, electrons, or neutrons is one of the most powerful methods for investigation of the surface structure. Surface diffraction patterns show a symmetry reflecting that of the surface structure. The methods can be used for *in-situ* determination of the atomic structure of adsorbed layers, surface reconstruction and relaxation, and buried interfaces of catalysts under real operating conditions [10, 11]. Hendriksen *et al.* [12] studied the surface reconstruction of Pd metal catalysts during catalytic CO oxidation by means of time-resolved surface X-ray diffraction combined with *in-situ* mass spectrometry. It was found that the formation of a PdO layer on the surface of Pd metal promotes CO oxidation to CO<sub>2</sub>.

Humidity of the gas phase has been claimed either to have a beneficial [13] or detrimental [14-16] effect on rate of surface oxygen exchange. A systematic, *in-situ* study on the effect of the ambient relative humidity on surface exchange might resolve apparent conflicts. Application of the pulse-response isotopic exchange (PIE) technique as exploited in this PhD work to study the surface exchange behavior of various oxide ionic and mixed ionic-electronic conductors is considered to be highly appropriate to conduct such investigations.

A major advantage of PIE is that the technique allows rapid assessment of the oxygen exchange rate. The residence time of the gas phase within the continuous flow reactor is in the range 10-40 ms. Other <sup>18</sup>O-<sup>16</sup>O isotope exchange-based techniques have much longer equilibration or exposure times, which may vary from minutes to hours. Still, the time scale of PIE measurements is not congruent with that of elementary acts during the exchange reaction, typically, these proceed on the time scale of femtoseconds or even picoseconds [17]. To investigate the elementary molecular processes during oxygen exchange fast spectroscopic techniques are required. Reference may be made to the work of Ahmed H. Zewail *for his studies of the transition states of chemi-*

*cal reactions using femtosecond spectroscopy*', which was awarded with The Nobel Prize in Chemistry 1999 [18].

## References

1. Q. Zeng, Y.-B. Zuo, C.-G. Fan, C.-S. Chen, *J. Membrane. Sci.* 335 (2009) 140.
2. W. Chen, C.-S. Chen, L. Winnubst, *Solid State Ionics* 196 (2011) 30.
3. K.H. Ryu, S.M. Haile, *Solid State Ionics* 125 (1999) 355.
4. C. Zuo, S.E. Dorris, U. Balachandran, M. Liu, *Chem. Mater.* 18 (2006) 4647.
5. J.J. Lander, *J. Am. Chem. Soc.* 73 (1951) 5794.
6. K.J. Hill, E.R.S. Winter, *J. Phys. Chem.* 60 (1956) 1361.
7. J.A. Kilner, S.J. Skinner, H.H. Brongersma, *J. Solid State Electrochem.* 15 (2011) 861.
8. W. Jung, H.L. Tuller, *Energy & Environmental Science* 5 (2012) 5370.
9. M. Backhaus-Ricoult, K. Adib, K. Work, M. Badding, T. Ketcham, M. Amati, L. Gregoratti, *Solid State Ionics* (2012) in press DOI: 10.1016/j.ssi.2012.03.007.
10. O. Balmes, R. van Rijn, D. Wermeille, A. Resta, L. Petit, H. Isern, T. Dufrane, R. Felici, *Catal. Today* 145 (2009) 220.
11. R. van Rijn, M.D. Ackermann, O. Balmes, T. Dufrane, A. Geluk, H. Gonzalez, H. Isern, E. de Kuyper, L. Petit, V.A. Sole, D. Wermeille, R. Felici, J.W.M. Frenken, *Rev. Sci. Instrum.* 81 (2010) 014101.
12. B.L.M. Hendriksen, M.D. Ackermann, R. van Rijn, D. Stoltz, I. Popa, O. Balmes, A. Resta, D. Wermeille, R. Felici, S. Ferrer, W.M. FrenkenJoost, *Nat. Chem.* 2 (2010) 730.
13. T. Ishihara, S. Fukui, H. Matsumoto, *J. Electrochem. Soc.* 152 (2005) A2035.
14. P. Hjalmarsson, M. Sogaard, M. Mogensen, *Solid State Ionics* 179 (2008) 1422.
15. A. Hagen, K. Neufeld, Y.L. Liu, *J. Electrochem. Soc.* 157 (2010) B1343.
16. J. Nielsen, A. Hagen, Y.L. Liu, *Solid State Ionics* 179 (2008) 1422.
17. M. Gruebele, A.H. Zewail, *Phys. Today* 43 (1990) 24.
18. A.H. Zewail, *Femtochemistry: Atomic-Scale Dynamics of the Chemical Bond Using Ultrafast Lasers* (Nobel lecture) (1999), retrieved on 15th June, 2012, from [http://www.nobelprize.org/nobel\\_prizes/chemistry/laureates/1999/zewail-lecture.html](http://www.nobelprize.org/nobel_prizes/chemistry/laureates/1999/zewail-lecture.html).

# Summary

The application of mixed ionic-electronic conducting oxides as oxygen separation membrane for the production of oxygen offers significant advantages over conventional cryogenic distillation. Perovskite- and fluorite-type oxides are promising candidates for such application. The research described in this thesis is mainly focused on *i*) crystal chemistry and phase stability of either Zr- or Nb-substituted  $\text{Ba}_{0.5}\text{Sr}_{0.5}\text{Co}_{0.8}\text{Fe}_{0.2}\text{O}_{3-\delta}$  (BSCF), and those of the parent perovskite phase, and *ii*) oxygen surface exchange kinetics of selected perovskite- and fluorite-type oxides.

**Chapter 1** provides an introduction of fundamental aspects, and describes relevant developments in the field of research. In **Chapter 2**, the cubic-to-hexagonal phase transition occurring in BSCF, at temperatures below 825 °C, is probed by means of electrical conductivity relaxation experiments. Both the surface exchange and chemical diffusion coefficients derived from the data of measurements are found to decline with time during long-term (332 h) annealing, at 800 °C, in pure oxygen. It is further demonstrated that the phase transformations are suppressed by partial substitution of 3 mol% Zr for (Co,Fe), thereby preserving the excellent oxygen transport properties of the parent BSCF phase.

**Chapter 3** examines the phase stability, thermal expansion, electrical conductivity, and oxygen permeation behavior of perovskite-type oxides with composition  $\text{Ba}_{0.5}\text{Sr}_{0.5}(\text{Co}_{0.8}\text{Fe}_{0.2})_{1-x}\text{Nb}_x\text{O}_{3-\delta}$  ( $x = 0-0.2$ ). Long-term annealing experiments in either flowing air or nitrogen, at 750 °C, demonstrate that the cubic-to-hexagonal phase transformation in BSCF can be suppressed by partial substitution of Nb for (Co,Fe). The latter is already found for 5 mol% Nb, which corresponds to the minimum level of substitution in the present study.

The partial substitution by redox-inactive Nb cations results in decreasing values for the electrical conductivity and thermal expansion. The oxygen permeation flux exhibited by 10 mol% Nb-substituted BSCF, in the range 800-900 °C, is reduced by 10% relative to that found for parent BSCF. However, when in similar experiments pure CO<sub>2</sub> is used as the sweeping gas, rather than inert helium, the oxygen flux drops instantaneously to a negligible value.

In **Chapter 4**, *in-situ* neutron powder diffraction is used to determine the crystal structures of 3 mol% Zr-substituted BSCF and 10 mol% Nb-substituted BSCF. Rietveld analysis of the diffraction patterns, recorded in the temperature range 27-900 °C, demonstrates that 3 mol% Zr-substituted BSCF exhibits cubic symmetry with space group  $Pm\bar{3}m$ , whereas 10 mol% Nb-substituted BSCF adopts an orthorhombic structure with space group  $Pnma$ . Relative to parent BSCF, the thermal expansion coefficient of 10 mol% Nb-substituted BSCF has decreased by ~30%, while that of 3 mol% Zr-substituted BSCF has remained almost similar.

In **Chapters 5-8**, the oxygen surface exchange kinetics of selected oxides is explored using the <sup>18</sup>O-<sup>16</sup>O pulse isotope exchange (PIE) method. As described in **Chapter 5**, the surface exchange rate exhibited by the fluorite-type 25 mol% erbia-stabilized bismuth oxide is comparable to those of perovskite-related oxides La<sub>0.8</sub>Sr<sub>0.2</sub>CoO<sub>3-δ</sub> and La<sub>2</sub>NiO<sub>4</sub>. The exchange kinetics is limited by the dissociative adsorption of oxygen. Electronation of superoxide ions (O<sub>2</sub><sup>-</sup>) at the surface is suggested to be the rate-limiting step for oxygen exchange.

The oxygen surface exchange kinetics of mixed conducting perovskite oxides SrTi<sub>1-x</sub>Fe<sub>x</sub>O<sub>3-δ</sub> (x = 0, 0.01, 0.05, 0.35, 0.5) is investigated in **Chapter 6**. The exchange rate is found to increase with increasing iron mole fraction until it saturates at the highest values of x. The increase of the exchange rate with x in SrTi<sub>1-x</sub>Fe<sub>x</sub>O<sub>3-δ</sub> is concomitant with corresponding increases of the electronic

and ionic conductivities. At 600 °C, an almost linear relationship is found between the exchange rate and oxide ionic conductivity. Corresponding data for perovskite-type oxides  $\text{SrTi}_{1-x}\text{Fe}_x\text{O}_{3-\delta}$ ,  $\text{Ba}_{0.5}\text{Sr}_{0.5}\text{Co}_{0.8}\text{Fe}_{0.2}\text{O}_{3-\delta}$ ,  $\text{La}_{0.6}\text{Sr}_{0.4}\text{Co}_{0.2}\text{Fe}_{0.8}\text{O}_{3-\delta}$ ,  $\text{La}_{0.6}\text{Sr}_{0.4}\text{CoO}_{3-\delta}$ , and  $\text{Sm}_{0.5}\text{Sr}_{0.5}\text{CoO}_{3-\delta}$  are found to coincide with this relationship. The observation suggests that it is the magnitude of the oxide ionic conductivity that governs the rate of oxygen surface exchange. Two different reaction schemes are employed to interpret the observed distribution of oxygen isotopomers ( $^{18}\text{O}_2$ ,  $^{16}\text{O}^{18}\text{O}$ , and  $^{16}\text{O}_2$ ) in the effluent pulse.

**Chapter 7** presents data of PIE measurements on 20 mol% rare-earth oxide-doped ceria,  $\text{RE}_{0.2}\text{Ce}_{0.8}\text{O}_{2-\delta}$  (RE = Gd, Sm, Pr, Tb), in the range of temperature 500-950 °C and oxygen partial pressure 0.1-0.95 atm.  $\text{Gd}_{0.2}\text{Ce}_{0.8}\text{O}_{2-\delta}$ ,  $\text{Sm}_{0.2}\text{Ce}_{0.8}\text{O}_{2-\delta}$ , and  $\text{Pr}_{0.2}\text{Ce}_{0.8}\text{O}_{2-\delta}$  show similar exchange rates, while that of  $\text{Tb}_{0.2}\text{Ce}_{0.8}\text{O}_{2-\delta}$  is about one order of magnitude lower. No apparent relationships are found between the exchange rates and either the ionic, electronic or ambipolar conductivity. It is shown that dissociative adsorption of oxygen molecules is the rate-determining step for oxygen surface exchange on  $\text{RE}_{0.2}\text{Ce}_{0.8}\text{O}_{2-\delta}$ .

**Chapter 8** represents a study towards oxygen surface exchange on perovskite-type oxides  $\text{La}_{1-x}\text{Sr}_x\text{CoO}_{3-\delta}$  ( $x = 0, 0.2, 0.4, 0.5, 0.7$ ). PIE measurements are conducted under synthetic air in the temperature range of 300-600 °C. Poor exchange rates are found for  $\text{LaCoO}_{3-\delta}$  and  $\text{La}_{0.8}\text{Sr}_{0.2}\text{CoO}_{3-\delta}$ . The measurements for these compounds are complicated due to significant  $^{18}\text{O}$ -accumulation at the surface. The exchange rate is found to increase with increasing  $x$  in  $\text{La}_{1-x}\text{Sr}_x\text{CoO}_{3-\delta}$ . Analysis shows incorporation of oxygen adatoms in the oxide lattice to be the rate-determining step for oxygen surface exchange on  $\text{La}_{0.6}\text{Sr}_{0.4}\text{CoO}_{3-\delta}$ , while dissociative adsorption of oxygen molecules is found to be rate-determining for  $\text{La}_{0.5}\text{Sr}_{0.5}\text{CoO}_{3-\delta}$  and  $\text{La}_{0.3}\text{Sr}_{0.7}\text{CoO}_{3-\delta}$ .

Finally, some recommendations for further research are provided in **Chapter 9**. More research is needed towards *i*) the factors governing the stability of alkaline-earth doped perovskite-type oxides in CO<sub>2</sub>-containing atmospheres, and *ii*) oxygen surface exchange kinetics on oxide ion conductors. With regard to the latter, in particular, the use of operando methods is recommended.

# Samenvatting

De toepassing van gemengd ionen-elektronen oxiden als zuurstofscheidend membraan voor de productie van zuurstof biedt aanzienlijke voordelen ten opzichte van conventionele cryogene destillatie. Perovskiet- en fluoriet-type oxiden zijn veelbelovende kandidaten voor deze toepassing. Het onderzoek beschreven in dit proefschrift is voornamelijk gericht op *i*) kristalchemie en fasestabiliteit van Zr- dan wel Nb-gesubstitueerd  $\text{Ba}_{0.5}\text{Sr}_{0.5}\text{Co}_{0.8}\text{Fe}_{0.2}\text{O}_{3-\delta}$  (BSCF), en die van de oorspronkelijke perovskietfase, en *ii*) kinetiek van de zuurstofuitwisseling aan het oppervlak van geselecteerde perovskiet- en fluoriet-type oxiden.

**Hoofdstuk 1** geeft een introductie van fundamentele aspecten en beschrijft relevante ontwikkelingen in het veld van onderzoek. In **Hoofdstuk 2** wordt de faseovergang van kubisch naar hexagonaal optredend in BSCF bij temperaturen lager dan 825 °C bestudeerd door middel van elektrische geleidingsrelaxatiemetingen. Zowel de oppervlakte-uitwisselingscoëfficiënt als de chemische diffusiecoëfficiënt, die beide uit de gegevens van de metingen kunnen worden afgeleid, nemen af tijdens langdurig (332 uur) temperen bij 800 °C in zuivere zuurstof. Voorts wordt aangetoond dat de faseovergang kan worden onderdrukt door partiële substitutie van 3 mol% Zr voor (Co,Fe), waarbij de excellente zuurstoftransporteigenschappen van het oorspronkelijke BSCF behouden blijven.

**Hoofdstuk 3** bestudeert de fase-stabiliteit, thermische uitzetting, elektrische geleiding, en gedrag van de zuurstofpermeatie van perovskite-type oxiden met de samenstelling  $\text{Ba}_{0.5}\text{Sr}_{0.5}(\text{Co}_{0.8}\text{Fe}_{0.2})_{1-x}\text{Nb}_x\text{O}_{3-\delta}$  ( $x = 0-0.2$ ). Langdurig temperen in stromende lucht of stikstof, op 750 °C, laat zien dat de overgang van de kubische naar de hexagonale fase in BSCF onderdrukt kan worden door partiële substitutie van Nb voor (Co,Fe). Dit laatste treedt reeds op bij 5 mol%



Nb, welke waarde overeenkomt met de minimum substitutie in de uitgevoerde studie. De partiële substitutie van redox-inactieve Nb kationen leidt tot afnemende waarden voor de elektrische geleidbaarheid en thermische uitzetting. De flux ten gevolge zuurstofpermeatie gevonden voor 10 mol% Nb-gesubstitueerd BSCF in het temperatuurgebied 800-900 °C is met 10% afgenomen ten opzichte van die van het ongesubstitueerde BSCF. Wanneer echter tijdens gelijksoortige experimenten zuiver CO<sub>2</sub> gebruikt wordt als spoelgas, anders dan inert helium, daalt de zuurstofflux instantaan naar een verwaarloosbare waarde.

In **Hoofdstuk 4** wordt *in-situ* neutronen-poederdiffractie gebruikt om de kristalstructuren te bepalen van 3 mol% Zr-gesubstitueerd BSCF en 10 mol% Nb-gesubstitueerd BSCF. Rietveld analyse van de diffractiepatronen, opgenomen in het temperatuurgebied 27-900 °C, laat zien dat 3 mol% Zr-gesubstitueerde BSCF kubische symmetrie heeft met ruimtengroep  $Pm\bar{3}m$ , terwijl 10 mol% Nb-gesubstitueerd BSCF een orthorhombische structuur heeft met ruimtengroep  $Pnma$ . Ten opzichte van het ongesubstitueerde BSCF is de thermische uitzettingscoëfficiënt van 10 mol% Nb-gesubstitueerde BSCF met ~ 30% afgenomen, terwijl die van het 3 mol% Zr-gesubstitueerde BSCF nagenoeg gelijk gebleven is.

In **Hoofdstukken 5-8** wordt de uitwisselingskinetiek van zuurstof aan het oppervlak van geselecteerde oxiden onderzocht met behulp van de <sup>18</sup>O-<sup>16</sup>O puls-isotopenuitwisselingsmethode (*Pulse isotopic exchange*, PIE). Zoals beschreven in **Hoofdstuk 5**, de uitwisselingsnelheid van de fluoriet-type 25 mol% erbia-gestabiliseerd bismuthoxide is vergelijkbaar met die van de perovskiet-gerelateerde oxiden La<sub>0.8</sub>Sr<sub>0.2</sub>CoO<sub>3-δ</sub> and La<sub>2</sub>NiO<sub>4</sub>. De uitwisselingskinetiek wordt beperkt door de dissociatieve adsorptie van zuurstof. Verondersteld wordt dat de elektronenoverdracht naar superoxide-ionen (O<sub>2</sub><sup>-</sup>) aan het oppervlak de snelheidsbepalende stap is in de zuurstofuitwisseling.

De kinetiek van zuurstofuitwisseling aan het oppervlak van gemengde geleidende perovskiet-type oxiden  $\text{SrTi}_{1-x}\text{Fe}_x\text{O}_{3-\delta}$  ( $x = 0, 0.01, 0.05, 0.35, 0.5$ ) wordt onderzocht in **Hoofdstuk 6**. De uitwisselingsnelheid neemt toe met een toenemende molfractie van ijzer totdat verzadiging optreedt bij de hoogste waarden van  $x$ . De toename van de uitwisselingsnelheid met  $x$  in  $\text{SrTi}_{1-x}\text{Fe}_x\text{O}_{3-\delta}$  treedt gelijktijdig op met dienovereenkomstige toenames van de elektronische en ionogene geleidingsvermogens. Bij 600 °C wordt een bijna lineair verband gevonden tussen de uitwisselingsnelheid en de zuurstofionengeleiding. Corresponderende waarden voor perovskiet-type oxiden  $\text{SrTi}_{1-x}\text{Fe}_x\text{O}_{3-\delta}$ ,  $\text{Ba}_{0.5}\text{Sr}_{0.5}\text{Co}_{0.8}\text{Fe}_{0.2}\text{O}_{3-\delta}$ ,  $\text{La}_{0.6}\text{Sr}_{0.4}\text{Co}_{0.2}\text{Fe}_{0.8}\text{O}_{3-\delta}$ ,  $\text{La}_{0.6}\text{Sr}_{0.4}\text{CoO}_{3-\delta}$ , en  $\text{Sm}_{0.5}\text{Sr}_{0.5}\text{CoO}_{3-\delta}$  vallen hiermee samen. De waarneming suggereert dat de mate van ionengeleiding bepalend is voor de zuurstofuitwisselingsnelheid. Twee verschillende reactieschema's worden gebruikt voor een verklaring van de waargenomen verdeling van zuurstofisotopen ( $^{18}\text{O}_2$ ,  $^{16}\text{O}^{18}\text{O}$  en  $^{16}\text{O}_2$ ) in de effluent puls.

**Hoofdstuk 7** geeft de resultaten van PIE metingen aan 20 mol% van ceria gedoteerd met zeldzame aardoxiden,  $\text{RE}_{0.2}\text{Ce}_{0.8}\text{O}_{2-\delta}$  (RE = Gd, Sm, Pr, Tb) in het temperatuurgebied 500-950 °C en dat van de zuurstofpartiaalspanning 0.1-0.95 atm.  $\text{Gd}_{0.2}\text{Ce}_{0.8}\text{O}_{2-\delta}$ ,  $\text{Sm}_{0.2}\text{Ce}_{0.8}\text{O}_{2-\delta}$  en  $\text{Pr}_{0.2}\text{Ce}_{0.8}\text{O}_{2-\delta}$  laten vergelijkbare uitwisselingsnelheden zien, terwijl dat van  $\text{Tb}_{0.2}\text{Ce}_{0.8}\text{O}_{2-\delta}$  ongeveer een orde van grootte lager is. Er worden geen schijnbare relaties gevonden tussen enerzijds de uitwisselingsnelheid en anderzijds de ionogene, elektronische of ambipolaire geleiding. Aangevoerd wordt dat de dissociatieve adsorptie van zuurstofmoleculen de snelheidsbepalende stap is voor de zuurstofuitwisseling aan het oppervlak van  $\text{RE}_{0.2}\text{Ce}_{0.8}\text{O}_{2-\delta}$ .

**Hoofdstuk 8** betreft een studie naar de zuurstofuitwisseling van perovskiet-type oxiden  $\text{La}_{1-x}\text{Sr}_x\text{CoO}_{3-\delta}$  ( $x = 0, 0.2, 0.4, 0.5, 0.7$ ). PIE metingen worden uitgevoerd onder synthetische lucht in het temperatuurgebied 300-600 °C.

Lage waarden worden gevonden voor de zuurstof-uitwisselingsnelheid van  $\text{LaCoO}_{3-\delta}$  en  $\text{La}_{0,8}\text{Sr}_{0,2}\text{CoO}_{3-\delta}$ . De metingen voor deze verbindingen worden bemoeilijkt door aanzienlijke accumulatie van  $^{18}\text{O}$  aan het oppervlak. De uitwisselingsnelheid neemt toe met toenemende  $x$  in  $\text{La}_{1-x}\text{Sr}_x\text{CoO}_{3-\delta}$ . Analyse laat zien dat het inbouwen van geadsorbeerde zuurstofatomen in het kristalrooster van het oxide de snelheidsbepalende stap is voor zuurstofuitwisseling aan  $\text{La}_{0,6}\text{Sr}_{0,4}\text{CoO}_{3-\delta}$ , terwijl dissociatieve adsorptie van zuurstofmoleculen de snelheidsbepalende stap is voor  $\text{La}_{0,5}\text{Sr}_{0,5}\text{CoO}_{3-\delta}$  en  $\text{La}_{0,3}\text{Sr}_{0,7}\text{CoO}_{3-\delta}$ .

Ten slotte worden enkele aanbevelingen voor verder onderzoek gedaan in **Hoofdstuk 9**. Meer onderzoek is nodig naar *i*) de factoren die de stabiliteit bepalen van perovskiet-type oxiden gedoteerd met aardalkalimetalen in  $\text{CO}_2$ -houdende atmosferen, en *ii*) de kinetiek van zuurstofuitwisseling aan het oppervlak van zuurstofionengeleiders. Wat dit laatste betreft wordt met name de toepassing van operando technieken aanbevolen.

## Acknowledgement

After four-year enjoyable life at the University of Twente in Enschede, now, it is time to end my journey. I would like to express my sincere gratitude to all people who directly or indirectly contributed to my Ph D thesis.

First of all, I would like to thank Arian Nijmeijer and Henny Bouwmeester for giving me the excellent opportunity to work and study in Inorganic Membranes (IM) at the University of Twente and motivating me to enjoy my Ph D study. Especially, I am very grateful to Henny for introducing me to the world of dense ceramic membrane, having intensive discussions, and correcting my articles and thesis.

I would like to thank Bernard Boukamp for discussions and help for oxygen isotope exchange and electrochemical impedance spectroscopy and correcting the Chapter 7 and 8 of this thesis. Louis Winnubst guided me to grasp the knowledge of ceramic processing and powder characterization.

I would like to express my appreciation to my committee members, Peter Vang Hendriksen, Hans-Dieter Wiemhöfer, Harold Zandvliet, and André ten Elshof for their help, suggestions, and discussions.

I would like to thank MEM-BRAIN project funded by Helmholtz Association of German Research Centers for my Ph D study. I have enjoyed nice discussions and collaborations within MEM-BRAIN project.

During my Ph D, I have realized that the team-work is more interesting than working alone. Especially, I would like to thank solid state ionics/perovskite alliance members: Sergey Yakovlev, Shumin Fang, Weihua Zhou, Tingfang Tian, Chunlin Song, Bo Wang, Tan Phung, Wei Chen, Bas ten Donkelaar, María Balaguer, and Nicolas Hildenbrand. I appreciate for their laboratory works, fruitful discussions, and great patience for me.

My life at the university would be difficult without help from Frank Morssinkhof, Susanne van Rijn, Greet Kamminga, Mieke Luiten-Olieman, Cindy Huiskes, Hermann Teunis, John Heeks, Louise Vrielink, and Mark Smithers. Many thanks for Other IM colleagues, Nieck Benes, Martin Wolf, Ana Pinheiro, Giri Sripathi, Hammad Qureshi, Emiel Kappert, Marcel ten Hove, Michiel Raaijmakers, Cheryl Tarnadi, Sushumna Shukla, Can Aran, and Kishore Tetala. During my Ph D, I am appreciated group activities such as Batavierenrace, study tour, football, shooting (many thanks for David Salamon, Szymon Dutczak, and Nick Aldenkamp), and bike tour with Membrane Technology Group and Soft Matters and Interface group.

지난 4 년간 엔스헤테에서 한국분들에서 많은 도움을 받았습니다. 저에게 트벤테 대학을 알려주신 광민석 선배님과 형수님, 그리고 트벤테 대학에서 먼저 오셔서 많은 도움을 주신 이운재, 이중석, 조대준 선배님에게 감사를 전하고 싶습니다. 제가 학위하는 동안 좋은 추억을 만들어주신 오정민 박사님, 남현우 교수님, 홍정진 박사님과 사모님, 강원이, 서영이, 이은수 박사님, 윤영술 선생님과 한얼이에게도 감사를 드립니다. 그리고, 앞으로 엔스헤테를 지켜주실 노훈석, 양윤선, 박선영, 백신우님께도 감사를 드립니다. 그리고, 저에게 학문의 길을 열어 주신 아주대학교 김승주 교수님과 신물질 화학 실험방 사람들에게도 감사를 드립니다.

항상 저를 응원해주신 아버지와 어머님 그리고 정열이에게도 감사를 드립니다. 4 년간 네덜란드에서 아무 걱정 없이 학위 할 수 있었던 것은 가족덕분이라고 생각합니다. Finally, I would like to thank Velianti for her help, patience, and understanding. We have been in long-distance relationship, but you always make me happy wherever you are. Now, it is my turn to make you happy. Cinta Velianti. 벨리안티 사랑합니다.

## **Chung-Yul Yoo**

**Inorganic Membranes  
Faculty of Science and Technology  
University of Twente, P.O. Box 217  
7500 AE, Enschede, The Netherlands  
Phone: +31 53 4894581  
Mobile: +31 6 52717265  
E-mail: c.yoo@utwente.nl (work)  
chungyulyoo@gmail.com**

---

### **Education**

---

- |   |                       |
|---|-----------------------|
| Ph D, University of Twente, The Netherlands   | Sep. 2008 ~ Sep. 2012 |
| Thesis title: Phase stability and oxygen transport properties of mixed ionic-electronic conducting oxides |                       |
| Master (Chemistry), Ajou University, South Korea  | Sep. 2006 ~ Aug. 2008 |
| Thesis title: Structure and property of mixed-anion layered perovskite and Li-containing garnet compounds |                       |
| Cumulative GPA: 4.45/4.5  |                       |
| Bachelor (Chemistry), Ajou University, South Korea  | Mar. 2000 ~ Aug. 2006 |
| Cumulative GPA: 4.03/4.5  |                       |

---

### **Awards**

---

- Sep. 2008 ~ Sep. 2012: Fellowship for Ph D, Helmholtz Association
- Aug. 2006 ~ Aug. 2008: Brain Korea 21 Fellowship, Korea Research Foundation
- Aug. 2006 ~ Aug. 2008: Graduate Student Scholarship, Ajou University
- Mar. 2006: Most outstanding student for 2005, Guwon Scholarship Foundation
- Mar. 2001 ~ Aug. 2006: Undergraduate Student Scholarship, Ajou University

---

### **Special knowledges**

---

- Preparation of oxide powder and dense ceramics
- Molten salt flux and chemical vapor transport method to prepare single crystals
- Solvothermal and electrodeposition method to prepare nanostructured oxides
- Crystal structure determination using X-ray and neutron powder diffraction data (Rietveld analysis and ab-initio structure determination)

- X-ray absorption spectroscopy (XANES and EXAFS)
- IR, Raman, and UV-vis spectroscopy, thermogravimetry, electron microscopy (SEM and TEM)
- Impedance analysis for lithium and oxide ion conductivity
- Gas phase analysis for catalytic reaction products using in-situ mass spectrometry
- Building equipment including cryogenic system for isotope gas handling and electrochemical cell
- N<sub>2</sub>/CO<sub>2</sub> gas sorption measurement for characterizing the surface area and pore size distribution of powder
- Scientific programming for simulation and numerical fitting using MATLAB

### List of publications

1. C.-Y. Yoo and H.J.M. Bouwmeester, "Oxygen surface exchange kinetics of PrBa-Co<sub>2</sub>O<sub>5.5+δ</sub>", Journal of Materials Chemistry, to be submitted (2012).
2. M. Balaguer, C.-Y. Yoo, H.J.M. Bouwmeester, and J.M. Serra, "Bulk and surface properties of the mixed ionic-electronic conductor Ce<sub>1-x</sub>Tb<sub>x</sub>O<sub>2-δ</sub> (x=0.1, 0.2, 0.5)", Journal of Materials Chemistry, to be submitted (2012).
3. C.-Y. Yoo, J. Kohnke, G. Schumacher, and H.J.M. Bouwmeester, "In-situ neutron diffraction study of zirconium- and niobium-substituted Ba<sub>0.5</sub>Sr<sub>0.5</sub>Co<sub>0.8</sub>Fe<sub>0.2</sub>O<sub>3-δ</sub>", Materials Research Bulletin, to be submitted (2012).
4. C.-Y. Yoo and H.J.M. Bouwmeester, "Oxygen surface exchange kinetics of SrTi<sub>1-x</sub>Fe<sub>x</sub>O<sub>3-δ</sub> mixed conducting oxides", Physical Chemistry Chemical Physics, 14, 11759, (2012). DOI:10.1039/C2CP41923H
5. S.M. Fang, C.-Y. Yoo, and H.J.M. Bouwmeester, "Performance and stability of niobium-substituted Ba<sub>0.5</sub>Sr<sub>0.5</sub>Co<sub>0.8</sub>Fe<sub>0.2</sub>O<sub>3-δ</sub> membranes", Solid State Ionics, 195, 1 (2011). DOI:10.1016/j.ssi.2011.05.022
6. C.-Y. Yoo, B.A. Boukamp, and H.J.M. Bouwmeester, "Oxygen surface exchange kinetics of erbia-stabilized bismuth oxide", Journal of Solid State Electrochemistry, 15, 231 (2011). DOI:10.1007/s10008-010-1168-8
7. S. Yakovlev, C.-Y. Yoo, S. Fang, and H.J.M. Bouwmeester, "Phase transformation and oxygen equilibration kinetics of pure and Zr-doped Ba<sub>0.5</sub>Sr<sub>0.5</sub>Co<sub>0.8</sub>Fe<sub>0.2</sub>O<sub>3-δ</sub> perovskite oxide probed by electrical conductivity relaxation", Applied Physics Letter, 96, 254101, (2010). DOI:10.1063/1.3455908
8. C.-Y. Yoo, S.-C. Kim, S.-S. Lee, and S.-J. Kim, "Synchrotron study of the garnet-type oxide Li<sub>6</sub>CaSm<sub>2</sub>Ta<sub>2</sub>O<sub>12</sub>", Acta Crystallographica Section E, E65, i74, (2009). DOI:10.1107/S1600536809040008
9. Y.-J. Song, C.-Y. Yoo, J.-T. Hong, S.-J. Kim, S.U. Son, and H.-Y. Jang, "Nanocrystalline Copper Oxide(II)-Catalyzed Alkyne-Azide Cycloadditions", Bulletin of Korean Chemical Society, 29, 1561 (2008)

10. C.-Y. Yoo and S.-J. Kim, "Dimensional modification of oxyfluoridelattice: Preparation and structure of  $A'ANb_2O_6F$  ( $A' = Na, K, A = Ca, Sr$ )", *Journal of Physics and Chemistry of Solids*, 69, 1475 (2008). DOI:10.1016/j.jpcs.2007.09.013
11. C.-Y. Yoo and S.-J. Kim, "KCaNb<sub>2</sub>O<sub>6</sub>F from a combined synchrotron X-ray and neutron powder diffraction study", *Acta Crystallographica Section E*, E63, i203, (2007). DOI:10.1107/S16005368070604362002
12. C.-Y. Yoo, K.-P. Hong, and S.-J. Kim, "A new layered perovskite, KSrNb<sub>2</sub>O<sub>6</sub>F, by powder neutron diffraction", *Acta Crystallographica Section C*, C63, i63, (2007). DOI:10.1107/S0108270107029563

## List of presentations

---

### Oral presentations

1. C.-Y. Yoo, B.A. Boukamp, and H.J.M. Bouwmeester, "Oxygen exchange kinetics of mixed ionic-electronic conducting oxides", *Electroceramics 13*, Enschede, The Netherlands, June (2012).
2. C.-Y. Yoo, J. Kohnke, G. Schumacher, and H.J.M. Bouwmeester, "In-situ neutron diffraction study of zirconium- and niobium-substituted Ba<sub>0.5</sub>Sr<sub>0.5</sub>Co<sub>0.8</sub>Fe<sub>0.2</sub>O<sub>3-δ</sub>", E-MRS meeting, Strasbourg, France, May (2012).
3. C.-Y. Yoo, T.F. Tian, C.S. Chen, and H.J.M. Bouwmeester, "Oxygen surface exchange kinetics of gadolinia- and samaria- doped ceria", 18th International conference on Solid State Ionics, Warsaw, Poland, July (2011).
4. C.-Y. Yoo and H.J.M. Bouwmeester, "Oxygen surface exchange of SrTi<sub>1-x</sub>Fe<sub>x</sub>O<sub>3-δ</sub> (x = 0, 0.35, 0.5)", E-MRS meeting, Strasbourg, France, June (2010).

### Selected poster presentations

1. C.-Y. Yoo, B.A. Boukamp, and H.J.M. Bouwmeester, "Oxygen exchange kinetics of mixed ionic-electronic conducting oxides", *International Conference on Inorganic Membranes 12*, Enschede, The Netherlands, July (2012).
2. C.-Y. Yoo, S.-J. Kim, M.-R. Li, and S.-T. Hong, "Structure of Oxygen-Deficient Perovskite Oxides, Ba<sub>11</sub>W<sub>4-x</sub>M<sub>x</sub>O<sub>23-0.75x</sub> (M = Al, Ga) by Combined Synchrotron X-ray and Neutron Powder Diffraction", 2nd International Conference on Physics of Solid State Ionics, Yokohama, Japan, December (2007).
3. S.-J. Kim, H.-J. Kim, C.-Y. Yoo, and N.H. Hur, "Metal insulator transition in V<sub>2</sub>W<sub>x</sub>Mo<sub>1-x</sub>O<sub>6</sub> studied by X-ray absorption spectroscopy", The 10th Asia Pacific Physics Conference, Pohang, south Korea, August (2007).
4. C.-Y. Yoo and S.-J. Kim, "Photoluminescence property of melamine derivatives prepared by thermal decomposition", The 10th Asia Pacific Physics Conference, Pohang, south Korea, August (2007).
5. C.-Y. Yoo and S.-J. Kim, "Dimensional Modification of Oxyfluoride Lattice : Preparation and Structure of KANb<sub>2</sub>O<sub>6</sub>F (A = Ca, Sr)", *International Symposium on Intercalation Compounds 14th*, Seoul, south Korea, June (2007).



6. C.-Y. Yoo and S.-J. Kim, “Synthesis and structural characterization of new layered perovskite-type oxyfluoride,  $\text{KSrNb}_2\text{O}_6\text{F}$ ”, the 99th Korean Chemical Society meeting, Seoul, south Korea, April (2007).

7. C.-Y. Yoo, N.-S. Shin, and S.-J. Kim, “Structural characterization of the new supralattice-type oxide,  $\text{Ca}_{7.4}\text{Ga}_{5.7}\text{Zn}_{1.9}\text{O}_{17.85}$  by synchrotron X-ray powder diffraction”, the 18th Korean Synchrotron User Association meeting, Pohang, south Korea, November, 19, (2006).

---

### Other experiences

---

- Sep. 2008 ~ Sep. 2012: Graduate teaching assistant, University of Twente
- Sep. 2006 ~ Aug. 2008: Graduate teaching assistant, Ajou University
- Jan. 2005 ~ Dec. 2005: Student representative of chemistry, Ajou University
- Mar. 2002 ~ Apr. 2004: Mandatory military service at the Republic of Korea Army

---

### Personal information

---

- Date of birth: 10th Feb. 1982
- Nationality: South Korea (Republic of Korea)

Updated on 15th Aug. 2012